

© 2017 Daniel James Fisher

OBSERVATIONS OF THE THERMOSPHERE USING MEASUREMENTS
FROM LONG-TERM FABRY-PEROT INTERFEROMETERS

BY

DANIEL JAMES FISHER

DISSERTATION

Submitted in partial fulfillment of the requirements
for the degree of Doctor of Philosophy in Electrical and Computer Engineering
in the Graduate College of the
University of Illinois at Urbana-Champaign, 2017

Urbana, Illinois

Doctoral Committee:

Professor Jonathan J. Makela, Chair
Professor Erhan Kudeki
Assistant Professor Lara Waldrop
Professor P. Scott Carney

ABSTRACT

Since the ionosphere was discovered in the 1920s, numerous and diverse experiments have been conducted to classify this region of the upper atmosphere. Radar, satellites, rockets, ionosondes, global positioning system (GPS) receivers, and more have been used to probe and understand this region between Earth and space. However, the ionosphere is coupled to the neutral region of the atmosphere, known as the thermosphere, and only through knowledge of the state parameters of both regions can accurate predictions of ionospheric phenomena be made during both quiet conditions and geomagnetic storms. As a compounding factor, thermospheric data have been historically lacking compared to the plentiful plasma datasets.

Neutral wind and temperature data are needed to understand and validate the physics of the upper atmosphere. As satellites do not provide high-resolution temporal coverage over a given region, stationary ground-based systems are needed to observe the thermosphere. The focus of this dissertation is to analyze the nighttime thermospheric winds and temperatures from data collected by Fabry-Perot interferometers (FPI) operating in Brazil, the United States, and Morocco. These instruments observe the 630.0-nm redline emission and estimate the neutral parameters from the Doppler shift and broadening of the spectra. The instruments provide a nearly-continuous, long-term nighttime dataset from deep solar minimum through solar maximum and the current decline. These data are required to improve the accuracy of empirical models that are commonly used to drive ionospheric simulations.

We provide monthly averages from each site to be used as a baseline of the quiet-time thermospheric temperatures, zonal winds, and meridional winds. Using these climatologies, we analyze the daily, seasonal, solar, and geographic variations in the neutral parameters. Further, these climatologies are used to validate and improve the horizontal wind model (HWM), a widely

used empirical model of atmospheric winds. Finally, we use storm-time neutral wind measurements along with equatorial plasma bubble (EPB) observations from a collocated all-sky imager (ASI) to study the activation of the disturbance dynamo.

I dedicate this dissertation to the unfortunate, future graduate student who reads this ... I sincerely hope this document helps you understand just one thing a bit better: Just keep swimming!

ACKNOWLEDGMENTS

First and foremost, I would like to thank my adviser, Professor Jonathan J. Makela. Without his support and guidance, I am sure this dissertation would have never been completed. He has spent years nurturing my ability to do meaningful research, helping to mold me into a nearly independent critical thinker. He has taught me how to question, analyze, and validate, which shall be invaluable gifts I can take with me in pursuit of my career. I am lucky to have been able to work under him, and am glad I can look back fondly on all the years under his mentorship.

Second, this dissertation would not have been possible without the help of many collaborators. The RENOIR, NATION, and Moroccan systems were only successful thanks to an enormous list of people who contributed to their design, installation, operation, and maintenance. Specifically, I would like to thank John Meriwether, Ricardo Buriti, and Rafael Mesquita who were very supportive during my first years of graduate school. Additionally, I must thank Nancy Morris for taking the burden of administrative tasks from me.

Third, I need to thank the friends who have been by my side throughout my many years of collegiate education. Shoutout to the Mak5 crew: Tim Duly, Tommy Gehrels, Matt Grawe, Brian Harding, Yiyi Huang, and Dimitris Iliou. Your help and encouragement will always be appreciated. We did great science! I'd also like to thank the post-docs who aided my progress as a graduate student: Mark Butala, Narayan Chapagain, Pierdavid Coisson, and Jianqi Qin. A special thanks is given to the other grad students who helped me keep my sanity: Anthony Christodoulou, Dave Cohen, Erik Johnson, Tony Mangogna, Pablo Reyes, and Sarah Robinson. To my oldest friends, and to all those I have wrongly omitted, I thank you for your support. My graduate life would not have been the same without each and every one of you.

Fourth, I must thank the University of Illinois. We've had eleven great

years of higher education together, and although I will be moving far away from you, you will always have a piece of my heart. From your challenging courses to your beautiful campus, clearly there was no better university than you.

Fifth, I thank Chelsea. My love, you have been the yin to my yang. Thank you for not murdering me during this process. I look forward to our many years together.

Finally, I need to thank my parents. You have supported me since birth and I have not communicated how important that has been to my success. Schooling was always a priority, and now, after 24 years of education, I'm finally done!

I acknowledge financial support by the National Science Foundation under Grant Nos. ATM 09-40253, AGS 11-38998, and AGS 14-52291, NASA under Grant No. NNX14AD46G, and the Office of Naval Research under Grant No. N00014-13-1-0350. Any opinion, findings, and conclusions or recommendations expressed in this material are those of the author and do not necessarily reflect the views of the National Science Foundation.

TABLE OF CONTENTS

LIST OF ABBREVIATIONS	ix
LIST OF SYMBOLS	xi
CHAPTER 1 INTRODUCTION	1
1.1 Motivation	1
1.2 Overview	2
CHAPTER 2 THE THERMOSPHERE	3
2.1 Thermospheric Background	3
2.2 Airglow	4
2.3 Thermospheric Winds and Temperatures	7
2.4 Geomagnetic Storms	11
2.5 Current Research Direction	12
CHAPTER 3 INSTRUMENTATION FOR AIRGLOW MEASURE- MENTS	14
3.1 The Fabry-Perot Interferometer	14
3.2 Our Instrumentation	17
3.2.1 Data Processing	21
3.2.2 Climatological Processing	25
CHAPTER 4 CLIMATOLOGICAL STUDIES OF NEUTRAL WINDS AND TEMPERATURES	27
4.1 Climatological Analysis Methodology	27
4.1.1 Sorting by Solar Flux	28
4.1.2 Three Climatological Analyses	30
4.2 Climatological Results	31
4.2.1 Climatology for Northeastern Brazil	38
4.2.2 Climatology for PARI	43
4.2.3 Climatology for Morocco	44
4.3 Discussion of Climatological Variations	45
4.3.1 Seasonal Neutral Variations	45
4.3.2 Solar-Driven Neutral Variations	46
4.3.3 Geographic Variations of Neutral Winds	49
4.4 Summary	50

CHAPTER 5	VALIDATION OF EMPIRICAL MODELS	52
5.1	Using Data to Update HWM	52
5.2	Comment on Measurement/Model Wind Comparisons	57
5.3	Using Data to Validate HWM14	67
5.3.1	Harmonic Analysis Methodology	69
5.3.2	Harmonic Analysis Results	73
5.3.3	Harmonic Analysis over Northeastern Brazil	77
5.3.4	Harmonic Analysis Over PARI	78
5.3.5	Harmonic Analysis over Morocco	82
5.3.6	Harmonic Analysis Discussion	85
5.4	Summary	90
CHAPTER 6	UTILIZING JOINT FPI AND ASI OBSERVATIONS TO ASSESS THE STORM-TIME DISTURBANCE DYNAMO	92
6.1	Equatorial Ionospheric Irregularities	92
6.2	Equatorial Plasma Bubble Analyses	94
6.2.1	Method 1: Cross-Correlation Analysis	94
6.2.2	Method 2: Keogram to Wind Vector Comparison	97
6.3	Comparison of Bubble Drifts and Neutral Winds	99
6.3.1	Method Validation During Quiet-Time Events	99
6.3.2	Method Implementation During Storm-Time Events	105
6.3.3	Comments on Secondary Instabilities	109
6.4	Summary	112
CHAPTER 7	CONCLUSIONS AND FUTURE DIRECTIONS	114
7.1	Contributions	114
7.2	Future Directions	116
REFERENCES	118

LIST OF ABBREVIATIONS

AACGM	Altitude Adjusted Corrected Geomagnetic
AERONET	Aerosol Robotic Network
ASI	All Sky Imager
CAJ	Cajazeiras, Brazil
CAR	Cariri, Brazil
CCD	Charge-Coupled Device
CME	Coronal Mass Ejection
CV	Common Volume
DOY	Day of Year
EPB	Equatorial Plasma Bubble
EUV	Extreme Ultraviolet
FOV	Field-of-View
FPI	Fabry-Perot Interferometer
FSR	Free Spectral Range
FWHM	Full-Width at Half-Max
GNSS	Global Navigation Satellite Systems
GPS	Global Positioning Systems
HWM	Horizontal Wind Model
LOS	Line-of-Sight
LT	Local Time

MOR	Oukaïmeden Observatory, Morocco
MSIS	Mass Spectrometer and Incoherent Scatter Model
MTM	Midnight Temperature Maximum
NATION	North American Thermosphere Ionosphere Observing Network
PAR/PARI	Pisgah Astronomic Research Institute in North Carolina, USA
RENOIR	Remote Equatorial Nighttime Observatory for Ionospheric Regions
SLT	Solar Local Time
TEC	Total Electron Content
UT/UTC	Universal Time (Greenwich Meridian Time)
UV	Ultraviolet
WAM	Whole Atmosphere Model

LIST OF SYMBOLS

E	vector electric field
B	vector magnetic field
U	vector neutral wind
V	vector plasma drift
J	vector current
u	zonal wind (east positive)
v	meridional wind (north positive)
w	vertical wind (up positive)
B	total magnetic flux
T_n	neutral temperature
T_i	ion temperature
T_e	electron temperature
$I_{630.0}$	airglow intensity
I_B	background intensity
t	time
σ_{FWHM}	full-width at half-max
α	elevation angle
θ	azimuth angle
γ	zero-Doppler offset
λ	wavelength

$\Delta\lambda$	free spectral range
c	speed of light
\mathbf{g}	gravity
K_P	K_P index
$F_{10.7}$	10.7-cm solar flux
$F_{10.7a}$	81-day average 10.7-cm solar flux
$\overline{F_{10.7}}$	filtered 10.7-cm solar flux
$hmf2$	height of the maximum F2 peak
$hmag$	height of the maximum airglow peak

CHAPTER 1

INTRODUCTION

This dissertation enhances understanding of the thermospheric neutral parameters using observations obtained from eight ground-based Fabry-Perot interferometers (FPIs). These instruments were designed to run nearly continuously, taking measurements each night of the neutral winds and temperatures from the naturally occurring redline emission. Using the long-term datasets collected from the various FPIs, we are able to monitor variations due to daily fluctuations, seasonal changes, and the solar cycle. We also compare these results between different latitudes and longitudes. Ultimately, these studies will validate and improve upper atmospheric models. This work illuminates how models, like the horizontal wind model (HWM), benefit from changes derived from actual observations. We also demonstrate how the FPI observations can be compared and contrasted against other datasets, such as all-sky imager (ASI) data, to further explain the physics of the upper atmosphere.

1.1 Motivation

The desire to understand the complex phenomena of the upper atmosphere stems from the discovery of an electric layer in the atmosphere by Marconi in 1920. Since then, scientists have focused on studying the plasma as it impacts radio wave propagation, directly affecting the users of satellite-based communication and global positioning systems. Historically, the number of measurements made of the plasma has been orders of magnitude larger than those of the collocated neutrals. This is problematic given that the plasma physics depend on the neutrals, the dominant particles in this region. While satellites have the advantage of global coverage, the measurements are limited in local time coverage. This constraint provides the rationale behind using

ground-based instruments; spatial coverage is sacrificed in order to obtain high-resolution temporal observations in local time and time of year.

The FPIs are designed to obtain estimates of the thermospheric neutral winds and temperatures. With instruments distributed in different regions, we are able to capture both spatial and temporal variations at a variety of scales. The measured parameters enable a better understanding of the physics of the upper atmosphere, including how the thermosphere and ionosphere couple. The thermospheric winds are known to drive plasma motion, and thus will affect many ionospheric phenomena.

Through the continued nightly collection of the winds and temperatures, we are able to amass a sizable dataset for the neutrals. These observations are used to both refine our understanding of the underlying physics and enhance or even correct current empirical models. The observations of the neutral winds and temperatures are crucial measurements required to improve these models, especially over the data-starved African sector. The observations are also necessary in order to accurately predict ionospheric phenomena. In order to drive these predictions, highly accurate models of the neutrals are required.

1.2 Overview

We begin by covering the characteristics of the thermosphere/ionosphere system. Chapter 2 describes the redline airglow emission and the fundamental physics that drive the typical conditions in the upper atmosphere. Then, we provide a description of the operating principles of Fabry-Perot interferometers. Chapter 3 describes the process for estimating the wind and temperature from FPI observations, as well as providing information for the systems used. Next, we describe the wind and temperature climatologies derived from the FPI datasets. Chapter 4 investigates the changes observed from daily, seasonal, and solar variations observed in the data. Then, Chapter 5 compares our FPI observations to the HWM winds utilizing a harmonic analysis technique. Following this, we explore the importance of combining FPI data with coincident ASI data. Chapter 6 details the insights gained from examples of drift/wind comparisons during geomagnetic storms. Finally, Chapter 7 summarizes the contributions of this work and outlines future research.

CHAPTER 2

THE THERMOSPHERE

The thermosphere is a region of Earth’s atmosphere exhibiting low neutral density and strong coupling with the ionosphere. We study the parameters of this region using passive optical techniques from the ground. In order to understand the significance of our long-term measurements, an understanding of the typical conditions in the upper atmosphere is first required. This chapter describes Earth’s thermosphere/ionosphere, the relevant redline airglow signal, and typical nighttime winds and temperatures for context.

2.1 Thermospheric Background

The troposphere, stratosphere, mesosphere, thermosphere, and exosphere are all neutral regions of Earth’s atmosphere differentiated by their thermal profiles. The thermosphere exists from roughly 90 to 600 km where the temperature is found to increase with altitude. It is surrounded by the mesosphere below, where temperature decreases with altitude, and the isothermal exosphere above. The left half of Figure 2.1 depicts the temperature profile of the atmosphere, including variations seen between solar minimum and maximum. Even though the atmospheric regions are distinct, chemical and energy transport exist between the layers. For example, waves generated from heating in the lowest region, the troposphere, propagate upward and deposit energy into the thermosphere [*Immel et al.*, 2006].

Since neutral density decays exponentially with height, the thermosphere is rarefied, over six orders of magnitude less dense than air on the surface. The thermosphere is also located above the turbopause, which separates where the composition is well-mixed due to turbulence (below) and where constituents are stratified through diffusion (above). Unlike the composition near Earth’s surface, which is well mixed and mostly nitrogen, the thermo-

sphere is dominated by monatomic oxygen [*Kelley, 1989*].

Additionally, the thermosphere is coincident with the ionosphere, a region with a large concentration of plasma (free ions and electrons). It extends from 60 to 1000 km, intermixing with the neutral mesosphere and exosphere as well. The ionosphere can be subdivided further into regions of peak electron density; the D region is a thin layer below 90 km, the E region is centered at 95 km, and the F region is centered at 350 km. The F region is largest, both in density (it is an order of magnitude denser than the D and E regions) and in vertical extent (covering 150 to 500 km in altitude). During the nighttime, the D and E layers quickly recombine, leaving only the F region. The right half of Figure 2.1 shows typical profiles of electron density during both the daytime and nighttime and compares them to the neutral density. Though many measurements are routinely made of the coincident ionosphere using radar, GPS, rockets, sounders, and satellites, historically, there have been significantly fewer measurements of the neutral constituents in the thermosphere. However, the layer is coupled with the 1000 times denser neutrals. Therefore, studying the neutral physics leads to a better understanding of the plasma physics.

2.2 Airglow

In order to probe the thermosphere using passive ground-based techniques, we must take advantage of the natural chemiluminescent emissions of the atmosphere called airglow. Airglow (or nightglow) occurs when a chemical reaction or photoionization causes molecular excitation where the excess energy is released in the form of light [*Herzberg, 1944*]. These atmospheric optical emissions are pervasive [*Krassovsky et al., 1962*].

We turn our focus to oxygen-related airglow emissions as oxygen is the dominant species in the thermosphere. There are three commonly observed airglow lines from oxygen: 557.7 nm, 630.0 nm, and 777.4 nm. The 557.7-nm or greenline emission mostly occurs in the mesosphere, which is below the region of interest for this work [*Rishbeth and Garriott, 1969*]. The 777.4-nm (near infrared) line is a prompt emission from the radiative recombination of ionized oxygen occurring significantly between 300 and 380 km [*Abalde, 2004*]. This emission is not useful for measuring the neutrals because the

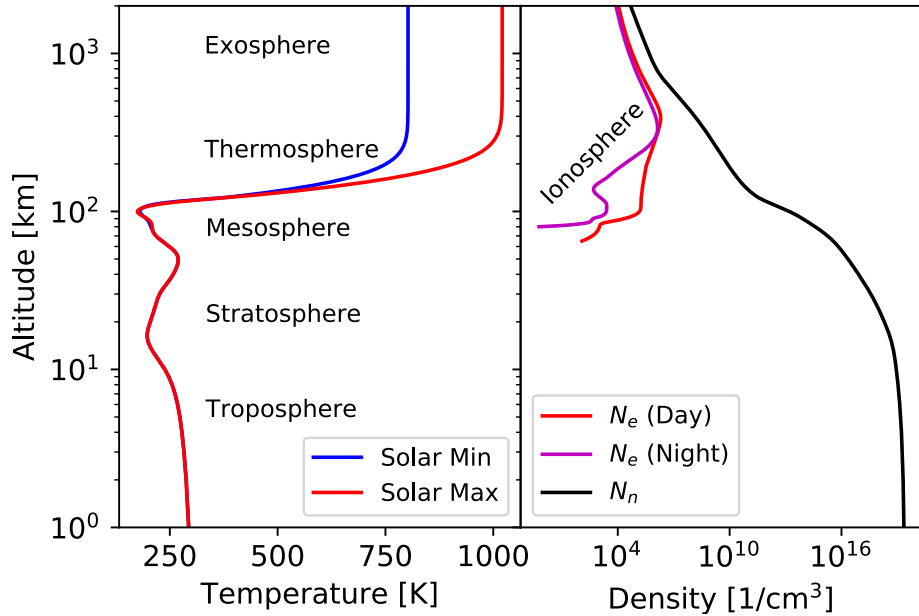


Figure 2.1: The Earth’s atmosphere profile by temperature and density. The neutrals are modeled from MSIS and ions are modeled from IRI. After *Kelley [1989]*.

radiation occurs from the ionized oxygen and thus cannot give any information on the neutral behavior. Finally, the 630.0-nm or redline emission peaks in brightness between 200 and 300 km, making it ideal for studying the thermosphere. The redline emission contains information regarding the neutral parameters of the thermosphere even though it originates from an ion species (Equation 2.2). Unlike the prompt 777.4-nm emission, the lifetime of the excited oxygen atom is 110 s, giving the particle time to thermalize with the neutrals. The collision frequency is on the order of 0.1 Hz in the thermosphere, indicating hundreds of collisions occur in the lifetime of the excited state. The redline photon occurs when metastable excited oxygen finally relaxes to the ground state:



Excited oxygen is primarily produced through the dissociative recombination of O_2^+ [*Hays et al., 1978*]:

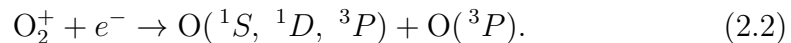


Table 2.1: Rate coefficients for 630.0-nm emission. After *Link and Cogger* [1988, 1989].

Coefficient	Rate	Units
A_{1D}	6.81 E-3	1/s
β_1	1.1	
k_1	$3.23 \text{ E-}12 \exp(3.72/(T_i/300) - 1.87/(T_i/300)^2)$	cm^3/s
k_3	$2.0 \text{ E-}11 \exp(111.8/T_n)$	cm^3/s
k_4	$2.9 \text{ E-}11 \exp(67.5/T_n)$	cm^3/s
k_5	$1.6 \text{ E-}12 T_e^{0.91}$	cm^3/s

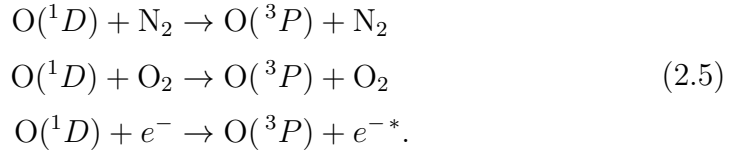
Thus, the main source of $\text{O}(^1D)$ is limited by the amount of O_2^+ reactant in this process. It is produced through an ion exchange with an ionized oxygen atom:



This, however, is not the only source for the redline emission as excited oxygen is produced through the photodissociation of O_2 [*Hays et al.*, 1978]:



Though the long lifetime of the 630.0-nm emission is required in order to remotely sense the bulk thermosphere, it also enables collisions that quench $\text{O}(^1D)$ before it can successfully emit a photon:



Using the above equations, along with laboratory-measured reaction rate coefficients, k , the volume emission rate (VER) or intensity of the nighttime redline emission can be calculated from [*Link and Cogger*, 1988]:

$$I_{630.0} = \frac{0.76 A_{1D} \beta_1 k_1 [\text{O}^+][\text{O}_2]}{A_{1D} + k_3[\text{N}_2] + k_4[\text{O}_2] + k_5[e^-]}. \quad (2.6)$$

The coefficients for the 630.0-nm reaction are in given in Table 2.1.

The volume emission rate equation shows that the production of a 630.0-nm photon is dependent on both plasma and neutral conditions. On the one hand, Equation 2.2 explains the importance of the plasma density; if more

electrons are present, there is a higher likelihood of a reaction producing an excited oxygen atom. The most electrons are found at the F-region peak around 350 km. On the other hand, Equation 2.3 explains the dependence on the neutral density; if more oxygen atoms are present, more O_2^+ will form which is needed to create more $O(^1D)$. The most neutrals are found lower in the atmosphere because density increases exponentially with decreasing altitude. As these two concentrations vary, so too will the redline peak-altitude shift. This balance causes an ambiguity in interpreting brightness changes. For example, a decrease in measured airglow intensity could be interpreted as: (1.) a decrease in dissociative recombination due to decreasing plasma density; (2.) the neutral collision rate dropping because the F region peak (hmF2) has risen in altitude, resulting in reduced ion exchange; or (3.) thermospheric neutral composition changes, causing increased quenching (Equations 2.5). The typical redline emission intensities are on the order of 100 R during the nighttime [*Takahashi et al.*, 2001]. The peak is typically located around 250 km, ranging vertically from 225 to 275 km.

2.3 Thermospheric Winds and Temperatures

Airglow intensities are not the only information that can be inferred from photon measurements. Via Doppler shifts of the photons, we can infer two crucial parameters in the thermosphere: neutral temperature and wind velocity. First, the motion of an $O(^1D)$ particle will imbue a Doppler shift to the 630.0-nm emission relative to the trajectory of the photon. Second, given an ensemble of $O(^1D)$, the individual speeds (and therefore Doppler shifts) will vary due to thermal fluctuations. Thus, the collective emitters will generate a Doppler profile following the Maxwell-Boltzmann distribution, where the peak describes the mean Doppler shift and the width is proportional to the bulk temperature. The details of extracting the correct neutral motion will be discussed further in Chapter 3. Given that the Doppler shifts and broadening are a proxy for physical parameters of the thermosphere, it is fruitful to know the underlying relevant physics. This section explains the temperatures and winds that pertain to the nighttime thermosphere in order to give a preliminary understanding of the expected observations, which are discussed in Chapter 4. We begin with a discussion of the temperatures, a

scalar quantity, and then move on to the vector winds.

The thermospheric temperature is driven primarily by solar heating. High energy UV and EUV radiation are absorbed in the upper atmosphere, driving temperatures of nearly 1000 K during the daytime. However, once the Sun sets, the thermosphere loses its energy source and the temperature decays, cooling to roughly 700 K. However, this natural diurnal cycle is not the only cause for thermal variation. The neutral temperature also fluctuates annually; solar zenith angle affects the direct heating of the thermosphere. Local summer temperatures are observed to be higher than in local winter [Roble, 1983]. Additionally, the neutral temperature varies with the 11-year solar cycle. Temperatures at night can vary from 600 K during solar minimum to over 1200 K during solar maximum [Makela *et al.*, 2011]. Models can capture this variation as shown in Figure 2.1. Another feature potentially seen in the nighttime thermosphere is the midnight temperature maximum (MTM), a seasonally varying phenomenon caused by a temperature bulge around local midnight from tidal forcing [Herrero *et al.*, 1983], leading to the poleward propagation of enhanced temperature over the course of a night.

The neutral wind, \mathbf{U} , is driven by a multitude of forces including the pressure gradient force, gravity, Coriolis force, ion-neutral collisions, and the viscosity of air. The equation of motion in the thermosphere is [Rishbeth, 2000]:

$$d\mathbf{U}/dt = \mathbf{F} - \mathbf{g} - 2\boldsymbol{\Omega} \times \mathbf{U} + \nu(\mathbf{V} - \mathbf{U}) + (\mu/\rho)\nabla^2\mathbf{U}. \quad (2.7)$$

The pressure gradient force per unit mass is denoted by \mathbf{F} , gravity, \mathbf{g} , is a downward force term, $\boldsymbol{\Omega}$ is the angular velocity of Earth (which is needed to describe the Coriolis effects), ν is the neutral-ion collision frequency, \mathbf{V} is the ion drift velocity, μ is molecular viscosity, and ρ is the density.

In general, the Sun is the major driver for wind speed and direction. The heating generated through energy absorption in the thermosphere drives a pressure gradient force. The Sun forces a dominant diurnal cycle, which is clearly evident in the nighttime winds; neutral winds are typically strongest after sunset and decay until the Sun rises. Furthermore, as the solar flux follows an 11-year solar cycle, so too should the winds. The solar driver also causes a seasonal variation; in low-latitudes, heating from the Sun causes the pressure gradient force that drives winds from the summer-to-winter hemisphere. The pressure gradient also forces zonal winds, causing an eastward

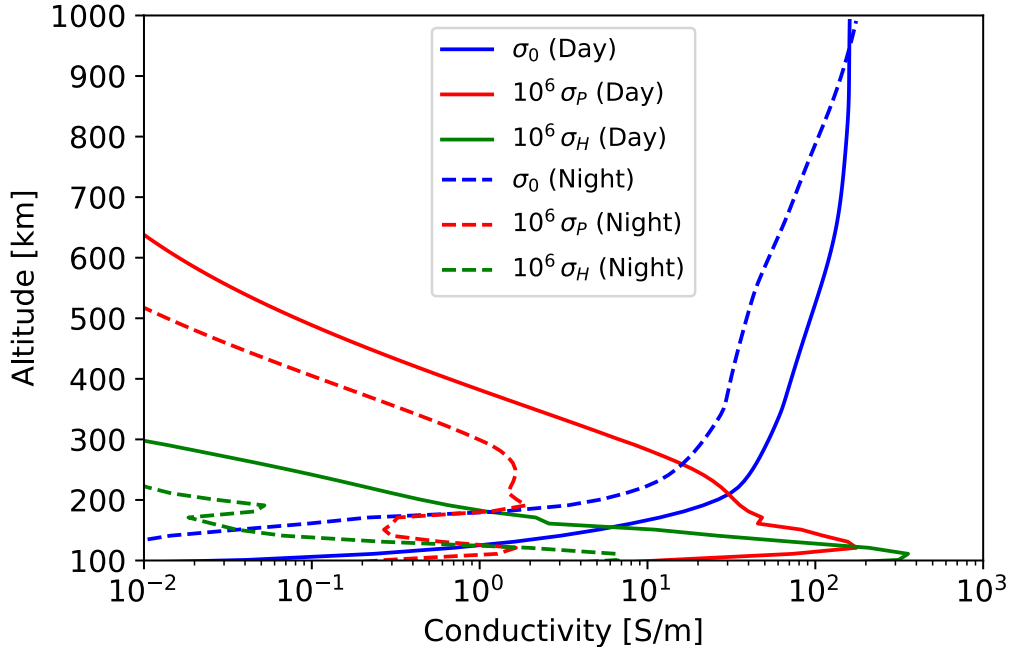


Figure 2.2: Modeled conductivity profile of the upper atmosphere on February 16, 2016. After *Kelley* [1989].

wind during the early night that eventually shifts to slightly westward at dawn. These general trends are most apparent in the low-latitude thermosphere. Moving towards the auroral region, forcing from polar cap heating must be introduced. Many studies have successfully captured the average global horizontal wind patterns [*Spencer et al.*, 1982; *Hedin et al.*, 1988; *Ridley et al.*, 2006]. The vertical winds are generally assumed to be zero, as gravitational forcing is balanced by the vertical pressure gradient force [*Dickinson and Geisler*, 1968]. However, instantaneous non-zero vertical winds have been measured in the thermosphere [*Biondi and Sipler*, 1985; *Raghavarao et al.*, 1993]. We present climatologies of the neutral horizontal winds from various sites in order to understand the average flow, as well as variations of it.

The importance of studying the neutral winds at night is that they are a driver of nighttime plasma motion. This motion occurs through a dynamo process in the F region where the mechanical motion of the neutral particles creates an electric field. In order to understand this process, we present the

equation for plasma velocity, or ion drift, as [Rishbeth, 2000]:

$$\mathbf{V} = \mathbf{V}_{\mathbf{E} \times \mathbf{B}} + \mathbf{V}_{\mathbf{U} \cdot \mathbf{B}} + \mathbf{V}_{\text{diff}} \quad (2.8)$$

where $\mathbf{V}_{\mathbf{E} \times \mathbf{B}}$ is the $\mathbf{E} \times \mathbf{B}$ drift, $\mathbf{V}_{\mathbf{U} \cdot \mathbf{B}}$ is the ion velocity from the neutral wind dragging plasma along the magnetic field lines, and \mathbf{V}_{diff} is the velocity due to plasma diffusion. The plasma speed depends on the changes in plasma concentration, the changes in temperature, gravity, and the plasma diffusion coefficient. Though we see the neutral wind vector is present in the equation, that component alone is not enough to explain the coupling. To gain a better understanding, we first model the F region as a “slab” of conductivity, ignoring the E region because it recombines nearly immediately after sunset. During the night, the neutral wind moves the conductive ionosphere across Earth’s magnetic field. The conductivity tensor, with the magnetic field, \mathbf{B} , pointing north at the equator, is defined as

$$\sigma = \begin{pmatrix} \sigma_P & -\sigma_H & 0 \\ \sigma_H & \sigma_P & 0 \\ 0 & 0 & \sigma_0 \end{pmatrix} \quad (2.9)$$

where σ_P is the Pedersen conductivity, σ_H is the Hall conductivity, and σ_0 is the parallel conductivity. A vertical profile of these values at solar maximum is given in Figure 2.2. When a conductive medium moves through a magnetic field, it creates a current. We have already noted that the primary wind is eastward at night, thus $\mathbf{U} \approx U_x$. Thus, the neutral winds will drag the ions and electrons across the magnetic field lines, creating an upward current. The current will move positive charge upward, but the ions will begin to accumulate on the edge of the conducting slab. The potential from charge separation forms a downward \mathbf{E} field and current to negate the upward current and satisfy the divergence-free condition:

$$\mathbf{J} = \sigma(\mathbf{E} + \mathbf{U} \times \mathbf{B}) = 0. \quad (2.10)$$

If we assume that diffusion is negligible, and ignore $\mathbf{V}_{\mathbf{U} \cdot \mathbf{B}}$ since $U_x \cdot \mathbf{B} = 0$, we find that Equation 2.8 reduces to

$$\mathbf{V} = \mathbf{V}_{\mathbf{E} \times \mathbf{B}} = \mathbf{E} \times \mathbf{B} / B^2 \quad (2.11)$$

where downward \mathbf{E} field crossed with \mathbf{B} leads to the typical eastward drifts during the night. $\mathbf{E} \times \mathbf{B}$ drifts are a guiding center motion in which the ions and electrons move together, and thus, it is not a current. Combining Equations 2.10 and 2.11, we find

$$\mathbf{V} = -U_x \times \mathbf{B} \times \mathbf{B}/B^2 = U_x. \quad (2.12)$$

This shows the coupling nature of \mathbf{U} ; a zonal neutral wind drives a plasma drift of equal velocity. This entire process is termed the F-region dynamo.

2.4 Geomagnetic Storms

The previous section described the thermosphere during typical calm conditions. However, these conditions can change drastically during a geomagnetic storm, which is a fluctuation of the Earth's magnetic field typically caused by solar-driven phenomena such as a coronal mass ejection (CME), a solar flare, or a high speed stream [Rees, 1995]. Changes in the solar wind are measured via satellite and the disturbances in the magnetic fields are measured via ground-based magnetometers. We choose to utilize the K_P index to identify storm periods. The K_P index classifies magnetic field disturbances from a global distribution of mid-latitude magnetometers as a number from zero to nine over a three-hour range [Menvielle and Berthelier, 1991]. Quiet times are defined when the index is less than four, and geomagnetically active times are defined when K_P is greater than four.

The changes in the solar wind during a geomagnetic storm interact with the Earth's magnetosphere, creating currents that can promptly penetrate to low latitudes through the conductive ionosphere [Blanc and Richmond, 1980]. The interaction can also change the equilibrium of the magnetic field lines and force plasma from the magnetosphere into the polar cap. The influx of particles to the polar region not only produces the aurora, but also drives currents that heat the upper atmosphere of the auroral region, a process called Joule heating. The heating causes expansion that creates an equatorward pressure surge, or traveling atmospheric disturbance (TAD), and upwelling which modifies the ratio of the constituents in the thermosphere [Buonsanto, 1999]. This pressure gradient drives the winds equatorward and the Cori-

olis force deflects these winds to the west. If the zonal winds are switched from eastward to westward (or at least greatly reduced in magnitude), this modifies the F-region dynamo. Instead of eastward drifts, westward drifts (or at least reduced eastward drifts) are generated from what is coined the “disturbance dynamo” [*Blanc and Richmond, 1980*]. The effect is greatest at mid-latitudes, but can also be seen in the low-latitude thermosphere. Additionally, the extra energy deposited in the low latitudes causes a rise in the height of the F-peak ($hmF2$) and locally increased temperatures. Later, we examine the storm-time effectiveness of the disturbance dynamo directly using joint measurements of the plasma drifts and the neutral motion.

2.5 Current Research Direction

While the general physics of the thermosphere is understood, there are inherent biases in the global studies of the thermosphere. The first bias results because most neutral wind data are collected by orbiting satellites. Numerous satellite passes over many days are required to map the neutral parameters across 24 hours of local time at a particular location. Thus, smoothing and averaging are required, effectively filtering away day-to-day and hour-to-hour variations. The second bias originates from the location of ground-based instruments. A majority of such instruments are deployed in the northern hemisphere, specifically clustered in North America, Europe, and Asia. Only through collecting neutral data from diverse stationary locations can we learn of both small-scale and large-scale features of the thermosphere across the entire globe.

Measurements of the neutral winds and temperatures have captured the monthly trends of the thermosphere. Still, variations on timescales of days to years, as well as geographic variations, are not yet fully understood. Our long-term data enable the study of variations seen in the neutral parameters over days, months, and years from a few latitude and longitude sectors. Empirical models do well in capturing the climatological winds and temperatures of the thermosphere; however, they are not perfect due to the biases mentioned above. Our long-term dataset will show both when (local time and seasonally) and where (geographically) neutral models, specifically the horizontal wind model, can be trusted. The same dataset can also be used

to improve the model, be it through data ingestion or implementing new harmonic fits to the data.

It is known that in the thermosphere, the dynamo effect is the driver of plasma motion at night. Direct measurements of plasma motion have been made in both quiet times [*Fejer et al.*, 1979, 1991; *Martinis*, 2003] and storm times [*Scherliess and Fejer*, 1997; *Abdu et al.*, 1998; *Knipp et al.*, 1998; *Santos et al.*, 2016a], and there are many measurements of quiet-time and storm-time neutral winds [*Salah et al.*, 1996; *Fejer et al.*, 2002; *Emmert et al.*, 2006; *Meriwether et al.*, 2011; *Brum et al.*, 2012]. There have even been coincident measurements of the drifts and neutral winds during quiet times [*Biondi et al.*, 1988; *Basu et al.*, 1996; *Valladares et al.*, 2002; *Chapagain et al.*, 2012, 2013]. However, we will present how well the disturbance dynamo functions during storm times using joint measurements of the winds and drifts.

CHAPTER 3

INSTRUMENTATION FOR AIRGLOW MEASUREMENTS

In-situ measurements of the thermosphere can be made with satellites or chemical releases from rockets. A satellite is extremely costly and sacrifices temporal resolution for global coverage. Unfortunately, rockets are also costly and only work for a single release. Therefore, many observations of the thermosphere are made passively using remote sensing from the ground. One way to probe the thermosphere is to use passive optical instrumentation to capture natural chemiluminescent emissions called airglow (see Section 2.2). The Fabry-Perot interferometer (FPI) and all-sky imager (ASI) are two instruments designed to measure these emissions. The focus of this work is to analyze the nighttime thermospheric parameters collected by FPIs. This chapter will explain the FPI instrument and how it extracts useful wind and temperature estimates from an airglow spectrum. The chapter also provides an overview of the instruments used for this study and the data products produced.

3.1 The Fabry-Perot Interferometer

In 1923, the first Fabry-Perot interferometer observations of the aurora were made by *Babcock* [1923]. Fifty years later, Hernandez and Roble were the first to record measurements of thermospheric winds and temperatures using the 630.0-nm emission [*Hernandez and Roble*, 1976a]. Today, many more FPIs are distributed around the globe probing the thermosphere via the redline emission [*Meriwether and Biondi*, 1995; *Fejer et al.*, 2002; *Ford et al.*, 2006; *Meriwether et al.*, 2011; *Brum et al.*, 2012; *Makela et al.*, 2012; *Liu et al.*, 2014; *Yu et al.*, 2014]. The resultant datasets, along with space-based satellite data, are used to study coupling mechanisms in the upper atmosphere, validate physics-based models of the upper atmosphere [*Chartier*

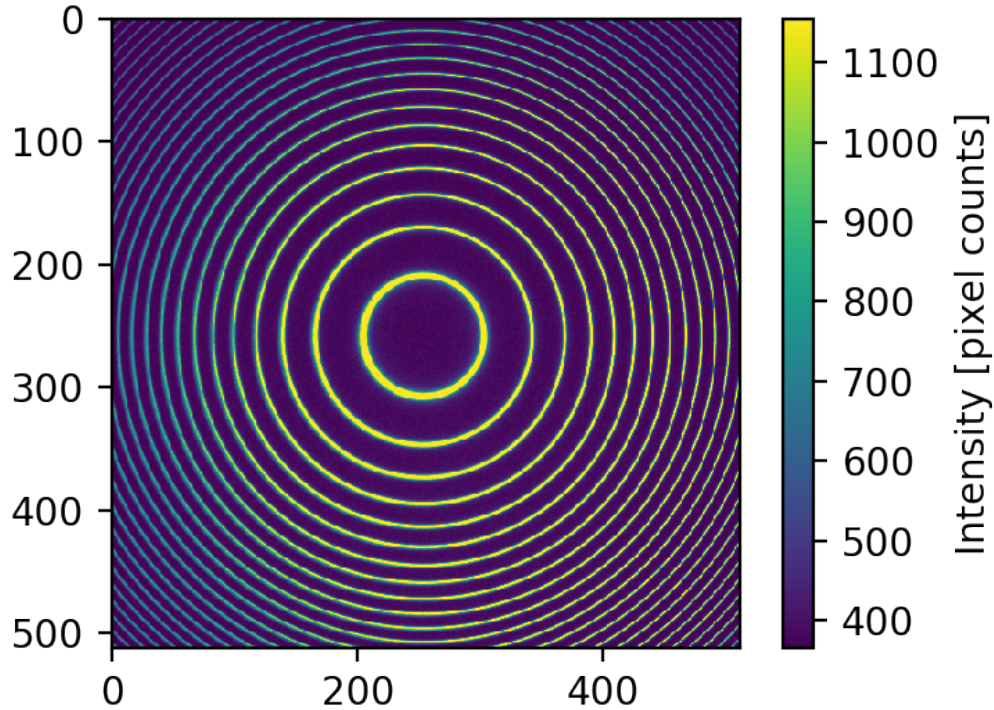


Figure 3.1: Typical Airy pattern imaged on a CCD after a near-monochromatic light source (here a frequency-stabilized HeNe laser) passes through the etalon.

et al., 2015], and improve empirical models of the thermosphere [Drob *et al.*, 2015]. However, measurements of the neutrals, especially in the southern hemisphere, still remain an under-sampled quantity in the study of the upper atmosphere.

The Fabry-Perot interferometer is an imaging system which consists of a filter, CCD, lens, and an etalon. An etalon is composed of two partially reflective surfaces separated by a gap. The properties of this gap determine the phase offset of the reflected copies of the light that enters the etalon. These transmitted copies will then constructively and destructively interfere on the CCD where they produce an Airy interference pattern. A full mathematical derivation of the Airy function is given in Fisher [2013]. An example of this interference pattern can be seen in Figure 3.1.

Since our goal is to capture the redline emission, a narrowband redline filter is placed before the etalon to isolate the emission. The airglow spectra, or spectral lineshape, typically fit a Maxwell-Boltzmann distribution, leading to the captured image on the CCD essentially being the convolution of the

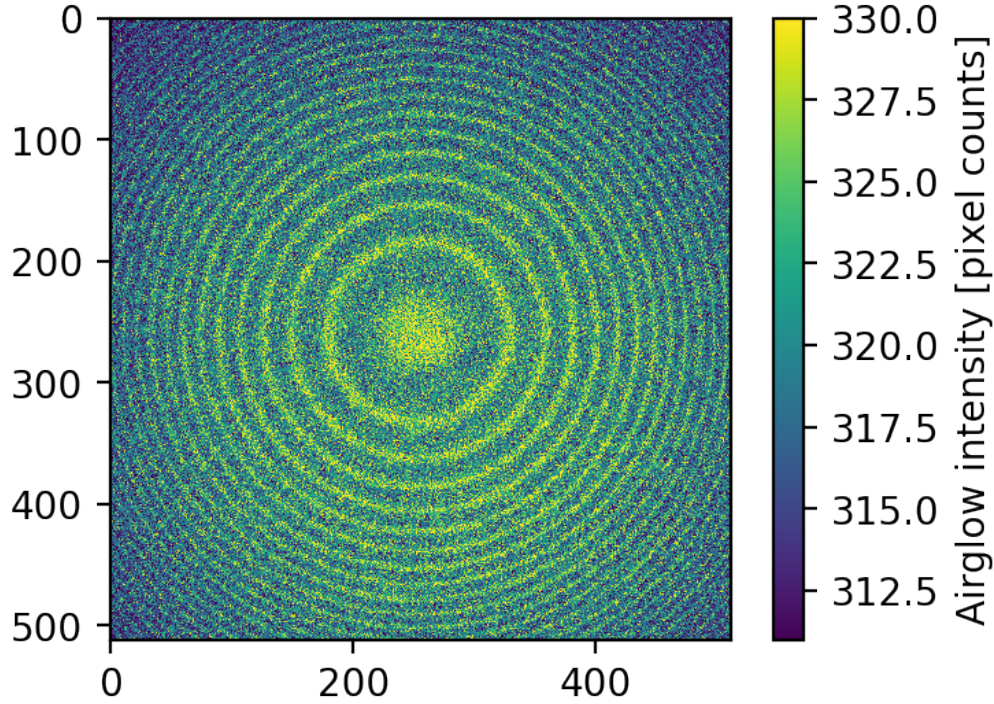


Figure 3.2: Typical pattern imaged on a CCD when observing the redline emission. This raw data product is called an interferogram.

airglow signal (Gaussian) with the instrument function (Airy pattern). An example of the resulting interference pattern is shown in Figure 3.2.

If the spectral lineshape of the 630.0-nm redline emission can be estimated from this image, it can be used to calculate the thermospheric wind and temperature from the Doppler shift and broadening of this emission's lineshape. A single fringe theoretically contains all the information needed to obtain these parameters. Figure 3.3 shows the four main signal parameters that will be retrieved from a single spectrum: background intensity, signal intensity, Doppler broadening, and Doppler shift. The background intensity, I_B , is a measure of the noise level in the image as well as the contribution of the sky continuum. The airglow intensity is a measure of the integral of the lineshape minus I_B and is proportional to $I_{630.0}$ (see Equation 2.6). The neutral temperature, T_n , is proportional to the Doppler broadened width, σ_{FWHM} :

$$T_n = \frac{\sigma_{FWHM}^2 m}{2k} \quad (3.1)$$

where k is Boltzmann's constant and m is the mass of the constituent (oxy-

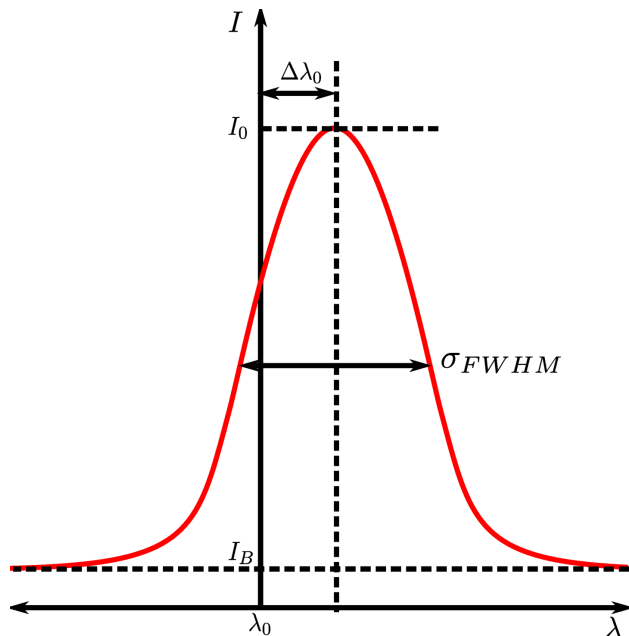


Figure 3.3: Signal parameters obtained from the measurements of a single fringe.

gen) [Makela et al., 2011]. The line-of-sight wind, U^{LOS} , can be determined using the wavelength shift, $\Delta\lambda_0$, from the Doppler equation:

$$U^{\text{LOS}} = \left(\frac{\Delta\lambda_0}{\lambda_0} \right) c. \quad (3.2)$$

While identifying the relative linecenter position is straightforward, the difficulty in estimating U^{LOS} lies in knowing the location of λ_0 relative to the linecenter peak. There is no 630.0-nm lab source that can be used for Doppler calibration, and instead, we must use another means to have a zero-Doppler reference. Obtaining a proper zero-Doppler reference is crucial in determining the correct absolute Doppler shift, and correct wind estimate, and will be discussed further in Section 3.2.1.

3.2 Our Instrumentation

Between 2009 and 2013, we assisted in deploying eight redline imaging FPIs for long-term thermospheric studies. In 2009, two ground-based Fabry-Perot interferometers were installed in northeastern Brazil as part of the Remote Equatorial Nighttime Observatory for Ionospheric Regions (RENOIR)

project. Included in the RENOIR project are two FPIs, an airglow ASI, a dual-frequency GPS receiver for measuring total electron content (TEC), and two GPS-based scintillation monitors. These instruments are distributed between two sites: one is located on a campus in the city of Cajazeiras and the other just outside Cariri. The two RENOIR FPIs have collected nearly continuous airglow brightnesses, neutral temperatures, and neutral wind measurements from August 2009 to August 2014 (when both instruments broke) providing a robust dataset of low-latitude thermospheric parameters spanning solar minimum through solar maximum. The Cariri FPI was repaired using parts from the Cajazeiras FPI and returned to nightly operation from August 2015 to June 2016, further expanding this dataset.

During the years of 2011 to 2013, five FPIs were deployed in the mid-west and east-central United States. These five instruments were installed as the framework for the North American Thermosphere Ionosphere Observing Network (NATION), a collection of FPIs covering the United States. The first was deployed in Pisgah Astronomical Research Institute (PARI), North Carolina, in 2011. In 2012, one was installed in Peach Mountain, Michigan, another outside of Urbana, Illinois, and a third at Eastern Kentucky University. In 2013, the final FPI of the initial set was installed near Virginia Tech. As of January 1, 2017, only the instruments at PARI and Urbana remain in nightly operation.

Finally, near the end of 2013, an FPI and ASI were deployed at Oukaïmeden Observatory in Morocco. These represent the first long-term ground-based instruments making measurements of the thermosphere in the African sector. An overview of all these sites, including locations and dates operational, is given in Table 3.1. We also include the total number of high-quality measurements utilized in this work (see Sections 3.2.1 and 3.2.2 for details on the filtering criteria used to obtain these totals).

While the instruments are not identical, the main design of the FPI remains the same. Each consists of an etalon with an air gap of 15 mm and a $\sim 77\%$ partially reflective coating. A 0.7-nm narrowband filter centered at 630.0 nm with $\sim 55\%$ transmission is placed in the optical path before the etalon to isolate the redline emission. This design forces the free spectral range, or the maximum wavelength change that can be unambiguously resolved, to be 13.2 pm. This translates to an unambiguous velocity of ± 3147 m/s, which easily covers all potential physical ranges of the neutral wind speed.

Table 3.1: Information on the FPIs analyzed in this work. Magnetic latitude is derived using the altitude adjusted corrected geomagnetic (AACGM) coordinate transformation at 250 km in altitude during 2015. Present denotes instruments that are still operational as of January 1, 2017. The number of filtered measurements indicates the total number of high-quality, filtered data points used in this work; this amount is 20 to 60% of the total measurements made per site.

Site	Location	Country	Lat	Lon.	Geomagnetic Lat.	Dates Operational	# Filtered Measurements
CAR	Cairi	Brazil	-7.4	-36.5	-10.7	Aug '09 - Jun '16	148,584
CAJ	Cajazeiras	Brazil	-6.9	-38.6	-10.0	Sep '09 - Aug '14	109,743
MOR	Oukaimeden Observatory	Morocco	31.2	-7.9	21.6	Nov '13 - Present	79,342
UAO	Urbana Aeronomy Observatory	USA	40.2	-88.2	51.0	Jul '12 - Present	164,356
PAR	Pisgah Astronomical Research Institute	USA	35.2	-82.9	46.2	Jun '11 - Present	165,125
EKU	Eastern Kentucky University	USA	37.8	-84.3	48.7	Jul '12 - Jul '15	61,397
ANN	Peach Mountain, Michigan	USA	42.3	-83.8	52.9	Jun '12 - Feb '16	83,122
VTI	Virginia Tech	USA	37.2	-80.4	48.0	Aug '13 - Feb '16	93,289

An objective lens focuses the image onto a 13.3×13.3 mm, 1024×1024 pixel Andor CCD. The CCD chip is thermoelectrically cooled to below -60°C to reduce dark noise. This FPI design has certain advantages over previous FPI instruments. It uses a new high-quality CCD, which provides very low noise, high-resolution images of the airglow spectra. This greatly reduces the uncertainties of the winds as compared to studies done just decades prior, and allows a very high cadence of images to be taken. The use of a HeNe laser as a stable source to determine the instrument function greatly improves the accuracy of our neutral observations.

In order to collect measurements in different look directions, a dual-mirror sky-scanning system, controlled by a SmartMotor on each axis, sits above the optics to steer the FPI's 1.8° field-of-view. The system's pointing accuracy is calibrated to within 0.1° . The standard data collection process cycles through taking measurements to the north, east, south, and west at a 45° elevation angle followed by a zenith exposure. This is known as "cardinal mode," and permits meridional and zonal winds to be extracted with minimal assumptions. The left panel of Figure 3.4 shows the look directions for this configuration, assuming the vector points to the 250 km emission altitude, for the Brazilian instruments. In addition to this standard observing mode, instruments placed in close proximity can be configured to enter a "common volume" (CV) mode. This observing geometry synchronizes the FPIs to allow them to view the same point in the sky at the same time. This mode adds an inline point from which a vertical wind estimate can be made as well as two CV points that enable a complete horizontal wind vector to be estimated. These three look directions are shown for the RENOIR instruments in the right panel of Figure 3.4 projected to 250 km. During short-term campaigns, the data-collection cycles have included additional modes that interlaced with the cardinal or CV modes: an ordinal mode to add more radial measurements for wind-field fitting, an along-**B** measurement to study potential high-speed winds along the field lines, and a tri-static mode to determine instrument biases. All measurements made in any of these three non-standard modes have been discarded for this study, as geographically meaningful winds cannot be deduced from them without making additional assumptions.

Exposure times for all sky images are typically varied from 20 to 480 s, depending on the airglow intensity. No observations are made in the general direction of the moon as it overwhelms the airglow signal. The system

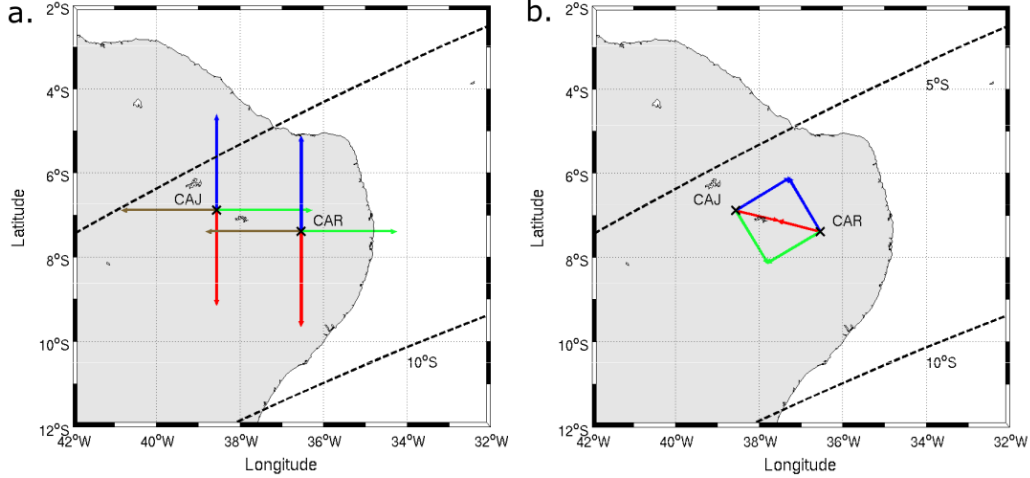


Figure 3.4: The two Brazilian FPI locations with vectors depicting (a.) the cardinal look directions; and (b.) the common volume look directions.

interleaves exposures of a 632.8-nm frequency-stabilized HeNe laser which are used to monitor the instrument function over the night. Additionally, a cloud sensor was installed at each location in order to better determine the presence of clouds which degrade data quality.

3.2.1 Data Processing

An overview of the FPI data processing is given here. A more complete description is given by *Harding et al.* [2014]. In order to analyze the airglow data, the laser images are first analyzed to estimate the instrument function. First the center of the Airy pattern must be found in order to perform an annular summation. This summation collapses the 2-D interferogram into a 1-D fringe pattern, similar in methodology to *Killeen and Hays* [1984]. However, our method improves upon this analysis by fitting the entire fringe pattern rather than individual fringes, using a modeled Airy function:

$$I(\phi) = I_0 / (1 + F \sin^2(\phi/2)) \quad (3.3)$$

where $F = 4R / (1 - R)^2$ is the coefficient of finesse and $\phi = \left(\frac{2\pi}{\lambda}\right) 2dn \cos(\psi)$ is the optical path difference phase lag [Vaughan, 1989]. Here, R is reflectivity of the etalon coating, d is the distance between the etalon plates, n is the refractive index of the gap material (air), and ψ is the incident angle

of the incoming light. A Levenberg-Marquardt inversion uses the modeled Airy function to infer the etalon parameters from the fringes. This allows varying parameters of the FPI, such as etalon gap, reflectivity, and blurring, to be tracked over time and applied to the airglow images. The airglow images undergo the same analysis as the laser images, first converted to a 1-D fringe pattern and then analyzed with the Levenberg-Marquardt inversion. This inversion assumes knowledge of the instrument parameters, which are interpolated from the analysis of the laser exposures, and uses them to estimate the airglow spectrum parameters (as seen in Figure 3.3). All temperature (Doppler broadening) and wind (Doppler shift) estimates include an uncertainty calculated by the Levenberg-Marquardt algorithm.

The winds estimated from the images are projections of the 3-D wind vector onto the instrument’s line-of-sight. In order to get winds in geographic coordinates, they must be rotated into a geographic coordinate frame, which can be done using the following equation:

$$U^{\text{LOS}} = w \sin(\alpha) + [v \cos(\theta) + u \sin(\theta)] \cos(\alpha) + \gamma. \quad (3.4)$$

Here, u , v , and w are the eastward, northward, and upward wind components, respectively, θ is the azimuth angle, α is the elevation angle, and γ is the zero-Doppler offset. For zenith measurements, the line-of-sight measurement is the estimated vertical wind:

$$\hat{w} = U^{\text{zenith}} - \gamma. \quad (3.5)$$

For cardinal measurements, this involves using an elevation-angle cosine correction factor to map the winds to a meridional or zonal direction, as well as interpolating the estimated vertical wind to this position:

$$\hat{u} \text{ or } \hat{v} = \frac{U^{\text{cardinal}} - \tilde{w} \sin(\alpha) - \gamma}{\cos(\alpha)}. \quad (3.6)$$

In this case, α maps the measurement down to the horizontal plane while θ (which has been factored out above) maps the measurement to the zonal or meridional direction. For common volume measurements, the two near-simultaneous observations of the same location are processed together to get both a zonal and meridional wind projection (see *Fisher* [2013] for more

details). Both these projections assume that there are no spatial gradients in the vertical wind.

As mentioned above, one issue in estimating the absolute wind values is that the Doppler line-center position is not known exactly, but only relatively. In order to resolve this, a zero-Doppler offset (γ) is estimated from the data and added to the line-centers to recover the absolute position. Historically, vertical winds have been assumed to be zero since the neutral density and pressure are assumed to be in hydrostatic equilibrium. Typical measurements of vertical winds presented in prior studies have been made showing them to be more than an order of magnitude smaller than the horizontal winds. When the estimated uncertainties are as large or larger than the estimated vertical winds, they can be assumed to be zero and will have a negligible effect on horizontal wind estimates (Equation 3.6). If the vertical winds are zero throughout the night, the zenith estimated wind can be set as the zero-Doppler offset (Equation 3.5). Essentially, the vertical wind estimate tracks the instrument drift. In order to loosen this vertical wind constraint, the FPI observes a frequency-stabilized HeNe laser to track the instrument parameters over the night. Then, our analysis finds γ by assuming the mode of the vertical winds across the night is zero. This method both accounts for instrument drift and allows for instantaneous vertical winds to exist during the night.

An example of a single night of processed data is displayed in Figure 3.5. In practice, our instrument can measure winds to within 2 m/s and temperatures to within 6.5 K [*Harding et al.*, 2014]. For reference, and to demonstrate the instrument sensitivity, a 10 m/s LOS wind speed is equivalent to the spectrum peak shifting only 210 fm.

The reliability of our measurements further increased after adding a cloud sensor to the sites. The cloud sensor measures the difference between the sky temperature and the ground temperature and uses it as an indicator of cloud cover. From empirical studies comparing ASI data with the cloud-sensor data, we were able to set two limits: (1.) if the temperature difference is greater than -10 C, the sky is cloudy and (2.) if the temperature difference is less than -25 C, the sky is clear and the data are assumed to be good. Similarly, tracking the CCD temperature can assist in data quality control: if the CCD cools below -60 C, the data are nominal; if the CCD is above this limit, there is a chance the fringes are too noisy to infer reliable spectral

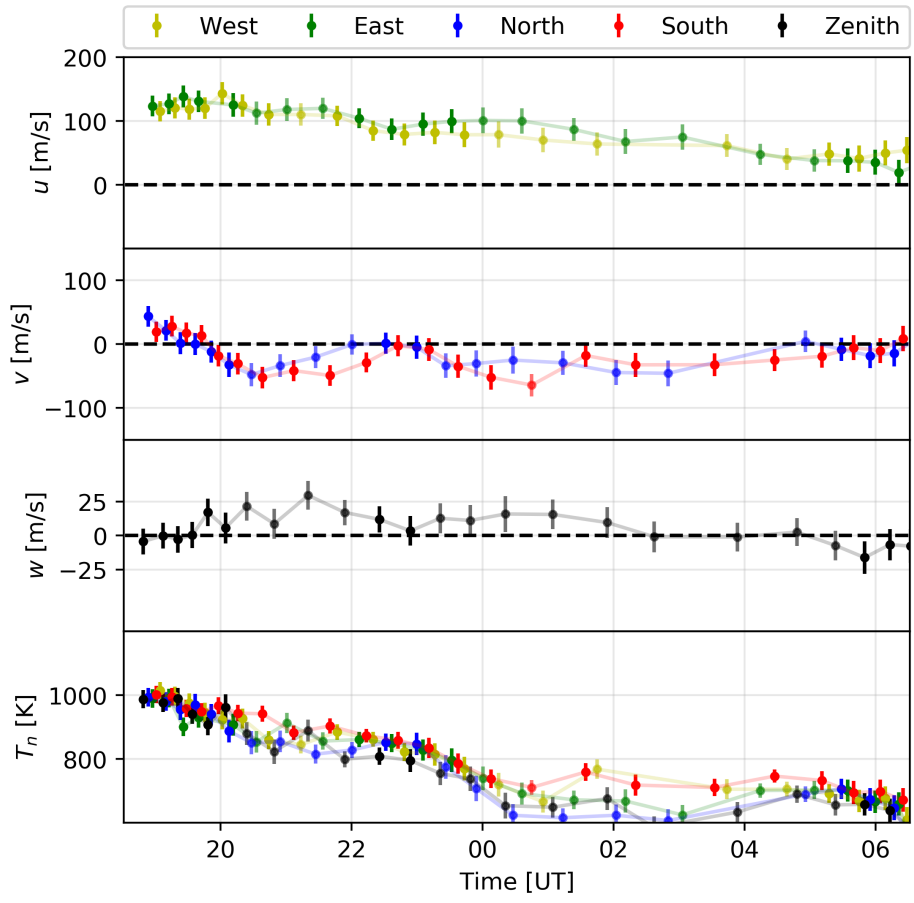


Figure 3.5: Neutral wind and temperature estimates from a single night of observations over Morocco on February 9, 2016.

estimates. Moonlight contamination could also affect the data quality.

The daily processing was initially a manual (and unsystematic) task requiring a binary classification of each individual airglow measurement. We have created a three-tiered, automated data quality control system: the data are flagged as either good, use with caution, or bad. Quality flags are set to cautionary if the laser fit drifts excessively over the night, the airglow intensity is too low, clouds are potentially present, or the CCD is too hot. If no cloud sensor data is present or no laser images are taken, the caution flag is also set. The bad data flag is set if clouds are certainly present (for winds only), the wind uncertainty is greater than 100 m/s, or the temperature uncertainty is greater than 100 K.

3.2.2 Climatological Processing

Given the large amount of data that are automatically processed each night, it becomes possible to bin and average the data in order to see long-term trends in the measurements. Although only data flagged as good and cautious are used here, quality-control processing is not perfect and erroneous data do pass through the automated checks. Thus, some filtering is needed to discard potentially erroneous measurements from the monthly averages presented in this work. We choose to err on the side of caution and employ more stringent filtering, removing measurements with temperature uncertainties larger than 50 K or wind fit uncertainties greater than 25 m/s. Additionally, the analysis tends to return unrealistically low temperatures when the signal-to-noise ratio in the raw interferograms is very low. Thus, observations are removed during periods of low signal intensity when the estimated neutral temperature drops below 600 K. Finally, the data are removed from consideration if the estimated zonal wind is greater than 200 m/s or less than -100 m/s or if the estimated meridional wind is greater than 150 m/s or less than -150 m/s. For quiet conditions, measurements outside these ranges are not physical and generally indicative of a problem with the laser calibration used to estimate the instrument's stability. Since each observation results in an estimate of both a temperature and wind, we assume that if either one needs to be removed, they both are suspect and are not included in the average. In this work, we shall refer to this culled data as high-quality.

The FPI measurements that remain after quality control are sorted into 30-minute solar local time bins for each month of observation at each site. All meridional wind estimates from a separate site are combined, whether obtained looking to the north or south in cardinal mode or from the meridional component in CV observations. Likewise, all zonal wind estimates are combined. Neutral temperatures obtained from all look-directions are combined, as well. Small spatial and temporal gradients are removed in this binning process. However, since each FPI instrument only observes a 5×5 degree latitude-longitude area, this smoothing is expected to produce mean values comparable in time and area to the values extracted from most thermospheric models.

For each time bin in each month, statistics are gathered for every parameter, and the weighted mean and sample standard deviation (variability) are computed. For a given parameter, x , where x is the set of zonal wind, meridional wind, vertical wind, or neutral temperature, the weighted mean is given by

$$\bar{x} = \frac{\sum_i x_i w_i}{\sum_i w_i} \quad (3.7)$$

where $w_i = \frac{1}{\sigma_i^2}$ are the weights and σ_i is the uncertainty of the i^{th} measurement. The day-to-day variability of parameter x , or the sample standard deviation s , is given by

$$s = \sqrt{\frac{1}{n-1} \sum_i (x_i - \bar{x})^2} \quad (3.8)$$

where n is the number of samples x .

CHAPTER 4

CLIMATOLOGICAL STUDIES OF NEUTRAL WINDS AND TEMPERATURES

Utilizing the long-term datasets collected of thermospheric neutrals from many sites, we can analyze the large-scale patterns seen in the neutral winds and temperatures. Furthermore, we can observe variations in different longitude/latitude sectors, as well as those caused by changes in solar output. This chapter focuses solely on the analysis of the neutral parameters from these climatological studies. Such studies enable an understanding of how typical conditions change due to the day-to-day fluctuations, latitude/longitude differences, seasonal dependences, and solar cycle dependence, while differentiating these from storm-time effects. The study is based on work published in *Fisher et al.* [2015].

4.1 Climatological Analysis Methodology

To study these variations, data from Brazil, the United States, and Morocco are compared. The data from the Brazilian sector is from both Cariri and Cajazeiras between August 2009 and August 2014. This near-continuous dataset is the same presented in *Fisher et al.* [2015], which expanded upon the first Brazilian climatological analysis by *Meriwether et al.* [2011]. After this period, both instruments were in need of repair. There were enough working parts between the two systems to keep the Cariri FPI operating intermittently until June 2016. This document utilizes all the available high-quality data. The two sites are separated by only 232 km, and so data from the two sites are combined to increase the temporal coverage over this sector. Since we are concerned with climatological averages, the slight separation between the two sites is considered negligible. Figure 4.1 shows that the monthly trends at both sites are nearly identical, indicating that we can combine the datasets.

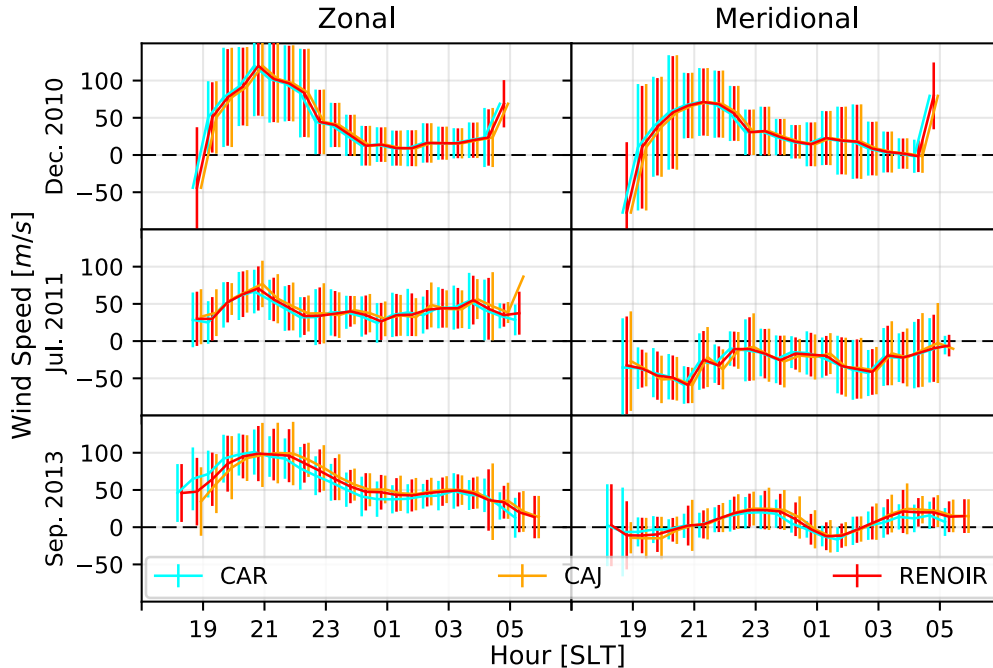


Figure 4.1: Comparison of the monthly averaged, quiet-time horizontal winds for Cariri, Cajazeiras, and RENOIR (Cariri and Cajazeiras combined) for three distinct months when both sites were operating.

To facilitate latitudinal and longitudinal comparisons, we include climatologies from two similar mid-latitude sites: one at Pisgah Astronomical Research Institute (PARI) in North Carolina, USA, and one at Oukaïmeden Observatory in Morocco (MOR). While PARI has been operating since June 2011, the Moroccan site was installed in October 2013. Both have been in nearly continuous operation since deployment. All available, high-quality data through December 2016 will be used. This adds an additional two years of data to what was reported in *Fisher et al.* [2015].

4.1.1 Sorting by Solar Flux

The 11-year solar cycle results in a fluctuating energy output from the sun which directly drives changes seen in the thermosphere, with differences in the neutral temperature being most affected by the changes in flux [*Mayr et al.*, 1978]. In order to observe solar cycle trends in the data, we have sorted each FPI measurement by low ($\overline{F_{10.7}} < 125$) or high ($\overline{F_{10.7}} \geq 125$) solar flux conditions. $F_{10.7}$ is an index used to indicate solar activity based

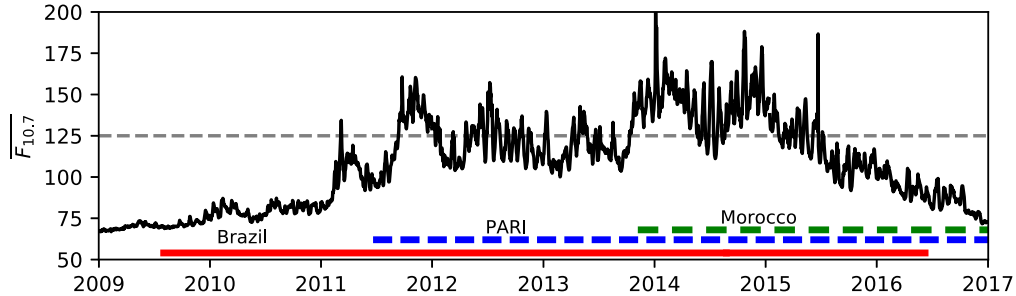


Figure 4.2: $\overline{F_{10.7}}$ from 2009 to 2017 with bars showing the approximate interval when data are available from each site. After *Fisher et al.* [2015].

on the average measured radio flux at the wavelength of 10.7 cm over one hour, reported in solar flux units ($\text{SFU} = 10^{-22} \text{ W s/m}^2$). Here, we utilize a filtered version of $F_{10.7}$ defined as

$$\overline{F_{10.7}} = (F_{10.7a} + F_{10.7})/2 \quad (4.1)$$

where $F_{10.7a}$ is an 81 day average of $F_{10.7}$. The choice was made to use this proxy for $F_{10.7}$ because the thermospheric response to solar input depends on both the current state of the thermosphere/ionosphere (influenced by past solar flux events) and the current input [*Brum et al.*, 2012]. Figure 4.2 shows the past eight years of $\overline{F_{10.7}}$ along with the dates when our FPIs were operating.

Given the availability of data from the two sites in Brazil, the dataset contains measurements from solar minimum at the beginning of solar cycle 24 to the peak in solar activity and declining phase of solar cycle 24. The sun was extremely inactive in a deep minimum between solar cycle 23 and 24, resulting in a range of $\overline{F_{10.7}}$ from 69 to 202 SFU. Data collected from the two mid-latitude sites span a minimum $\overline{F_{10.7}}$ of 72 SFU and a maximum of 202 SFU.

Although sorting by solar flux will allow solar variations to be analyzed, we must be careful to not draw biased conclusions from potential sampling irregularities inherent in binning the data with an additional dimension. There are two factors that need to be addressed before analyzing the solar cycle effects, as larger solar flux changes are likely to lead to larger changes in the thermosphere. The first deals with non-uniform sampling of the FPI observations. The instruments run nearly continuously night-to-night, but issues

arise causing small gaps in the dataset. However, even if the instruments operated flawlessly, there would still be non-uniformities. Since the observations are made with a dynamically changing integration time, the number of samples per 30-minute bin will vary with airglow brightness. Also, observations are not made toward the moon, causing further non-uniformity. Additionally, cloudy data are discarded, causing further inhomogeneity in the binning. Simple monthly climatologies that only sort by local time and month can handle this; however, the problem is compounded when you factor in the extra dimension of solar cycle. $\overline{F_{10.7}}$ fluctuates greatly each month, meaning that direct month-to-month comparisons are complicated as the amount of solar flux is not the same in each. To enable comparisons, we quantify the average $\overline{F_{10.7}}$ value for our climatological analyses. Since the value of $\overline{F_{10.7}}$ varies daily, it is a weighted average:

$$\overline{F_{10.7}} = \frac{\sum_i \overline{F_{10.7i}} n_i}{\sum_i n_i} \quad (4.2)$$

where n_i is the number of measurements on the i^{th} night. Note that the average $\overline{F_{10.7}}$ values are calculated for each local-time bin, for each month, for each flux condition, for each site and are presented in Section 4.2. We reiterate that care must be taken when discussing the monthly differences due to solar flux.

4.1.2 Three Climatological Analyses

Using monthly climatologies, we will describe the seasonal, solar, and geographic variations observed in the neutral winds and temperatures over northeastern Brazil, PARI, and Morocco. Each site will be discussed individually. The 30-minute binning and weighted monthly averaging methodology described in Section 3.2.2 will be used here, enabling both local time and seasonal (monthly) features to be observed while mitigating any conflation of the causes. All of the data presented are from geomagnetically quiet periods when K_p is less than 4. Geomagnetic activity is another cause of variation in the neutrals but will not be discussed in this chapter. Only high-quality data points are used.

First, we comment on the variations in the monthly trends of the measured neutral parameters. This will be done using days with low solar flux as defined above. This climatology removes solar cycle effects, revealing daily and seasonal variations. The monthly neutral winds and temperatures will show the “baseline” state of the thermosphere.

Second, we comment on the variations in the trends of the measured neutral parameters due to the solar cycle. The low solar flux baseline is subtracted from the high solar flux climatologies to show the differences solely caused by changing solar inputs. Local time and monthly variations due to solar flux changes can still be observed.

Finally, with a growing number of FPIs in operation, it is possible to study the geographic differences in the seasonal wind dynamics. We comment on the variations in the trends of the measured neutral parameters between the different sites. Instead of using solar flux, we bin by individual months of a single year. The months used require all three instruments to be running simultaneously for a majority of the month.

4.2 Climatological Results

First shown are the low solar flux baseline climatologies. Figure 4.3 shows the neutral temperature climatologies, Figure 4.4 shows the zonal wind climatologies, and Figure 4.5 shows the meridional wind climatologies. The three regions are plotted together, with red denoting Brazilian measurements, blue denoting PARI measurements, and green denoting Moroccan measurements. The monthly sample variance or day-to-day variability of these observations is presented as an error bar. Additionally, each figure is plotted in solar local time (SLT) to facilitate comparisons between different longitudes.

Next, we present the solar variations seen in the FPI data as the difference between low solar flux and high solar flux. We display the differential neutral temperature climatologies in Figure 4.6, the differential zonal wind climatologies in Figure 4.7, and the differential meridional wind climatologies in Figure 4.8. Similar to the prior figures, the day-to-day variability of the high solar flux observations is presented as an error bar. It is worth noting that PARI has very few measurements from August in high solar flux conditions, so no conclusions should be drawn from PARI during this month.

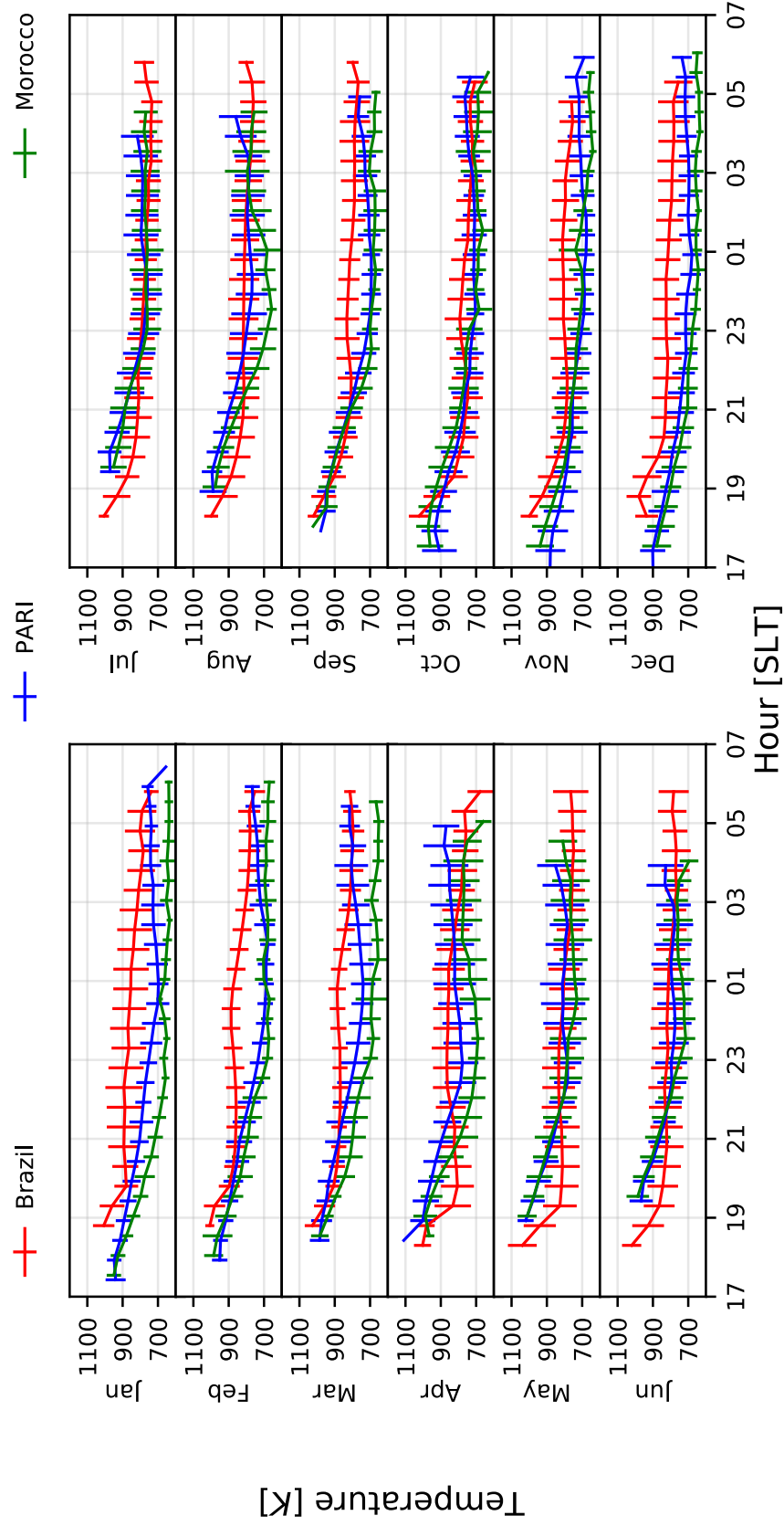


Figure 4.3: Climatologies of the thermospheric temperature during solar quiet times.

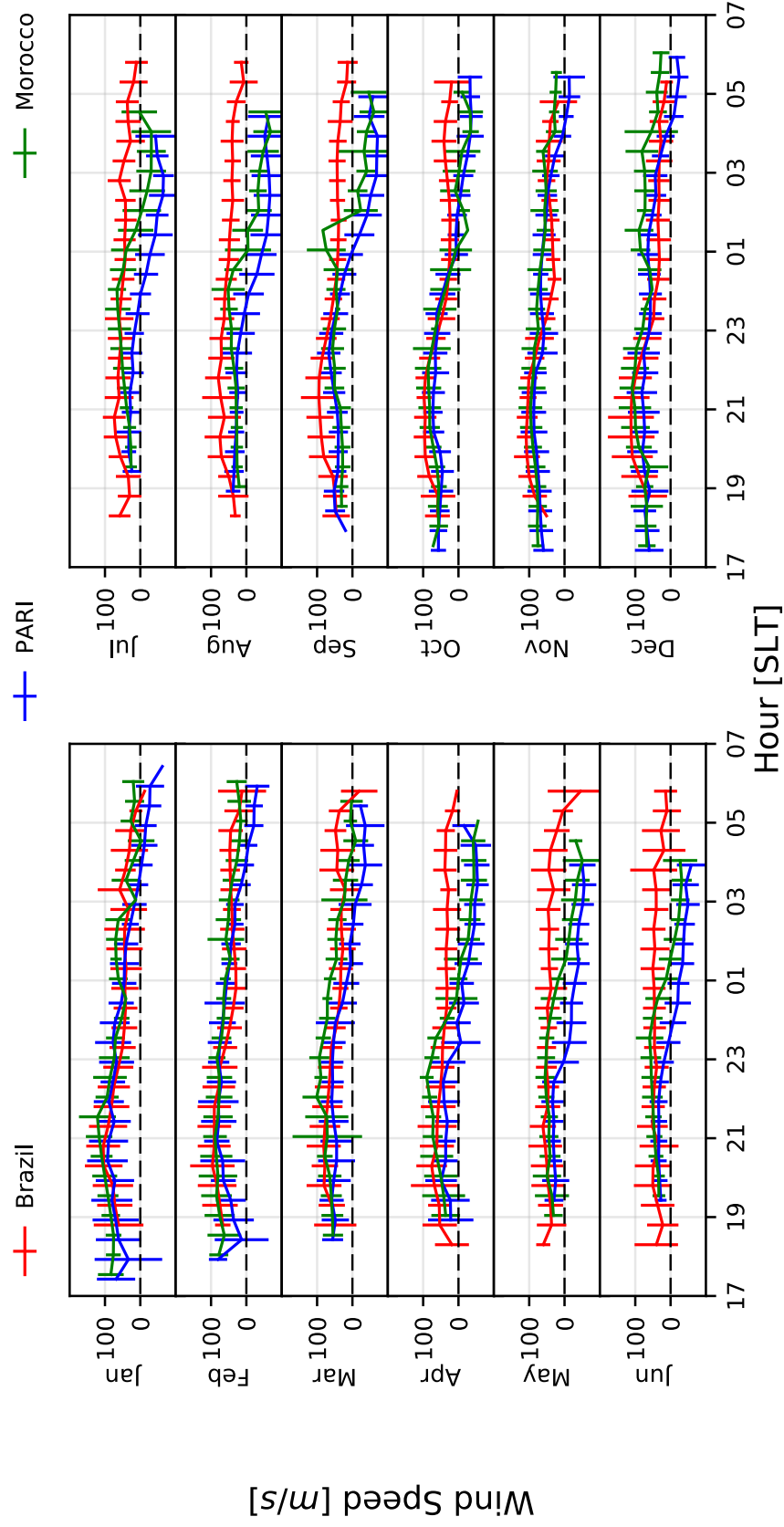


Figure 4.4: Climatologies of the thermospheric zonal winds during solar quiet times. Positive values are eastward.

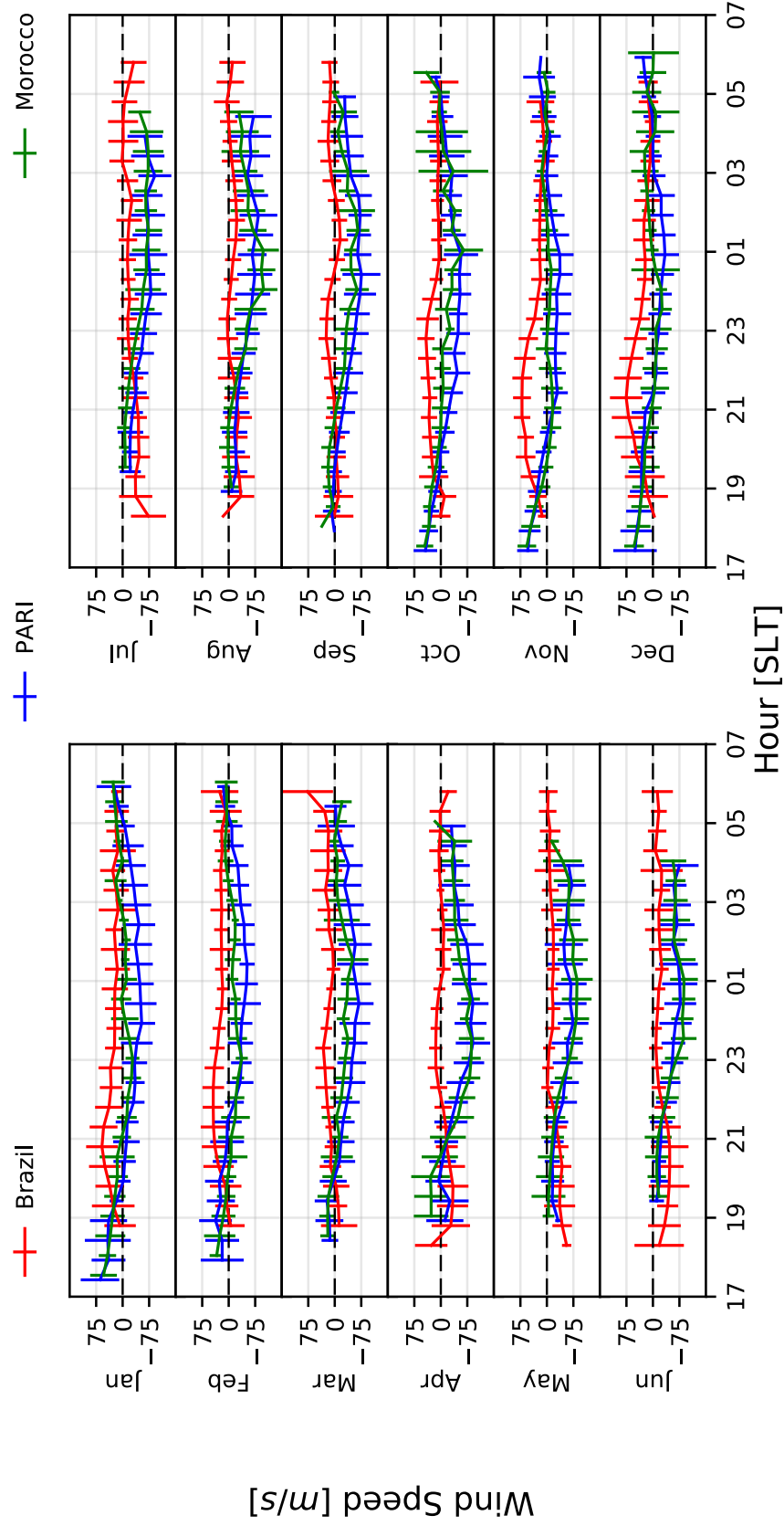


Figure 4.5: Climatologies of the thermospheric meridional winds during solar quiet times. Positive values are northward.

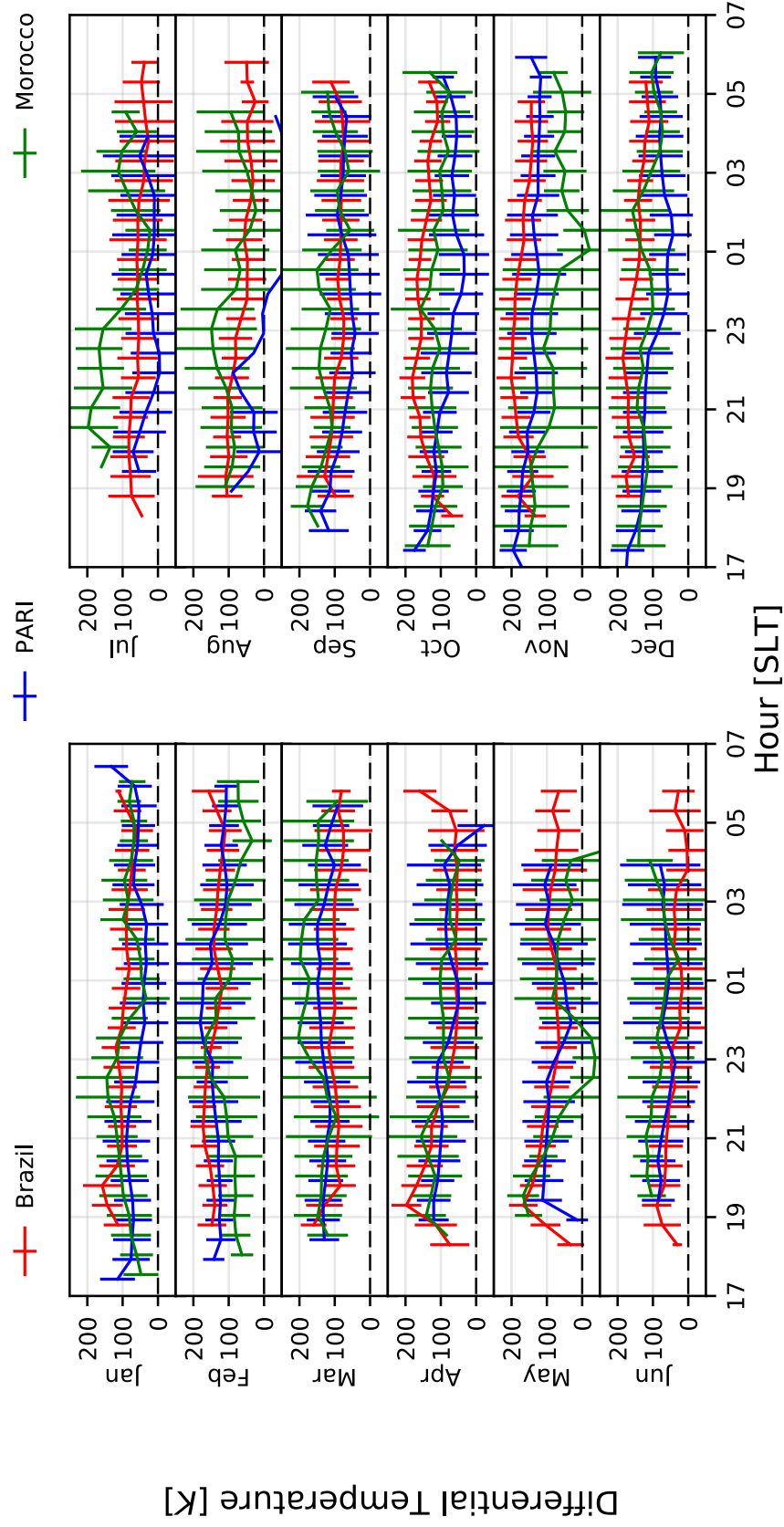


Figure 4.6: Climatologies of the thermospheric temperature difference between high and low solar flux times.

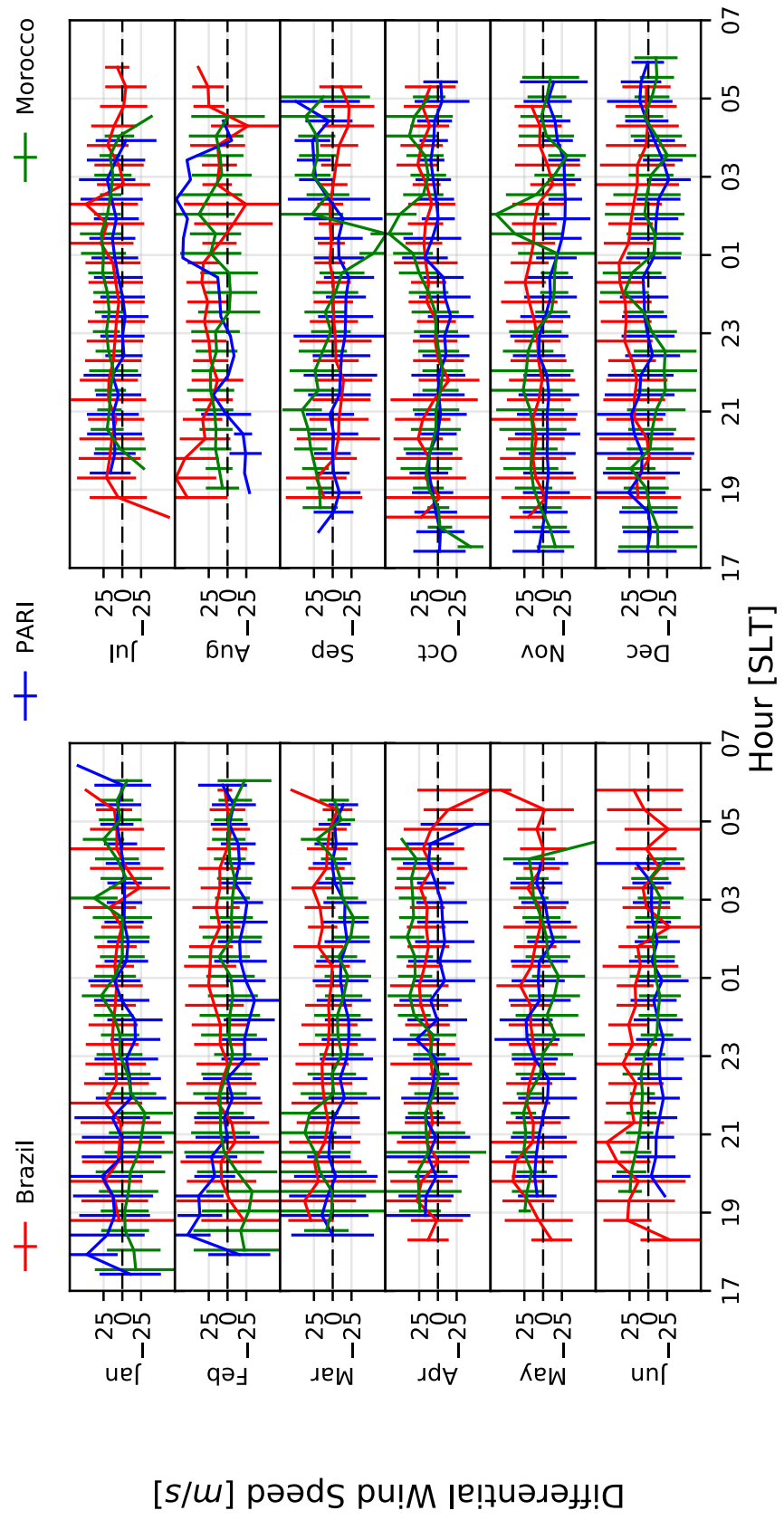


Figure 4.7: Climatologies of the thermospheric zonal wind difference between high and low solar flux times. Positive values are eastward.

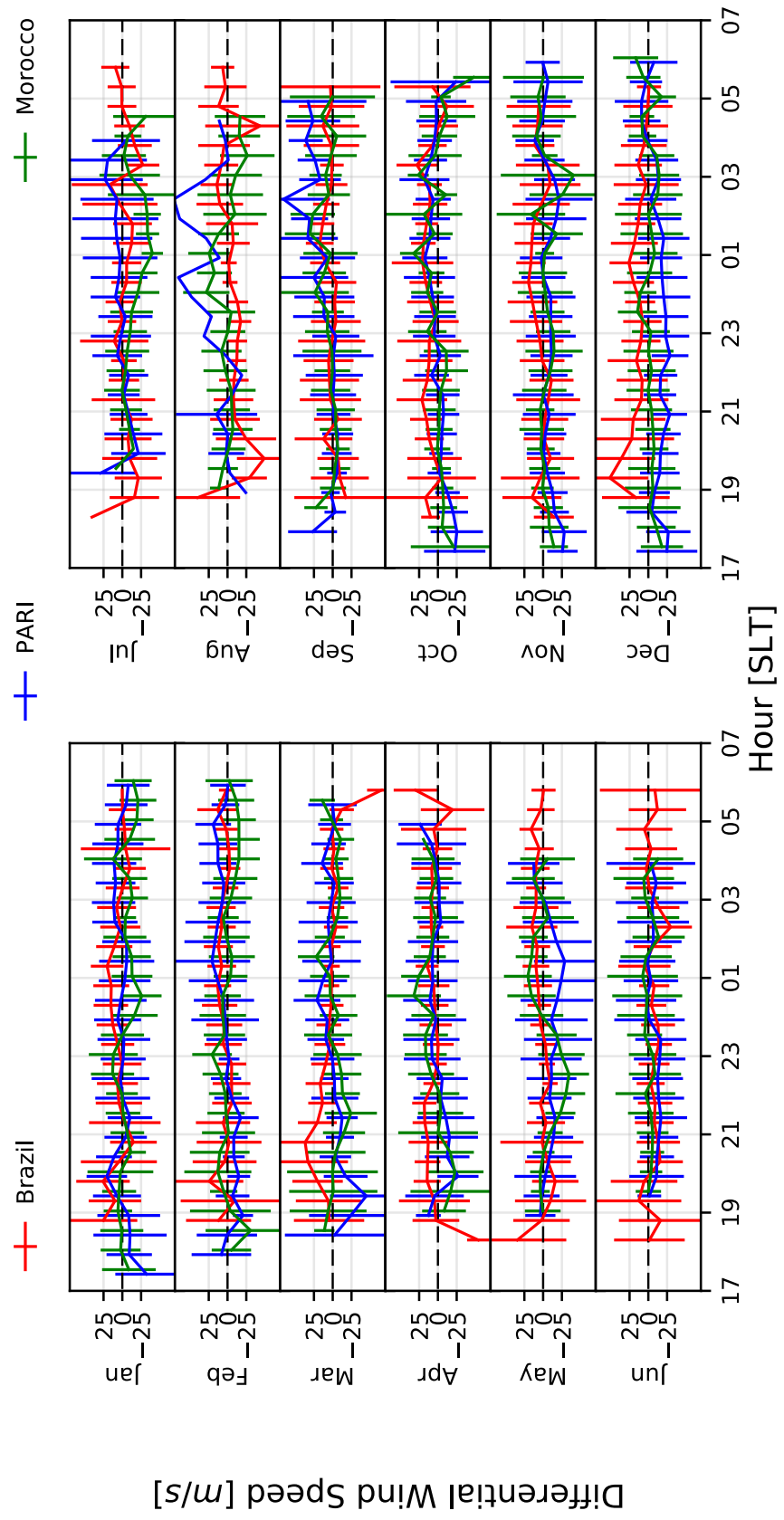


Figure 4.8: Climatologies of the thermospheric meridional wind difference between high and low solar flux times. Positive values are northward.

As discussed in Section 4.1.1, the solar fluxes, and therefore the differential solar fluxes, are not identical month-to-month. This must be taken into account to properly analyze changes caused by the solar input. Table 4.1 lists the average low solar flux (used in Figures 4.3, 4.4, and 4.5), the average high solar flux, and the difference between the two (used in Figures 4.6, 4.7, and 4.8). Since solar cycle changes will lead to changes in the temperatures and winds, we should expect to see larger effects when the solar flux difference is greater.

We seek to further confirm this theory by analyzing the correlation between temperature change and solar flux change. Figure 4.9 depicts all the differences in temperature from Figure 4.6 against the monthly differences in $\overline{F_{10.7}}$ from Table 4.1. An uncertainty-weighted, linear best fit has been applied to each location's data. Even though the local time variations are large, the general trend of increasing temperature with increasing solar flux is evident at all sites.

Finally, we share the latitude/longitude variations between the sites for three set months. Figure 4.10 presents quiet-time monthly averages comparing the neutral winds collected over Brazil (red), PARI (blue), and Morocco (green). Data are from the single months of January, April, and July of 2014 with zonal winds on the left half and meridional winds on the right. This figure presents not a month-by-month climatology sorted by $\overline{F_{10.7}}$, as in the previous figures, but a single monthly average. The latitudinal differences in the meridional winds are expected to be largest as the low-latitude region is primarily driven by solar forcing, while the mid-latitude locations are influenced by both forcing from the sun and polar cap heating. The two mid-latitude sites are expected to behave similarly because they are at similar geographic latitudes, although variations could be expected due to differences in geomagnetic latitude.

4.2.1 Climatology for Northeastern Brazil

We begin by discussing the observed quiet-time climatology of the thermospheric temperatures and winds over northeast Brazil. The low-latitude neutral temperatures, shown in red in Figure 4.3, are in good agreement with prior results from *Meriwether et al.* [2011]. Each month, the neutral tem-

Table 4.1: Monthly low, high, and differential solar flux values for each site. Each is a weighted average value using the total number of measurements.

Month	Location	Low $\overline{F_{10.7}}$ [10^{-22} Ws/m ²]	High $\overline{F_{10.7}}$ [10^{-22} Ws/m ²]	$\Delta \overline{F_{10.7}}$ [10^{-22} Ws/m ²]
Jan	Brazil	103.0	148.0	45.0
	PARI	112.5	140.3	27.8
	Morocco	102.4	145.2	42.8
Feb	Brazil	104.6	162.4	57.8
	PARI	108.6	152.3	43.7
	Morocco	111.6	154.7	43.1
Mar	Brazil	111.4	148.6	37.2
	PARI	107.1	145.2	38.1
	Morocco	100.0	146.4	46.5
Apr	Brazil	106.0	138.0	32.0
	PARI	107.4	138.6	31.2
	Morocco	103.4	139.3	35.9
May	Brazil	107.2	134.8	27.6
	PARI	107.4	135.4	28.0
	Morocco	108.1	136.7	28.5
Jun	Brazil	110.6	134.3	23.7
	PARI	111.4	135.7	24.3
	Morocco	105.5	136.3	30.8
Jul	Brazil	107.8	146.1	38.3
	PARI	110.6	146.7	36.2
	Morocco	105.3	145.9	40.6
Aug	Brazil	107.6	134.6	27.0
	PARI	108.3	127.6	19.3
	Morocco	104.7	135.7	31.0
Sep	Brazil	106.2	134.5	28.4
	PARI	100.6	137.8	37.1
	Morocco	95.7	145.8	50.1
Oct	Brazil	100.1	136.2	36.0
	PARI	102.6	146.1	43.5
	Morocco	101.9	153.6	51.7
Nov	Brazil	96.0	144.6	48.6
	PARI	94.3	145.4	51.1
	Morocco	103.4	147.8	44.5
Dec	Brazil	96.2	143.7	47.6
	PARI	97.0	144.4	47.3
	Morocco	99.2	154.0	54.8

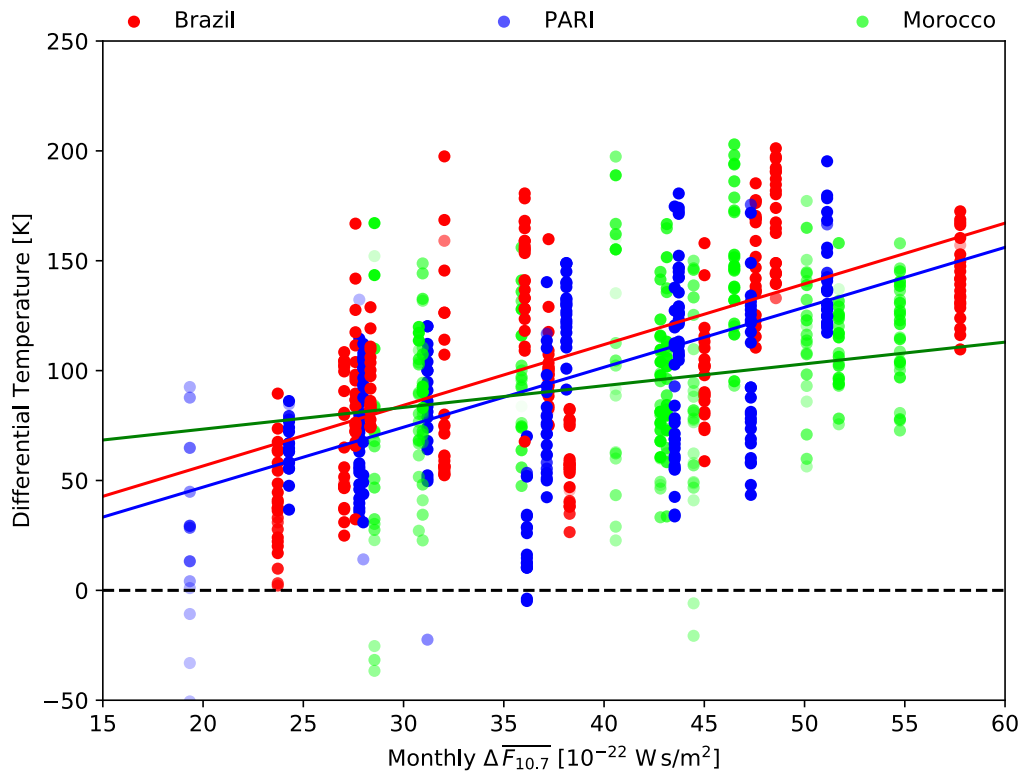


Figure 4.9: Scatter plot of differential temperature versus differential $\overline{F}_{10.7}$. The solid lines are linear weighted best fit curves for each site.

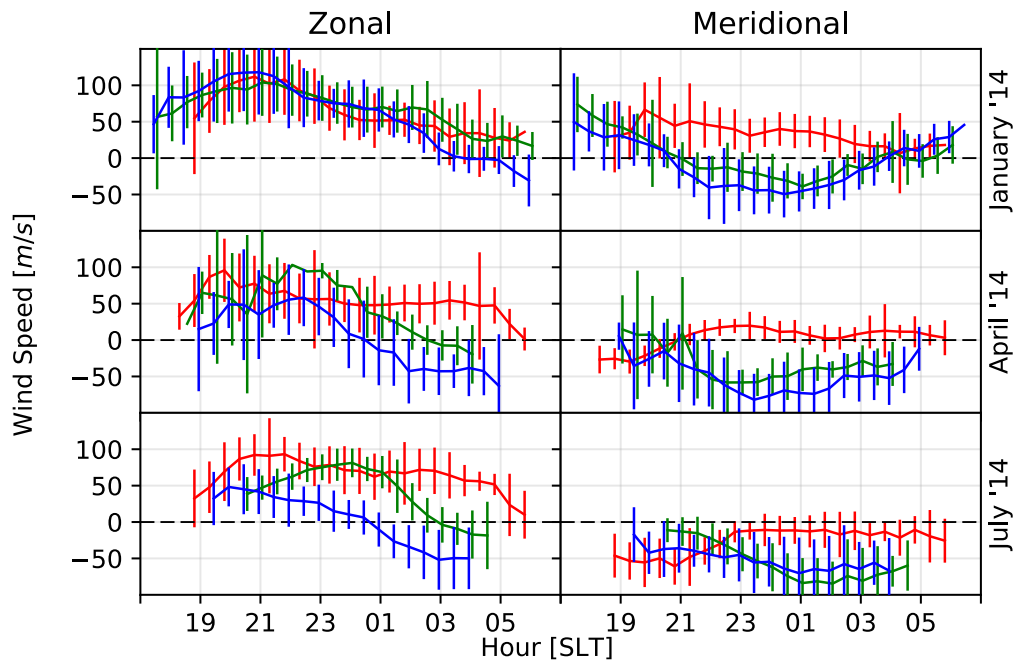


Figure 4.10: Monthly averages of the zonal and meridional wind over Brazil (red), PARI (blue), and Morocco (green) from three seasons: January, April, and July of 2014. The winds are plotted SLT. After *Fisher et al.* [2015].

perature is seen to gradually cool over the night. This is typically followed by an increase in the temperature around local midnight, a signature of the midnight temperature maximum [MTM; *Mayr et al.*, 1979]. The MTM is present most months (most easily noticeable in the equinox periods) and occurs regardless of solar flux conditions. However, the MTM is not a daily occurring phenomenon, and thus the feature tends to be washed out in the monthly averaging. Here, the variability ranges from 50 to 100 K, with no seasonal trend.

In the Brazilian zonal winds of Figure 4.4, we find the variation seen in this component to be typically 20 to 40 m/s. The nighttime zonal wind is always eastward, as expected, with a maximum value occurring one to two hours after sunset. The peak wind speed changes from 150 m/s in local summer to 75 m/s in local winter. The winds then decay to zero before sunrise. This occurs most rapidly in the summer months.

The Brazilian monthly averaged meridional winds in Figure 4.5 also show that the variability is equal to the zonal component (20 to 40 m/s). The nighttime meridional winds are also consistent with prior work [*Makela et al.*, 2013]. The low-latitude meridional wind follows the typical summer-to-winter hemispherical flow. This flow peaks around 21 SLT, with wind speeds higher in the summer months. During the equinox, the meridional winds show two equatorward maxima (at 23 SLT and 04 SLT) with a null near 01 SLT.

Moving to the differences seen due to solar flux, the Brazilian temperatures show an obvious solar flux dependence. The temperature increase ranges from 25 to 200 K. Figure 4.9 fits the relationship between solar flux and change in temperature, showing a 50 K increase per $\overline{F_{10.7}}$ increase of 20 W_s/m^2 . Neither the zonal nor meridional winds show a clear solar flux dependence, but we do see some local time effects. For example, there is an equatorward enhancement of ~ 40 m/s in December and March after sunset and a 20 to 40 m/s poleward enhancement in July and August after sunset. A 20 to 25 m/s enhancement in the equatorward direction is also seen around 01 SLT in the local summer. Unlike the meridional winds, the zonal winds appear to consistently be slightly faster in higher solar flux. We see a roughly 15 m/s increase across most months and local times.

4.2.2 Climatology for PARI

Next, we discuss the quiet-time climatologies above PARI. Starting with the neutral temperatures in blue from Figure 4.3, the monthly averaged neutral temperatures show the expected cooling until local midnight, at which point the temperature slowly starts increasing again. The mean temperature trend even shows an MTM peak around 01 SLT in May. The variability of temperatures is typically small (~ 50 K) except around midnight when a few months (April to August) show standard deviations of 100 K.

The mid-latitude zonal wind climatology over PARI are depicted in Figure 4.4. The zonal winds are eastward at the beginning of the night until a reversal occurs between midnight and 03 SLT. The fastest eastward zonal winds are seen a few hours before midnight, but the magnitude and timing vary seasonally. Amplitudes of 100 m/s are seen in the local winter while only 30 m/s winds are seen in the local summer. The westward zonal wind peak is also seasonally varying, from 0 m/s in the local winter to ~ 40 m/s in the local summer. Similar to the data collected in Brazil, the day-to-day variability seen over PARI is 20 to 40 m/s.

Figure 4.5 shows the monthly averaged meridional wind climatology for PARI. Note the presence of a poleward-to-equatorward reversal near 20 SLT. Equatorward winds are strongest at midnight, reaching 75 m/s. Around 04 SLT, a second reversal occurs, resulting in weak poleward winds. The variability observed in the meridional component is equivalent to that of the zonal component: 20 to 40 m/s.

The direct solar dependence is seen in the differential neutral temperatures, with temperatures 10 to 200 K hotter during high solar flux nights. The differential temperature/solar flux fit for PARI matches that of Brazil: a 50 K increase per $\overline{F_{10.7}}$ increase of 20 Ws/m². There is another similarity to Brazilian data: no clear solar dependence in the neutral winds is apparent. However, features are seen in the local winter months. The post-sunset meridional winds show a 25 m/s equatorward enhancement and the post-sunset zonal winds show a ~ 20 m/s eastward enhancement. Also, the zonal winds after midnight are on average 10 m/s more westward during the high solar flux conditions in local winter.

We now briefly compare the latitudinal differences seen in Figure 4.10 between low-latitude Brazil and mid-latitude PARI. The January zonal winds

match precisely; however, in April and July the zonal winds in PARI reverse while the zonal winds in Brazil remain eastward all night. Furthermore, the differences in wind speed are largest in July, with up to 125 m/s differences. As expected the meridional winds are very different. The low-latitude measurements show the clear summer-to-winter hemispherical flow that eventually decays to zero while the mid-latitude measurements show equatorward winds. Only the January post-sunset and pre-sunrise hours have a poleward component.

4.2.3 Climatology for Morocco

Finally, we describe the quiet-time climatologies for the thermospheric neutral winds and temperatures over Oukaïmeden Observatory. Starting with the monthly averaged neutral temperatures in green from Figure 4.3, we see the expected decrease in temperature until local midnight, at which point the temperature typically starts slowly increasing. The temperature variability is also small over Morocco, with a standard deviation of ~ 50 K. However, during a few months around midnight, the standard deviations increase to around 100 K.

Figure 4.4 shows the zonal wind climatology. First, the wind is eastward until a reduction or reversal occurs after midnight. The timing of this reversal is seasonal, seen almost at sunrise in the local winter and at 02 SLT in the local summer. There is also a seasonal dependence in the peak eastward winds. The maximum is stronger and occurs earlier in the local winter (over 100 m/s at 22 SLT), and is weaker and later in the local summer (75 m/s at 00 SLT). The variations seen over Morocco are similar to those measured in PARI, with standard deviations between 20 and 40 m/s.

Figure 4.5 shows the meridional winds collected from the west African sector over Morocco. The wind pattern shows a poleward-to-equatorward reversal around 21 SLT, equatorward winds at local midnight, and an equatorward-to-poleward reversal after 03 SLT. Note that the meridional wind reduction is incomplete in the local summer, only reaching ~ 50 m/s. The equatorward winds are also stronger in summer than in winter.

The Moroccan linear fit in Figure 4.9 shows the same positive trend between neutral temperature and solar flux but has a smaller response than

Brazil and PARI, possibly due to higher variability seen in this region. An average of 100 K increase is seen at all local times. Like at the other sites, Moroccan data does not contain a strong correlation between the neutral winds and solar flux, but small local time features are apparent. A small, 15 m/s equatorward enhancement is present in the local winter. During a few equinox months, a 25 m/s poleward enhancement is present after midnight. No discernible zonal feature is detected.

Last, we compare and contrast the three monthly climatologies of the mid-latitude sites, PARI and Oukaïmeden. In general, the meridional components of the neutral winds at these two sites are comparable, especially in magnitude. The data collected during January 2014 indicate that both sites also show a transition in the meridional flow from poleward to equatorward, occurring between 20 and 21 SLT. Then, another transition back to poleward exists between 03 and 05 SLT. The meridional winds over both sites are increased during April of 2014. In July 2014, the meridional wind over both sites is southward, with the maximum equatorward flow reached at around 01 SLT.

The coincident mid-latitude zonal winds show more disagreement. In each month, the zonal winds turn westward approximately two hours earlier over PARI than over Morocco. The eastward winds before this reversal are also significantly stronger over Morocco than they are over PARI in April and July of 2014. For example, a peak in the eastward wind over Morocco in July of ~ 75 m/s is seen around local midnight, compared to a steadily decreasing wind over PARI, starting at ~ 12 m/s. In January 2014, Morocco and PARI both show similar peak eastward flow of ~ 100 m/s, both around 21 SLT. Section 4.3.3 contains a more comprehensive analysis of the longitudinal variability.

4.3 Discussion of Climatological Variations

4.3.1 Seasonal Neutral Variations

The neutral temperatures at all sites follow a similar pattern: temperatures start around 1000 K and gradually cool down until dawn. However, around midnight, the thermospheric temperatures can increase due to the MTM. The

signature is clearly present in the Brazilian data for most months. It may also be present in the two mid-latitude sites. The increased variation seen around midnight in some months could be indicative of an MTM occurring occasionally. It is known that the MTM does not occur daily, and when it does, the magnitude of the effect is varied [*Spencer et al.*, 1979]. The MTM feature is seen to be most common over PARI in the summer, with observations still frequent in spring and fall [*Mesquita et al.*, Submitted]. These months match when higher day-to-day variability is seen over PARI.

The quiet-time, low solar flux neutral wind observations also agree with prior work. The zonal winds are typically eastward, slowly decaying over the night and, at times, turning westward before dawn. The meridional winds in the low-latitude sites show the well understood summer-to-winter hemispherical flow, while the measurements in the mid-latitudes show more forcing from the polar regions, with equatorward flow peaking at midnight most months. This dataset is important because it creates a long-term baseline for the neutral winds, useful for improving climatological models. One of the most important insights from these climatologies is the day-to-day variability. These variations are rarely captured in models and further studies are required to fully understand what drives the daily fluctuations.

4.3.2 Solar-Driven Neutral Variations

Despite the limited range of $\overline{F_{10.7}}$ values covered by these datasets, the thermospheric temperatures do show great distinction between our designated high and low solar flux conditions. Figure 4.6 shows a very clear difference; on average, there is a 50 to 150 K increase seen over all sites. This is confirmed by Figure 4.9, which shows a direct correlation between change in temperature and change in solar flux. The direct correlation is the expected neutral temperature dependence on solar cycle [*Hernandez*, 1982; *Makela et al.*, 2013].

Thermospheric winds, on the other hand, do not seem to respond as drastically as the temperatures to solar flux variations. The seasonal differences, noted in Section 4.2, appear to dominate the variation. However, slight local-time, solar-cycle dependences are observed. The feature common to all three sites is an equatorward enhancement of the meridional winds in

the local winter months after sunset. Arguably, it would be easiest to observe solar flux changes from November to February as these months see the largest differential $\overline{F_{10.7}}$ (from Table 4.1). Additionally, post-sunset wind enhancements are seen in July and August in Brazil’s meridional winds and in the post-sunset zonal winds of Brazil and PARI. Any early evening effect is likely due to the ion drag, which is expected to have a strong solar cycle dependence. Near solar minimum, the plasma does not reach higher altitudes because the pre-reversal enhancement is generally weak [Fejer *et al.*, 1979; Fejer, 1981]. Consequently, the eastward pressure gradient is balanced partly by the ion drag caused by the collisions of the neutral gas with the F-region plasma. Near solar-maximum, the removal of the F-region plasma to higher altitudes by the pre-reversal enhancement phenomenon near twilight allows the pressure-gradient forcing to become fully dominant, accounting for the increased early evening wind.

Another local-time solar-cycle dependence is seen after midnight at all three sites. Zonal and meridional wind enhancements are observed after midnight November through February (the months with large $\Delta \overline{F_{10.7}}$) in Brazil. On the other hand, PARI sees a zonal wind reduction from November through February, while Morocco observes a meridional reduction during the equinoxes. These could be related to MTM signatures as they potentially align with decreases in temperature at these times. Unfortunately, the variability of the temperatures is very large, around 100 K, making such variations hard to see on top of the ~ 100 K temperature increase associated with increased solar flux. Faivre *et al.* [2006] demonstrated an inverse relationship between MTM amplitude and solar flux. Therefore, it is plausible that the wind changes observed post-midnight are related to weaker MTM signatures.

A previous climatological study of the thermospheric neutral winds by Emmert *et al.* [2006] presented a consistent relationship between increasing solar flux and increasing magnitudes of the zonal and meridional winds observed by a low-latitude FPI located at Arequipa, Peru (geographic: 16.5°S, 71.5°W geomagnetic: 3.5°S). The range of solar flux values covered in their study (60-220 SFU) is broader than here (70-157 SFU), but the study also found a stronger dependence in the zonal component of the thermospheric neutral wind compared to our observations. However, their study at low-latitudes did not cover the local summer period at Arequipa, due to poor observ-

ing conditions typical of that site during those months. Thus, the results presented here indicating a slight solar cycle dependence of the meridional and zonal winds over Brazil during the local summer months augment the conclusions reached by *Emmert et al.* [2006].

At mid-latitudes, the meridional wind results are less coherent than in Brazil. No correlation exists between the meridional winds and differential solar flux, nor are there repeating local-time variations. On the other hand, results from PARI indicate a slight decrease in the magnitude of the thermospheric zonal winds with increasing solar flux. This is most prevalent during local winter (November and February), when the zonal winds are reduced by ~ 25 m/s after midnight. A reduction is seen in June, but during the pre-midnight hours. The results from Morocco show that the winds are reduced during local winter, too, but the zonal winds in December and January decrease ~ 25 m/s during the pre-midnight hours. *Fejer et al.* [2002] and *Emmert et al.* [2003] presented results collected by a mid-latitude FPI located at the Millstone Hill Observatory (geographic: 42.6°N , 71.5°W geomagnetic: 53.1°N) that showed a similar relationship between the mid-latitude flow and solar flux. This result was explained by considering that the increased ion drag at higher solar flux values dominated the pressure gradient forcing. Notably, *Emmert et al.* [2003] found that this relationship was strongest in local winter.

Consistent with the results of *Emmert et al.* [2003], we see the largest magnitude in the post-sunset zonal winds during October and November, and a small solar cycle dependence in this component during these months for PARI observations. However, unlike *Fejer et al.* [2002] and *Emmert et al.* [2003], we see a direct solar flux dependence in the zonal winds for parts of the night April through September; that is, an increase in the zonal wind with an increase in solar flux. The Oukaïmeden observations also indicate a 50 m/s direct solar flux dependence at 02 SLT in October and November, but it is worth noting that variations over 30 m/s exist during those times.

Regardless of latitude and longitude, the solar cycle variations seen in the horizontal winds in our dataset are very minimal. The seasonally driven pressure gradient is the driving force behind the quiet-time horizontal winds. It is worth noting that the day-to-day variability is usually on the same order of magnitude as these solar cycle variations. Therefore, for deep solar minimum intervals, it seems reasonable that one could neglect to account for solar

flux in the neutral winds, especially when averaging large datasets together. This is very useful for comparing our long-term dataset with HWM14 as the recent iteration does not include solar flux as an input. A similar approach is not applicable for thermospheric temperatures, which were noted to be more sensitive to solar input.

4.3.3 Geographic Variations of Neutral Winds

The meridional winds are markedly different between the low-latitude (Brazil) and mid-latitude (PARI and MOR) sites. The low-latitude measurements show the clear summer-to-winter hemispherical flow that eventually decays to zero while the mid-latitudes show equatorward winds all year, suggesting nighttime forcing from the poles. On the other hand, the zonal winds are very similar for all three locations in January; they are all eastward and slowly decaying before the dawn reversal. However, the April and July zonal winds show that magnitudes do vary by latitude and that timing differences can exist. We see the low-latitude sites typically have the strongest zonal winds, followed by Morocco and PARI. We also notice that the westward reversal happens three hours after Morocco's reversal, which is two hours after PARI's reversal. While Brazil's differences are explained by the sites observing in a different latitude regime, the differences between the mid-latitude sites are intriguing. Since the latitudinal differences were expected, we turn our focus to the longitudinal variations in the two mid-latitude sites.

A study of the difference between two longitudinally separated mid-latitude FPIs was conducted by *Wu et al.* [2014]. In their study, data from three FPIs, two in China and one in Boulder, Colorado, were studied to investigate differences in the mid-latitude neutral wind patterns on two separate nights in October 2012. They concluded that the meridional winds were largely the same in the two separate longitude sectors, with the primary difference being the timing of the equatorward wind maximum, which was reached earlier for the Chinese sites than for the measurements over Boulder. More significant differences were observed between the zonal winds, which showed larger diurnal variation (maximum minus minimum wind speed) and an earlier turning from eastward to westward for the Boulder site. *Wu et al.* [2014] attributed these variations to the difference in the geomagnetic latitude of the two sites,

with Boulder being at 49°N and the two Chinese FPIs being at 33°N and 34°N.

Although the geographic latitudes of PARI and MOR are further equatorward than the sites used in the *Wu et al.* [2014] study, their geomagnetic latitudes span a similar range (21.6°N for MOR and 46.2°N for PARI). Ignoring the slight effects of the solar cycle differences in October 2012 (the period of the *Wu et al.* [2014] study) and when we have coincident measurements from PARI and MOR, we see several similarities when comparing the mid-latitude wind patterns. For example, the zonal winds seen in our April 2014 (equinox) averages also show an earlier westward turning at PARI compared to MOR (00 SLT compared to 02 SLT, respectively), similar to the earlier westward turning at Boulder in *Wu et al.* [2014]. However, one difference between the climatological results presented here and those for the two nights presented in *Wu et al.* [2014] is that the latter study indicated larger diurnal variability in the zonal winds for the site at a higher geomagnetic latitude, which they attributed to the effects of auroral heating. In our results, the diurnal variations for PARI and MOR are approximately equal, about 50 m/s on average; however, the MOR winds are shifted eastward from those observed over PARI. Whether this is an effect of differences between climatological comparisons (our results) and case studies of individual nights (*Wu et al.* [2014]), or a longitudinal effect not seen in the *Wu et al.* [2014] study, is unclear at this time.

4.4 Summary

We summarize the key points learned from the long-term studies of our FPI data:

- We have captured the typical quiet-time conditions of the thermospheric winds and temperatures from our long-term ground-based FPI datasets in Brazil, the United States, and Morocco. We are able to monitor both daily and seasonal changes over the night.
- Increased solar flux increases the thermospheric temperatures measured by the redline emission. Even in the limited range of $F_{10.7}$ observed, temperatures increased 50 to 150 K on average over all months.

- Increased solar flux has a negligible effect on the horizontal neutral winds, at least for the limited range of $F_{10.7}$ experienced during solar cycle 24. Note that this was a less active solar cycle than previous ones. However, local-time wind enhancements are seen post-sunset (relating to changes in ion drag with changing solar flux) and after midnight (potentially relating to reduced MTM signatures).
- Latitudinal variations are clearly seen in the meridional wind flow, as the low-latitude is driven by summer-to-winter hemispherical flow and the mid-latitude is additionally driven by the polar region. The zonal winds were in good agreement in January, but magnitude differences were seen in April and July, with the low-latitude site having larger amplitudes.
- While the mid-latitude meridional winds are in good agreement, the zonal winds are not in agreement. Specifically, the timing of the east-west reversal over PARI occurs two hours before the reversal over Morocco. These differences are likely due to the differences in geomagnetic latitude as prior studies have shown similar results with higher magnetic-latitude sites having an earlier reversal. The timing of the eastward peak also varies between PARI and Morocco, although it is not clear if this is just a longitudinal difference.

CHAPTER 5

VALIDATION OF EMPIRICAL MODELS

This chapter discusses the use of our long-term Fabry-Perot measurements to improve thermospheric models, specifically regarding the horizontal neutral winds. As the neutral winds are currently an under-sampled parameter of the upper atmosphere, all measurements made are vital to validating physics-based models and improving empirical-based models. These models are widely used in place of data by the wider community since achieving global coverage of the neutral parameters at all local times is currently impossible. The horizontal wind model (HWM) is perhaps the most widely used neutral wind model and our datasets have been essential to improving that product. However, the temperature data can also be used to aid models such as the mass spectrometer and incoherent scatter empirical model [MSIS; *Hedin et al.*, 1977] and the whole atmosphere model [WAM; *Akmaev*, 2011].

5.1 Using Data to Update HWM

The popular horizontal wind model was created in 1988 using only satellite data from Dynamic Explorer 2 and Atmospheric Explorer [*Hedin et al.*, 1988]. Over the years it was updated to include increasingly diverse measurements, and expanded to provide winds from the surface to the thermosphere [*Hedin et al.*, 1991, 1996]. One of the important additions was ground-based neutral wind measurements. These fixed sites provided a wind survey of the same geographic location each night. Paired with satellites, which provided better spatial coverage but poorer local time resolution, in-situ data from rocket soundings, and spherical harmonic functions to fill in the gaps, a global model of neutral winds was created. Given a latitude, longitude, altitude, date, and time, HWM returns the horizontal wind vector. A new version was created in 2007, which separated the baseline winds from the disturbance winds along

with adding more datasets to fill in the sparse coverage, both geospatially and in local time [Drob *et al.*, 2008; Emmert *et al.*, 2008].

Having one of the longest, nearly continuous datasets of thermospheric neutrals in South America from the Fabry-Perots installed in Cajazeiras and Cariri, Brazil, we were able to independently validate HWM07's improvements over HWM93. No data from the Brazilian sector were used to create HWM07 or HWM93, outside of satellite passes over the area. Since the horizontal wind model does not contain the day-to-day fluctuations of real winds, it was expected that the model could only capture the general seasonal and local time trends. Figure 5.1 presents the night time zonal winds measured from the Brazilian FPI sites, modeled from HWM93, and modeled from HWM07 between August 2009 and December 2013. The HWM winds are taken from the geographic midpoint between the two Brazilian FPIs at an altitude of 250 km, the assumed emission-peak altitude at night. Easily seen are the local time dependences of the measured neutral winds: they start off strong and eastward after sunset and decay to nearly zero by sunrise. The seasonal dependences are also evident from the figure: the eastward winds are strongest in the local summer (December through February) and weakest in local winter (June through August). In general, HWM93 captures both the local time and seasonal dependencies. We see the strong post-sunset winds (with the local summer having larger amplitude winds than in local winter) that decay to zero at sunrise. It is also evident that a slight solar flux dependence exists, causing wind speeds to be more than 10 m/s greater in 2013 compared to 2010 in solar minimum. The amplitudes between 18 and 22 LT are on average 75 m/s greater in the model than in the measurements, but the amplitudes of the winds from 00 to 05 LT are on average within ± 25 m/s.

What is very interesting is how different the HWM07 zonal winds are. The seasonal dependence is present in the early night, but non-existent after midnight when an apparent semiannual variation dominates the seasonal pattern. The most obvious difference between the FPI measurements and HWM07 is the local time trend; there is no wind speed decay from dusk to dawn to match the data. The amplitudes are greatly underestimated by ~ 60 m/s in the model between 18 and 22 LT, and overestimated by ~ 40 m/s between 00 and 05 LT. Finally, no clear solar flux dependence can be seen.

We now turn to the meridional winds to see if similar shortcomings in

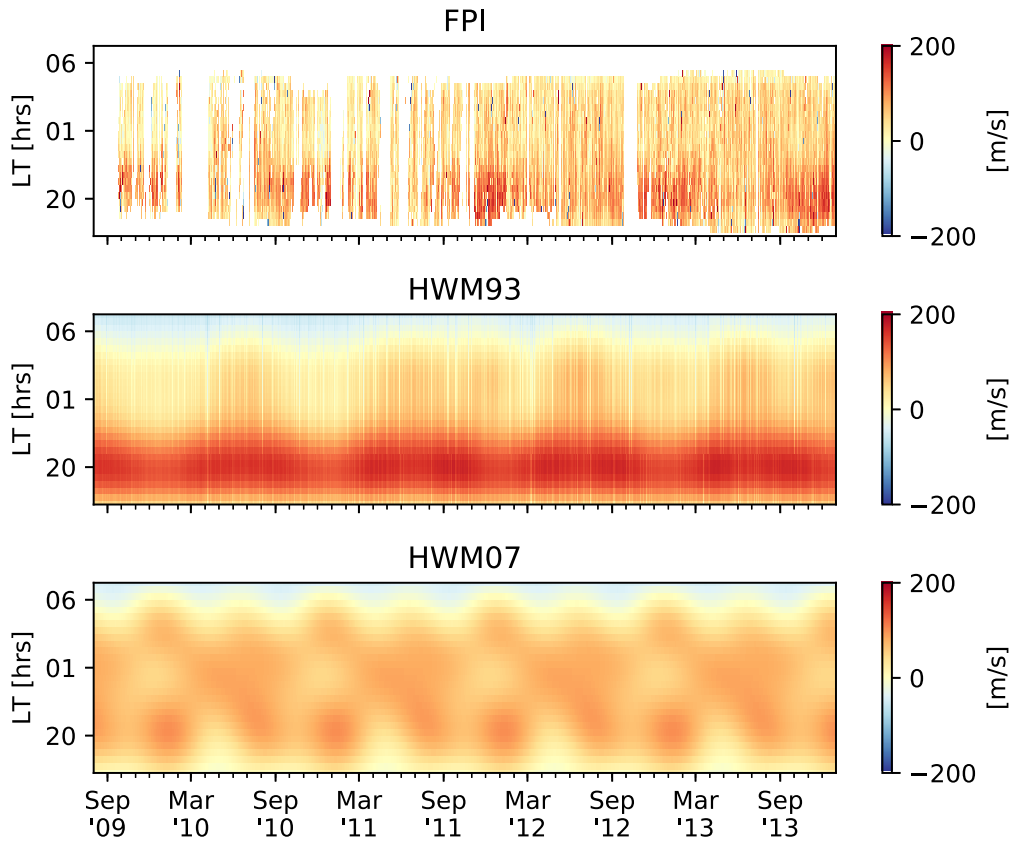


Figure 5.1: Comparing the FPI measured zonal winds over northeast Brazil to HWM93 and HWM07. Positive values are eastward. Model winds are from an assumed 250 km emission altitude.

HWM07 are seen over the Brazilian sector. The FPI measurements, HWM93 estimates, and HWM07 estimates for the meridional winds are presented in Figure 5.2. Again, the HWM data is from the midpoint between the two sites at 250 km. The obvious repeating pattern in the FPI measured meridional winds is the seasonal dependence. In the local summer the winds are equatorward and in the local winter the winds are poleward, consistent with the solar-driven cross-hemispherical flow. Winds are strongest just after sunset in the local summer and slowly decay to zero. The local winter winds start strong, decay to zero around midnight and then increase again (remaining poleward). HWM93 captures the seasonality, with equatorward winds in winter and poleward winds in summer. Even the decay to zero at midnight is captured by the model. The amplitudes seen in local winter and local summer do match well with measurements as they are typically within ± 20 m/s. Furthermore, only a very slight solar flux dependence can be drawn from the model.

HWM07 once again looks different than the measurements and HWM93, but does not differ as drastically as in the zonal winds. In the local summer, the winds are equatorward but underestimate the wind speed by 50 m/s. In local winter, there is a small time frame of poleward winds, which underestimates the amplitudes by 30 m/s. The best-fit waveform to the model at midnight seems to be a semiannual variation instead of the annual one seen in the data. What is also problematic here is the time shift that causes the maximum equatorward motion to occur earlier than in the data. Again no solar flux variation is present in HWM07.

Neither the zonal nor the meridional wind output of HWM07 agreed well with the measured results over northeast Brazil. The clear departure from the measured local time and seasonal dependences (and from HWM93) indicated that something in HWM07 was not correct. The appearance in both the zonal and meridional winds of a semiannual variation that was stronger than the annual variation, indicated that the weighting on the harmonics was incorrect. These results were concerning considering that HWM07 was the standard neutral wind model used by the upper atmospheric community. Studies using HWM as an input to their analysis could draw incorrect conclusions based on the model version used. If HWM07 was this far off in a location where little data was ingested, then other under-sampled regions were probably also unreliable.

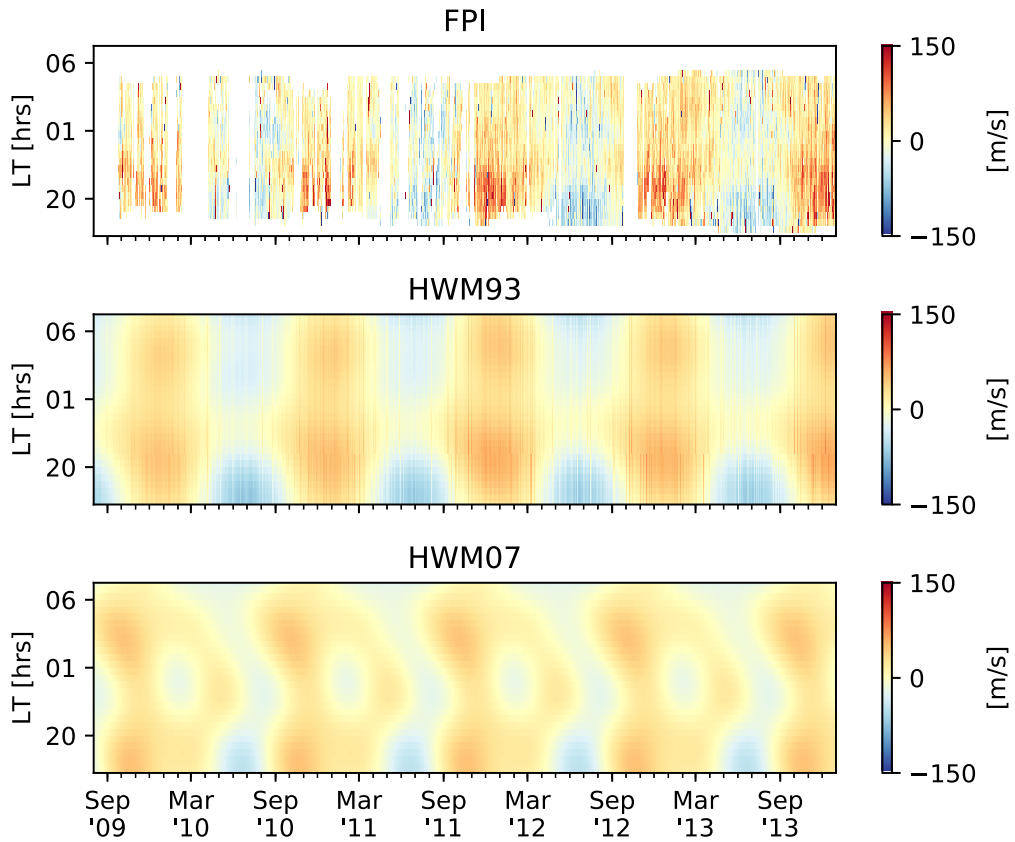


Figure 5.2: Comparing the FPI measured meridional winds over northeast Brazil to HWM93 and HWM07. Positive values are northward. Model winds are from an assumed 250 km emission altitude

To help correct this issue, three years of quiet-time horizontal wind data from Cajazeiras and Cariri were ingested into the next iteration of HWM. Over 37,000 data points from our dataset were used along with over 12,000 measurements from the FPI in PARI. These measurements were included with other FPIs from around the globe and new satellite data to help further fill in the gaps. The wind fits were also re-parameterized, creating the most recent iteration: HWM14 [Drob *et al.*, 2015].

The update noticeably fixed the discrepancies over northeast Brazil, as seen in Figures 5.3 and 5.4. The zonal winds of HWM14 show a local time variation consistent with the measurements of strong eastward winds that decay around 05 LT. The seasonal patterns are also improved with stronger winds in local summer. A semiannual harmonic seems present from 00 to 03 LT, but it is small and consistent with our dataset. Even the magnitudes of the zonal estimates are improved as agreements are within ± 25 m/s for all local times and seasons. The meridional winds of HWM14 show the improved seasonal variation, too, with equatorward winds in the summer and poleward winds in the winter. The agreements are within ± 25 m/s here as well, regardless of local time and season. The magnitude of the winds appears much improved over HWM93 as well, especially in the zonal winds. However, subtle changes in the wind pattern of HWM14 from HWM93 which cannot be verified in such a qualitative manner are seen in both wind components. Section 5.3 delves into a more advanced analysis for verifying HWM winds. Regardless, the simple comparison here shows that HWM14 is a reliable model over the Brazilian sector. This is perhaps unsurprising, as our data was used to improve the model fittings.

5.2 Comment on Measurement/Model Wind Comparisons

One uncertainty in interpreting Fabry-Perot measurements is that the emission altitude is unknown. FPI measurements are obtained by integrating all the light along a line-of-sight that passes through the narrowband filter, meaning the measurements are taken from a slice through the emitting layer. We have no corresponding measurements of the emitting layer height or width, but desire to assign a location to our wind and temperature es-

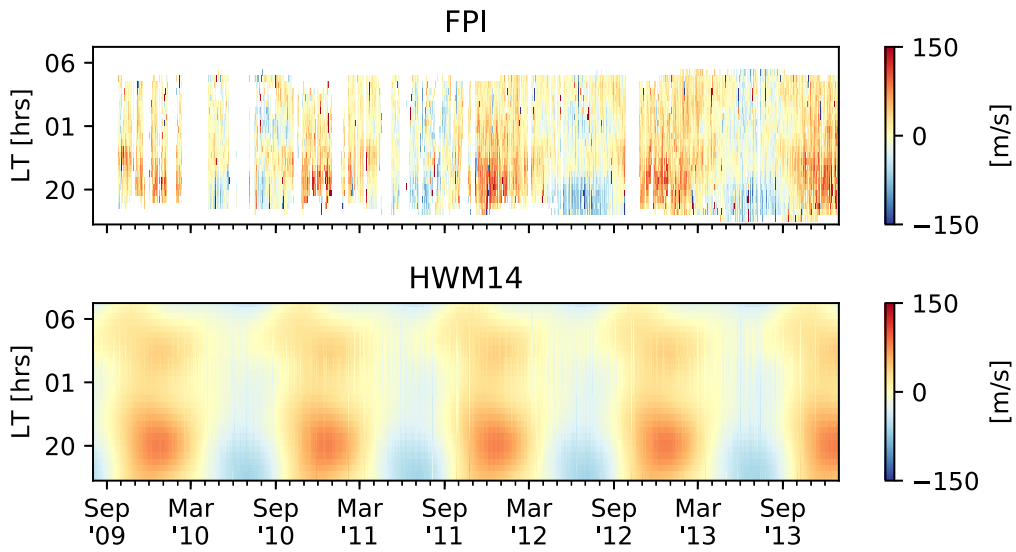


Figure 5.3: Comparing the FPI measured zonal winds over northeast Brazil to HWM14. HWM14 data from assumed 250 km emission altitude.

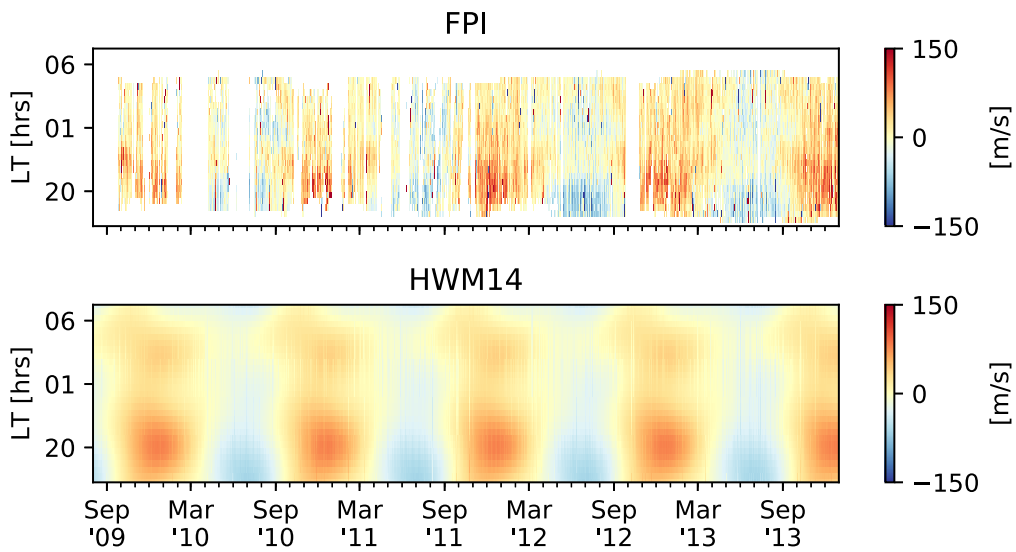


Figure 5.4: Comparing the FPI measured meridional winds over northeast Brazil to HWM14. HWM14 data from assumed 250 km emission altitude.

timates. Since most of the signal measured comes from the peak altitude where the emission is brightest, we attribute the observation to this peak location, commonly assumed to be 250 km. Another way of looking at this assumption is that the entire emitting region is collapsed to a thin layer at the peak height.

Recently, *Chartier et al.* [2015] performed a study that simulated the thermospheric observations of an FPI using several different models. For simulations of the low-latitude thermosphere, they concluded that incorrectly assigning the altitude of the emission layer could lead to erroneous data-model comparisons and that the largest errors were introduced when the emitting layer was lower than 250 km, due to the larger altitudinal gradients in the winds at low altitudes.

To investigate this potential effect on the comparison between observations and models, we simulate the altitudinal profiles of the nighttime 630.0-nm emission over our instruments for a full year. The standard climatological models for ion parameters [IRI; *Bilitza and Reinisch, 2008*] and neutral parameters [MSIS; *Picone et al., 2002*] are used to provide estimates of the atmospheric constituents required to calculate the redline volume emission rate specified in *Link and Cogger* [1988]. The peak altitude of the emitting layer is then found as a function of time of day and day of year. We show the deviations from the 250-km assumption during 2015 for Cariri, Brazil and Oukaïmeden, Morocco, in Figures 5.5 and 5.6, respectively. It becomes immediately apparent that the assumption of a static 250-km emission layer is not appropriate for almost any specific time. In the low-latitude site, we find that in the local summer, the altitude is 10 to 25 km higher than the standard assumption, but in the local winter, the peak altitude is lower by 35 km. The variation across a single night can be quite significant as well, ranging from 20 km in local winter to 40 km in local summer. Over the mid-latitude site, we see peak altitudes 10 to 40 km above the 250 km assumption during local summer, and 10 to 20 km lower in local winter. The variation across a night is even more drastic, spanning 40 to 60 km. It is clear that the standard assumption that the emitting layer peaks at an altitude of 250 km is not appropriate most of the time, although one could argue that “on average” it is an appropriate value in some locations. The average peak altitude over Cariri was 239 km, while the average over Morocco was 261 km in the same time frame. Since most of the night is not at the 250 km assumption,

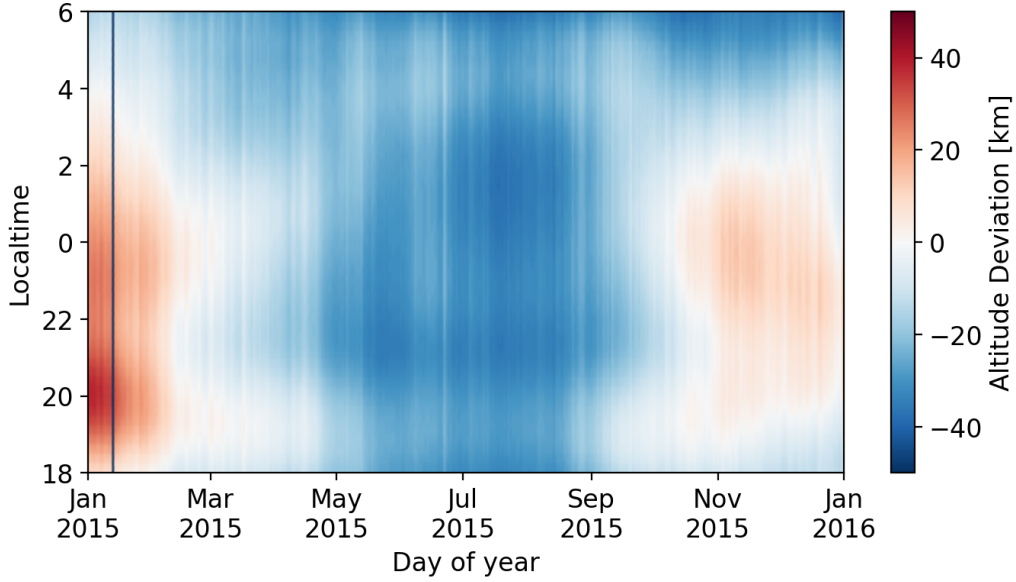


Figure 5.5: Deviations from assumed 250 km peak altitude of 6300 emission modeled over Cariri, Brazil, for 2015.

failing to take these dynamics into account could bias a comparison of data results to a model.

To account for the variability of the peak airglow layer affecting data-model comparisons, we calculate the airglow-weighted values to match with the FPI observations. *Chartier et al.* [2015] found that this approach produced more satisfactory results than assuming a fixed altitude of 250 km as this method is more representative of how an actual FPI takes measurements. Of course, the models used to predict the airglow layer’s volume emission rate are empirical models, and so the actual day-to-day variability in the layer altitude will not be captured. However, we are limited by lacking actual observations of the layer altitude, or a proxy such as *hmf2*.

The airglow-weighted values are estimated by

$$\hat{x} = \frac{\sum_z x_z a_z}{\sum_z a_z} \quad (5.1)$$

where x_z are the model values at altitude z and a_z is the calculated redline volume emission rate using the equations from *Link and Cogger* [1988] at altitude z . Here, x_z values could be winds from HWM or temperatures from MSIS.

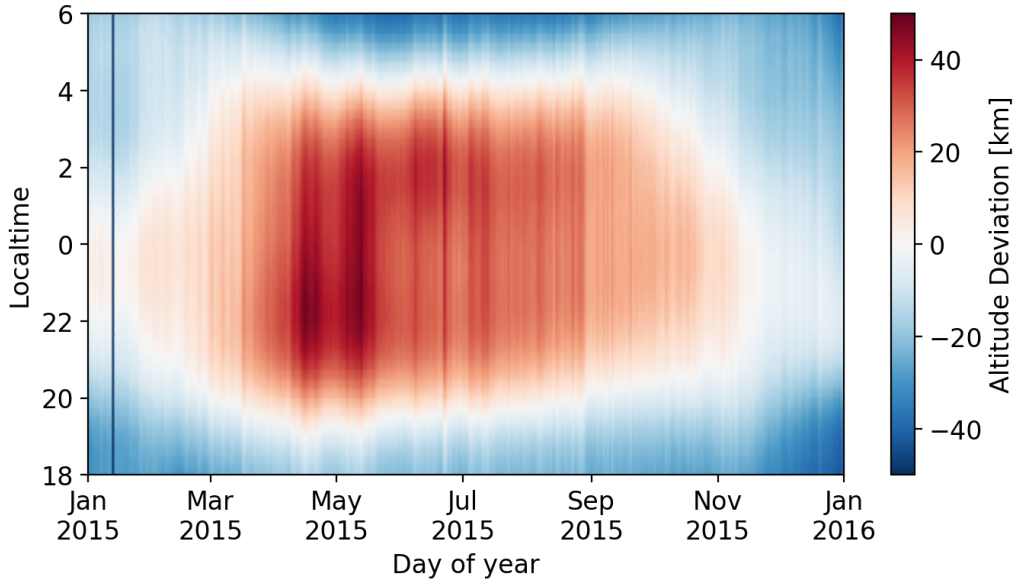


Figure 5.6: Deviations from assumed 250 km peak altitude of 6300 emission modeled over Oukaïmeden, Morocco, for 2015.

To validate *Chartier et al.* [2015] and see if the results hold for other geographic locations, we must examine the effect of airglow weighting on the model outputs. For each site, we have produced simulated measurements from the empirical models between 20 and 04 LT for five continuous years (2010 to 2015). First, we simulate the airglow peak altitude and compute the difference from 250 km (as was done for Figures 5.5 and 5.6). Second, we simulate the airglow-weighted parameters using Equation 5.1. Finally, we retrieve the model parameters at 250 km and compare them to the airglow-weighted values. For the study, HWM14 is used for the horizontal wind components and MSIS is used for the temperatures. We present scatter plots of the differences between the airglow-weighted model parameters and the 250-km parameters against the difference in peak altitude from Brazil in Figures 5.7, 5.8, and 5.9. We also provide the mean differences and standard deviations per hour in Table 5.1.

During these five years, we see that the peak variations from 250 km can lead to incorrectly retrieving the temperatures by ± 40 K. However, the average error is only 12 K before midnight and 7 K after midnight. It is interesting to see larger errors before midnight because the peak layer estimates are worse after midnight. This difference means that the vertical gradients must be much larger after sunset. The other worthwhile observation from the

Table 5.1: The mean differences in peak altitude, temperature, zonal wind, and meridional wind for the simulated measurements with and without airglow weighting over Cariri, Brazil, from 2010 to 2015. The standard deviations are also provided. Note that *hmag* is an abbreviation of the airglow peak altitude.

LT	Δ hmag [km]		ΔT [K]		Δu [m/s]		Δv [m/s]	
	μ	σ	μ	σ	μ	σ	μ	σ
20	-5.6	18.4	-11.1	13.2	-6.7	9.5	2.0	3.1
21	-10.1	18.9	-13.9	12.3	-7.7	7.9	2.4	3.0
22	-10.2	18.6	-12.3	11.0	-5.2	5.6	2.0	2.7
23	-8.2	18.7	-9.7	10.2	-2.9	4.1	1.7	2.9
00	-8.2	18.0	-8.3	9.0	-2.0	3.9	1.7	3.0
01	-10.0	16.2	-7.8	7.4	-2.5	4.3	1.7	2.5
02	-12.9	13.4	-7.5	5.5	-3.8	4.3	1.5	1.9
03	-15.5	10.0	-6.6	3.6	-4.2	3.5	0.9	2.1
04	-17.7	6.6	-6.1	2.7	-2.2	2.7	0.2	2.7

temperature plot is the 15 K spread of temperatures when the peak actually is at 250 km. That is, knowing the emission peak is not sufficient to accurately estimate the observed measurements because altitudinal gradients can exist for the thermospheric winds and temperatures within the emission layer to bias the results. Therefore, it is important to take the airglow-weighted values for model results to capture the effects from the neutral parameter gradients.

Similar results are seen in the two scatter plots of the horizontal wind components. Zonal winds could be off by -30 to 20 m/s (average: -4 m/s), while the meridional winds could be off by -5 to 12 m/s (average: 2 m/s). Another important observation from these plots is that each local time has a different response, and again, larger variations are seen before midnight. This observation is explained by the combination of varying airglow altitude ranges and different wind profiles. However, it appears that the magnitude of the winds/temperatures dominates this variation; when the temperatures and zonal winds are highest (from 20 to 22 LT) we see the largest differences. Gradients of the winds must increase with increasing wind speed, as a wind inversion exists lower in the atmosphere and the equilibrium speed is reached higher up.

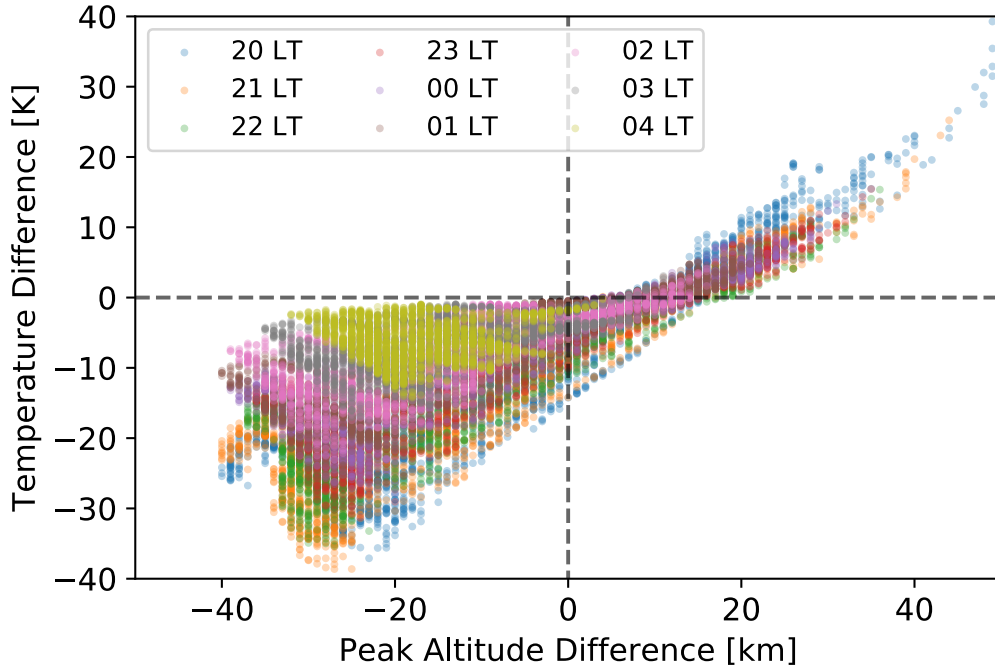


Figure 5.7: Deviations of MSIS temperatures vs. deviation from assumed 250 km peak altitude of 6300 emission modeled over Cariri, Brazil, for five years. The colors represent the differences at different local times.

Even though these changes are small with respect to typical thermospheric conditions, both the temperature and wind variations associated with this effect can be greater than the typical uncertainties from FPI-derived measurements. These results show that airglow weighting is necessary for accurate comparisons between model and data. Again, this conclusion relies on the validity of the airglow constituent models used to find the 630.0-nm profiles. Overall, these results are in agreement with the work of *Chartier et al.* [2015]; we see the biggest effects when the airglow peak is below the assumed 250 km height.

What has not previously been looked into is how the mid-latitude model results over Morocco would change with airglow weighting. The differences in the temperatures from MSIS, zonal winds from HWM14, and meridional winds from HWM14 are shown in Figures 5.10, 5.11, and 5.12, respectively. We also provide the hourly mean and standard deviation of those differences in Table 5.2. In this mid-latitude site, we also see differences in local time, due to a combination of altitude gradients and airglow peak changes. In the early night hours of 20 to 22 LT, we see the best correlation between

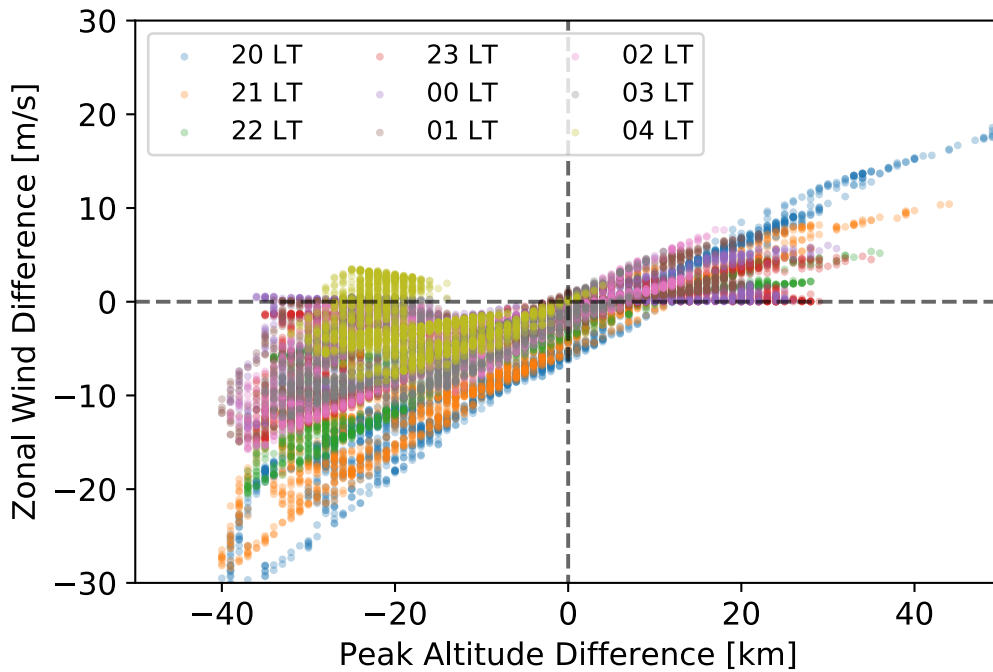


Figure 5.8: Deviations of zonal HWM winds vs. deviation from assumed 250 km peak altitude of 6300 emission modeled over Cariri, Brazil, for 2015.

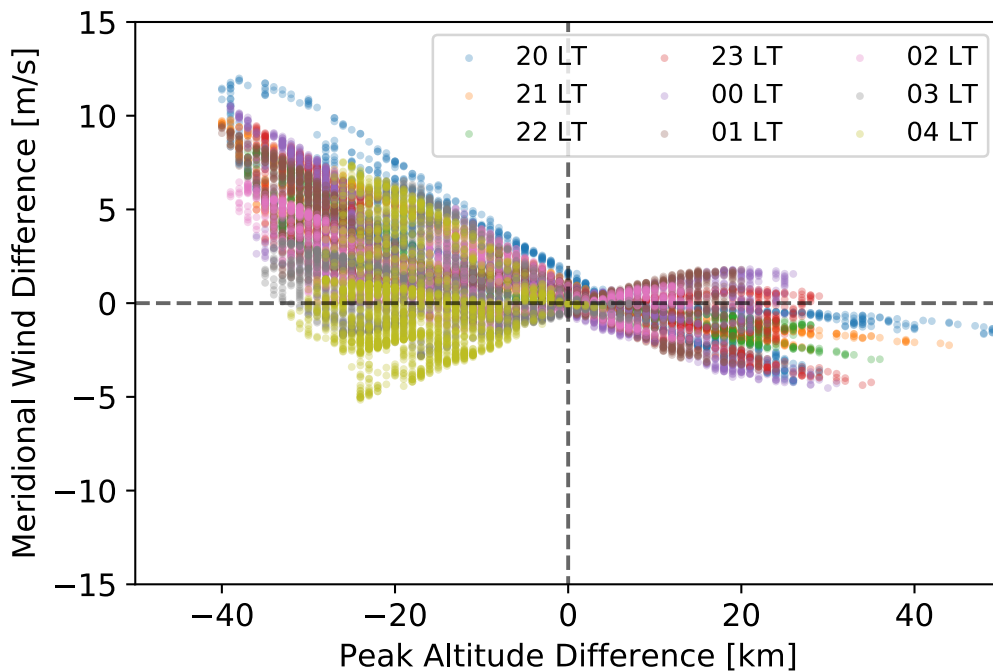


Figure 5.9: Deviations of meridional HWM winds vs. deviation from assumed 250 km peak altitude of 6300 emission modeled over Cariri, Brazil, for 2015.

Table 5.2: The mean differences in peak altitude, temperature, zonal wind, and meridional wind for the simulated measurements with and without airglow weighting over Oukaïmeden, Morocco, from 2010 to 2015. The standard deviations are also provided. Note that *hmag* is an abbreviation of the airglow peak altitude.

LT	Δ hmag [km]		Δ T [K]		Δ u [m/s]		Δ v [m/s]	
	μ	σ	μ	σ	μ	σ	μ	σ
20	0.0	11.7	-1.7	8.6	-0.2	4.5	0.2	1.1
21	12.3	14.6	3.6	7.0	3.5	4.1	-1.3	3.0
22	17.8	15.1	3.1	4.4	3.2	2.6	-3.6	4.1
23	18.8	14.1	2.1	3.1	1.8	1.5	-4.2	3.8
00	18.1	14.1	1.5	2.7	0.6	1.2	-3.2	3.0
01	16.9	15.9	1.1	3.0	-0.1	1.3	-1.2	2.0
02	14.3	18.0	0.9	3.7	-0.5	1.7	0.8	1.1
03	8.4	16.7	0.6	4.2	-0.8	2.0	1.3	1.1
04	-1.7	11.2	-1.0	3.1	-0.2	1.5	0.2	1.2

altitude difference and wind/temperature difference. This time corresponds to when the neutral temperatures and zonal winds are strongest, too. The temperature spread at 250 km also shows a need to account for altitudinal gradients. Over the same five years, the temperature differences range from -20 to 30 K (average: 1 K), the zonal wind differences range from -12 to 12 m/s (average: 1 m/s), and the meridional wind differences range from -15 to 7 m/s (average: 1 m/s). While the deviations seen in the temperatures and zonal winds are not as large as those seen in low-latitude Brazil, the meridional winds are of the same magnitude; none of the ranges are negligible as they also can be larger than the typical measurement uncertainties. However, unlike at low-latitudes, the mid-latitudes still saw substantial changes when the peak airglow layer was above 250 km. This result shows that the direction of the peak altitude difference does not matter; assuming the 250 km emission layer will lead to incorrect results.

The amount of variation seen confirms the necessity to use airglow weighting in data-model comparisons for better accuracy. The airglow weighting is applied for these comparisons only, in order to better mimic how the FPI takes measurements. Therefore, we can justify the increase in computation time required to get airglow-weighted values at all geographic coordinates be-

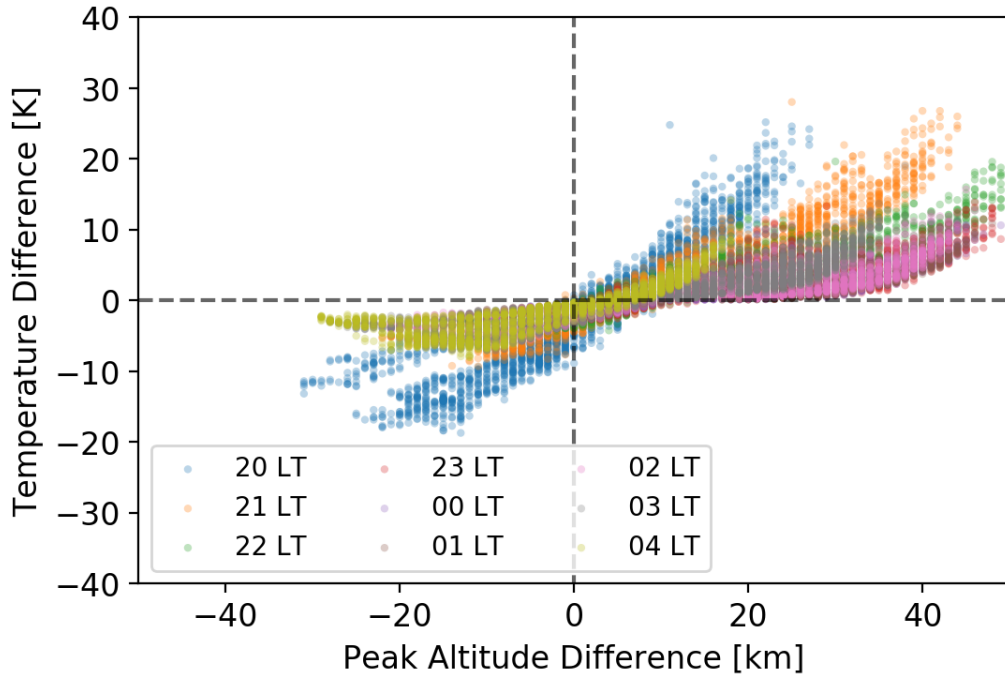


Figure 5.10: Deviations of MSIS temperatures vs. deviation from assumed 250 km peak altitude of 6300 emission modeled over Oukaïmeden, Morocco, for five years. The colors represent the differences at different local times.

cause it will account for differing gradients in the neutrals during the night. Unfortunately, there is nothing we can do with the measurements themselves to figure out the peak emission altitude or find any altitudinal gradients in the winds. However, the model results show that gradients in the winds do affect the FPI measurements. Applying this to our instruments, we note that actual gradients in the winds could be biasing our measurements, especially early in the night. The FPI can only estimate one Doppler velocity along a single line of sight (LOS), meaning that gradients along that LOS will be averaged out. Temperatures would be artificially enhanced by this as a wider airglow spectrum results in higher temperature estimates. Additionally, this means that the wind estimate will be heavily dependent on the airglow peak location. Since neither the peak height nor the gradients can be determined using the FPI alone, we cannot quantify the biases to our temperature or wind measurements. Finally, we must emphasize that this simulation depends on the accuracy of three models: IRI, MSIS, and HWM. We found that the altitudinal gradients can affect the HWM14 wind estimate, but this assumes the gradients are real. The three models represent climatological

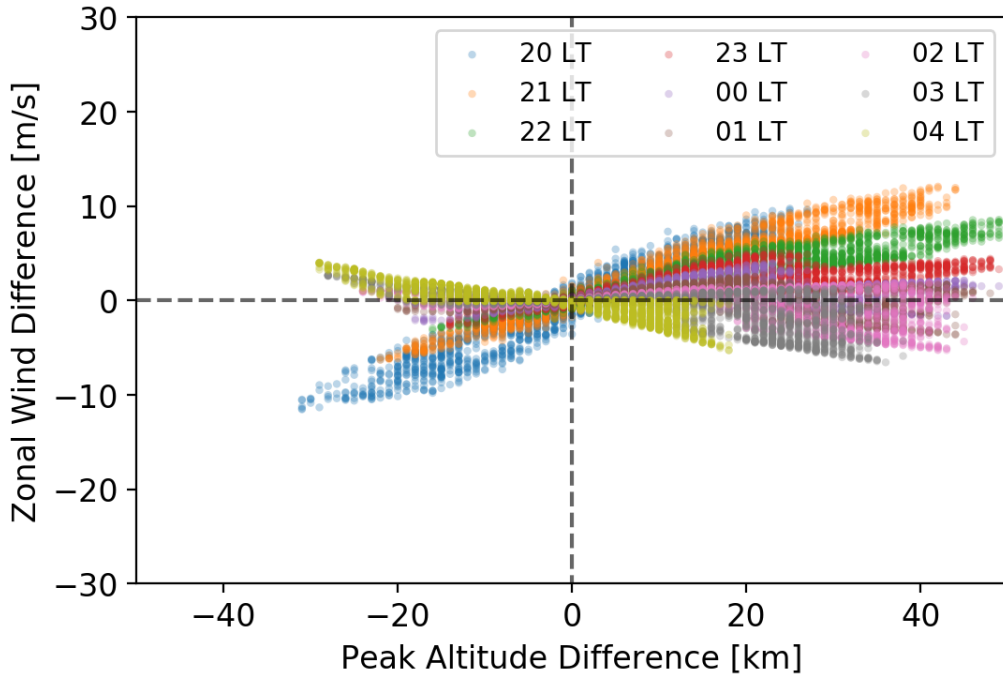


Figure 5.11: Deviations of zonal HWM winds vs. deviation from assumed 250 km peak altitude of 6300 emission modeled over Oukaïmeden, Morocco, for 2015.

averages of the thermosphere/ionosphere; day-to-day fluctuations would not be captured and could lead to larger errors in the wind estimates than predicted in the prior figures. Furthermore, HWM may have generated artificial gradients due to lack of measurements in the lower thermosphere, meaning the wind differences found in this section could be overestimated, especially when the peak is below 250 km.

5.3 Using Data to Validate HWM14

The horizontal wind model is the standard model for upper atmospheric neutral winds. One of the biggest changes made from HWM93 to HWM07 was the separation of disturbance winds from the baseline horizontal winds [Drob *et al.*, 2008]. This change has held over to the most recent version, HWM14 [Drob *et al.*, 2015], making it ideal for comparison with the quiet-time climatologies presented in Chapter 4. Furthermore, solar flux is not an input to the HWM model, as the outputs are averages over all solar flux conditions. The

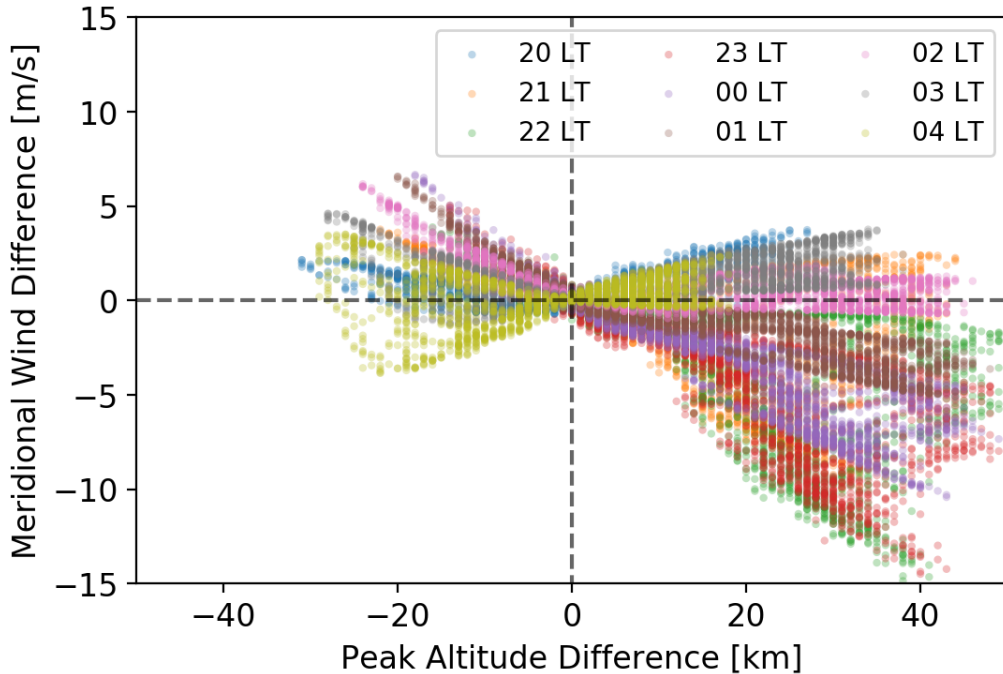


Figure 5.12: Deviations of meridional HWM winds vs. deviation from assumed 250 km peak altitude of 6300 emission modeled over Oukaïmeden, Morocco, for 2015.

lack of solar dependence in the model also enables us to combine all years of wind data to increase the number of samples in our monthly averages. This means that HWM14 winds are based only on geographic latitude, longitude, altitude, date, and time. The gaps are filled in using spherical harmonic functions, which include diurnal, semidiurnal, and terdiurnal harmonics and annual and semiannual variations. Updates from HWM07 to HWM14, on top of adding new ground-based datasets, set the spherical harmonic equations so that the horizontal winds are zero at the poles [Drob *et al.*, 2015]. Below, we use our measurements to validate the output of HWM14. In certain locations (North America and Brazil), our measurements were used in developing HWM, and so the results presented can be viewed as a study in understanding the effects of combining ground and space-based measurements. Over Africa, however, none of our measurements were used in constructing the model, so the results represent an independent validation of the model.

In this section, we compare the measured neutral winds to the thermospheric wind patterns predicted by the horizontal wind model and expand on the results originally presented in Kaab *et al.* [2017]. The analysis is simi-

lar to that performed by *Yuan et al.* [2013] for observations made at Xinglong station in central China. The goal is to investigate the long-term variations of the thermospheric winds and see how well the general trend is captured by the airglow-weighted neutral winds of HWM14. This method is ideal for use with HWM14 because it breaks down the winds into local time harmonics, which matches how the model was constructed. Month-by-month climatological comparisons are possible, but the lack of day-to-day fluctuation in the model makes the comparison more challenging. Our analysis extracts the annual, semiannual, and terannual variations from the full multi-year quiet-time FPI observations and compares them to the same harmonics found in HWM14.

5.3.1 Harmonic Analysis Methodology

We utilize a fast Lomb-Scargle periodogram to extract the dominant frequencies from each local time. Lomb-Scargle is a least-squares spectral fit, often called a periodogram, designed to perform frequency analysis on non-uniformly sampled data. This method is preferred over the fast Fourier transform because it minimizes the addition of spectral information created when filling in data gaps. We choose to utilize the Palmer chi-squared implementation as it is a fast, low-error method of computing a Lomb-Scargle periodogram that makes full use of the measurement uncertainties [*Palmer, 2009*].

Here, we choose to look at five local times over the observation period; pre-midnight (20 and 21 LT \pm 15 min), midnight (00 LT \pm 15 min), and post-midnight (03 and 04 LT \pm 15 min). Utilizing all possible data at a maximum of one sample per night, we potentially get resolution ranging from two days to multi-year periods. We choose to search 2,000 periods in the range of 18 days to two years. This will allow the desired annual, semiannual, and terannual frequencies to be analyzed, along with higher order frequencies such as a quatrannual or lunar frequency, without adding noise from the high frequency daily fluctuations.

For each local time, we run a series of three Lomb-Scargle periodograms with a least-squares fit, allowing parameters to be found for the three desired harmonic variations. Separate frequency analyses are done for the meridional

and zonal winds because they are binned independently. We begin by creating a periodogram from the data. It is from this first periodogram that we find the peaks (using an automated peak-finding routine) to capture frequencies with large power. This is necessary in order to claim if a harmonic is or is not present in the data. If no peak is recognized near the desired harmonic, we set an amplitude of zero and do not record a phase. Peaks are only counted if they surpass the 92nd percentile of the total signal, preventing noisier signals from returning false peaks in a standardized methodology. This threshold was chosen because the periodograms resemble a half-normal distribution and the 92nd percentile is three standard deviations above the mean. Figure 5.13 shows an example of the Lomb-Scargle periodogram using Moroccan data at 04 LT with markings for the peaks at the desired harmonics.

The next step is to use a least-squares model to return the best-fit wave with a frequency of once per year. From this wave, we extract an offset, O , and peak amplitude, A , in m/s as well as phase, ϕ . Here, we follow the definition set by *Yuan et al.* [2013] where phase corresponds to the point of maximum amplitude, reported in units of day of year (DOY). This wave is then subtracted from the observational data to get residuals used in the following Lomb-Scargle analysis. A best fit then returns the same parameters for the semiannual frequency. This cycle is repeated one last time to pull out harmonic results for the terannual frequency. Both the model data and the Fabry-Perot measurements are decomposed in this manner. If desired, this method can easily be extended to pull out quatrannual and higher harmonics. It is worth noting that a 27-day harmonic is not discussed in this section as it is not certain if the peaks are physical or artifacts from the analysis. The 27-day period could be from contamination of a lunar origin; not only does the FPI avoid looking near the moon, changing the routine observation strategy, but scattering off of the dome from the bright moon can potentially contaminate images systemically.

Additionally, a Monte Carlo simulation was run to study the susceptibility of the Lomb-Scargle analysis to noisy data. We use 1,000 trials of our Lomb-Scargle periodogram analysis for each local time at each site. A dataset for the simulation is created using a set of random numbers generated from individual normal distributions, where each normal distribution is formed using the wind velocity estimate as the mean and the measurement uncertainty as

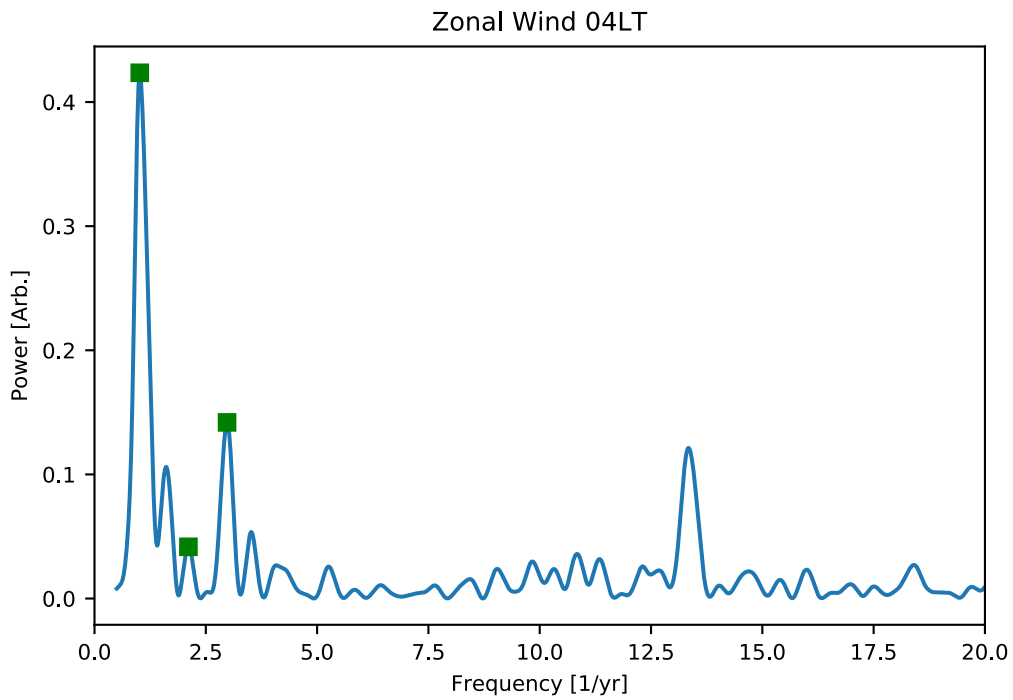


Figure 5.13: An example Lomb-Scargle periodogram of zonal winds over Oukäimeden Observatory at 04 LT. The squares represent the locations of the peaks at the annual, semiannual, and terannual harmonics. In this case, the semiannual peak is within the noise floor. Note the peak around the frequency of 13 times per year signifies a significant 27-day harmonic.

the standard deviation. The measurement uncertainties are also used as the weights for each dataset. The Monte Carlo returns the mean and standard deviation of the periodogram-derived amplitudes and phases for the annual, semiannual, and terannual periods.

While characterizing HWM using the results from the Lomb-Scargle analysis can give a big-picture view of the model’s success, the performance over the course of a year cannot be easily distilled from a few numbers. We utilize the components from the Lomb-Scargle analysis to recreate the non-linear best-fit waveform. Not only do best-fit sinusoids make it easier to determine how well the phasing and amplitude weights combine to fit the data/model, but we can also use simple statistical techniques, such as a least-squares regression, to get quantitative measures of success. Utilizing the annual, semiannual, and terannual harmonic components, we can calculate the best-fit waveform as

$$H^h[t] = \sum_{f=1}^3 A_f^h \cos\left(\frac{2\pi(t - \phi_f^h)}{365.25/f}\right) + O^h. \quad (5.2)$$

Here, t is the date, A_f^h and ϕ_f^h are the amplitude and phase, respectively, of the harmonic with frequency f at local time h , and O^h is the offset at local time h . ϕ and t are in units of days, with a value of 0 representing January 1 (subtract 1 from a DOY). f is in units of 1/year. We refer to the data-driven harmonic fit as the harmonic or data fit while the HWM14 best-fit waveform will be referred to as the HWM or model fit. We plot the best-fit waveforms for the meridional and zonal winds from both the FPI measurements and HWM14 on top of the individual measurements to visualize how well the reconstructed waveforms fit, with darker points signifying measurements with smaller uncertainty. We choose to simplify the plots by only including three times (20 LT: post-sunset, 00 LT: midnight, and 04 LT: pre-sunrise). Furthermore, because there is no solar-cycle variation in HWM, there is a negligible solar-cycle variation in the data, and the harmonic fits have a maximum period of one year, we collapse the x-axis to one year and plot all data on this modulo scale.

In order to accurately characterize the success of the waveforms, we perform two analyses. First, we calculate an uncertainty-weighted, least-squares regression on both fits. The residuals of the model fit are compared to those of the data fit. This is a fair comparison because the model fit is only calcu-

lated at the time of each measurement. Second, we calculate the local time biases of the fits. This is computed from a sliding 30-day weighted average of the wind measurements for each day of year, DOY 1 to 366. The running average is subtracted from the model and data fits in order to find when the fits under and overestimate the observations.

5.3.2 Harmonic Analysis Results

The Lomb-Scargle harmonic analyses have been completed for our sites in Brazil, the United States, and Morocco at 20, 21, 00, 03, and 04 LT resulting in amplitude and phase estimates for the annual, semiannual, and terannual harmonics for both our FPI data and HWM14. These components of the zonal and meridional winds are compared in Tables 5.3 and 5.4, respectively. We have chosen to only include three specific sites to keep the table manageable and still capture the large-scale variation (as sites in close proximity are generally in good agreement to one another). All quiet-time data ($K_P < 4$) available through 2016 were used in constructing the Lomb-Scargle periodograms. Also note that an amplitude of 0.0 means not necessarily that the component is not present, but that it is in the noise floor of the frequency spectrum and cannot be determined.

Utilizing the data from these two tables, the offset calculated from the Lomb-Scargle analyses (not shown), and Equation 5.2, we reconstruct the harmonic waveform at each local time and site for both the meridional and zonal winds. Table 5.5 displays the residuals found from an uncertainty-weighted, least-squares regression for the harmonic and model fits. The ratio between the model residual and data residual is also given in the table, with values greater than 100% signifying that HWM14 has a worse fit than the harmonic fit.

The Monte Carlo simulation of the all three sites showed that the amplitude estimates are robust to noise, with a less than 1-m/s standard deviation for all harmonics at all local times. The phase is less robust, with a 20-day standard deviation on average for all local times and harmonics. This result confirms that the Lomb-Scargle technique can accurately return amplitudes and phases (within ± 20 days) from the FPI measurements. Given this, the following sections summarize the results of the harmonic analysis for Cariri,

Table 5.3: The annual, semiannual, and terannual harmonic fits to the zonal winds for both FPI data and HWM14 at 20, 00, and 04 LT. The amplitude is in m/s and the phase (in parenthesis) is in DOY.

LT	Location	FPI Data			HWM14		
		Annual	Semi.	Ter.	Annual	Semi.	Ter.
20	Cariri, Brazil	27.8 (325)	2.9 (42)	6.7 (56)	32.6 (360)	3.1 (137)	0.0 (N/A)
	PARI, USA	28.9 (364)	0.0 (N/A)	0.0 (N/A)	22.9 (365)	10.5 (156)	0.0 (N/A)
	Oukaïmeden, Morocco	30.6 (17)	8.5 (145)	3.0 (57)	26.4 (363)	15.5 (146)	1.4 (114)
21	Cariri, Brazil	26.1 (330)	0.0 (N/A)	0.0 (N/A)	27.4 (351)	3.7 (167)	0.0 (N/A)
	PARI, USA	32.7 (366)	0.0 (N/A)	4.8 (3)	28.1 (363)	7.7 (156)	0.0 (N/A)
	Oukaïmeden, Morocco	31.1 (23)	6.4 (124)	6.3 (74)	29.1 (362)	12.6 (147)	0.0 (N/A)
00	Cariri, Brazil	9.2 (209)	7.1 (180)	4.4 (107)	7.2 (258)	10.7 (176)	2.5 (30)
	PARI, USA	33.1 (361)	2.6 (82)	0.0 (N/A)	39.5 (358)	0.0 (N/A)	0.0 (N/A)
	Oukaïmeden, Morocco	8.6 (58)	9.2 (31)	7.2 (68)	46.8 (357)	4.6 (74)	0.0 (N/A)
03	Cariri, Brazil	5.4 (45)	0.0 (N/A)	0.0 (N/A)	6.2 (196)	11.3 (171)	2.1 (12)
	PARI, USA	39.3 (364)	10.2 (167)	6.4 (72)	39.9 (354)	0.0 (N/A)	0.0 (N/A)
	Oukaïmeden, Morocco	43.7 (365)	5.4 (19)	3.3 (70)	59.0 (360)	0.6 (5)	0.0 (N/A)
04	Cariri, Brazil	5.7 (60)	0.0 (N/A)	4.2 (55)	2.9 (196)	4.7 (182)	1.4 (23)
	PARI, USA	25.1 (364)	11.6 (174)	2.4 (59)	42.2 (357)	0.0 (N/A)	0.0 (N/A)
	Oukaïmeden, Morocco	38.5 (4)	6.5 (36)	6.6 (57)	59.4 (362)	2.1 (124)	0.0 (N/A)

Table 5.4: The annual, semiannual, and terannual harmonic fits to the meridional winds for both FPI data and HWM14 at 20, 21, 00, 03, and 04 LT. The amplitude is in m/s and the phase (in parenthesis) is in DOY.

LT	Location	FPI Data			HWM14		
		Annual	Semi.	Ter.	Annual	Semi.	Ter.
20	Cariri, Brazil	59.9 (356)	3.1 (78)	3.8 (98)	59.8 (355)	0.0 (N/A)	0.0 (N/A)
	PARI, USA	20.3 (16)	2.5 (16)	5.2 (118)	20.0 (365)	3.4 (69)	0.0 (N/A)
	Oukaïmeden, Morocco	11.9 (352)	8.0 (7)	7.4 (116)	30.1 (10)	2.6 (113)	0.0 (N/A)
21	Cariri, Brazil	56.4 (357)	7.3 (135)	0.0 (N/A)	53.4 (354)	0.0 (N/A)	0.0 (N/A)
	PARI, USA	11.1 (9)	3.9 (181)	5.8 (14)	19.4 (23)	0.0 (N/A)	0.0 (N/A)
	Oukaïmeden, Morocco	9.4 (309)	3.6 (31)	3.8 (15)	31.2 (18)	3.2 (144)	0.0 (N/A)
00	Cariri, Brazil	26.5 (360)	5.6 (84)	3.3 (62)	27.5 (348)	5.2 (127)	0.0 (N/A)
	PARI, USA	17.0 (364)	4.2 (30)	5.7 (5)	17.2 (31)	5.1 (174)	1.4 (75)
	Oukaïmeden, Morocco	35.1 (344)	4.2 (40)	5.7 (62)	24.9 (24)	9.2 (150)	0.0 (N/A)
03	Cariri, Brazil	14.5 (6)	7.6 (65)	3.0 (29)	24.2 (359)	2.3 (26)	0.0 (N/A)
	PARI, USA	26.8 (329)	5.9 (95)	3.2 (21)	25.0 (360)	12.2 (98)	0.0 (N/A)
	Oukaïmeden, Morocco	39.1 (362)	6.5 (126)	0.0 (N/A)	30.5 (360)	14.5 (99)	0.0 (N/A)
04	Cariri, Brazil	9.2 (14)	5.0 (67)	3.4 (104)	22.1 (355)	3.7 (33)	0.0 (N/A)
	PARI, USA	30.5 (330)	6.0 (98)	2.3 (10)	32.1 (352)	18.5 (95)	0.0 (N/A)
	Oukaïmeden, Morocco	38.8 (355)	8.2 (90)	3.6 (10)	37.4 (355)	17.3 (115)	0.0 (N/A)

Table 5.5: Residuals of the harmonic fit and HWM14 to the weighted mean of the measurements. The ratio is defined as the HWM14 residual over the harmonic fit residual, given as a percent.

LT	Location	Zonal			Meridional		
		Harmonic	HWM14	Ratio	Harmonic	HWM14	Ratio
20	Cariri, Brazil	1197	1248	104%	773	889	115%
	PARI, USA	686	3743	546%	637	695	109%
	Oukaïmeden, Morocco	677	1928	285%	584	791	136%
21	Cariri, Brazil	1054	1123	107%	563	638	113%
	PARI, USA	827	2848	344%	679	841	124%
	Oukaïmeden, Morocco	744	1484	200%	499	1117	224%
00	Cariri, Brazil	774	819	106%	369	428	116%
	PARI, USA	961	2030	211%	990	1157	117%
	Oukaïmeden, Morocco	662	1521	230%	558	1183	212%
03	Cariri, Brazil	831	948	114%	576	797	138%
	PARI, USA	671	988	147%	957	1278	134%
	Oukaïmeden, Morocco	659	906	137%	597	627	105%
04	Cariri, Brazil	640	922	144%	449	675	150%
	PARI, USA	784	1118	143%	1028	1189	116%
	Oukaïmeden, Morocco	810	1959	242%	828	929	112%

PARI, and Morocco individually.

5.3.3 Harmonic Analysis over Northeastern Brazil

We first look at the results of the Lomb-Scargle analysis over Cariri, Brazil, from Tables 5.3 and 5.4. The most obvious trend seen is the dominant annual harmonic. The amplitude of the annual component is largest during all studied local times for both the zonal and meridional winds. The average phase is DOY 3 with a standard deviation of 33 days, if you remove the midnight meridional component that is nearly 180 degrees out of phase. The semiannual component has more local time variation than the annual; three of the local times have no statistically significant, meridional semiannual amplitude and the zonal semiannual amplitude at midnight is nearly equal to the annual amplitude. The phase of the semiannual harmonic is DOY 67 with a 40 day standard deviation. Over Brazil, a terannual component exists in the data during a majority of local times. In fact, terannual amplitudes are larger, or nearly equal to, the semiannual amplitude at 20 LT and 04 LT in the zonal winds and at 00 LT in the meridional winds. The phase of the terannual component is DOY 73, with a standard deviation of 30 days.

Turning to HWM14, there is fairly good agreement with the annual harmonics found in the FPI data for both the zonal and meridional winds. Most amplitudes match closely with the data within 5 m/s and the phase matches well, too. However, when the zonal amplitude is smaller than the semiannual amplitude (after midnight in Brazil), HWM14's non-dominant peak is nearly 180 degrees out of phase. Outside of these cases, HWM14's annual harmonic has a mean phase of DOY 355, which is within the standard deviation of the measurements. Regarding the semiannual amplitudes, HWM14 is not in good agreement with the data as to when the semiannual component is present, especially in the zonal winds after midnight where HWM14 shows a dominant semiannual component and the data show little semiannual contribution. The average phase is DOY 127 with a standard deviation of 63 days.

We now turn to analyzing the harmonic reconstructions over Brazil. Presumably, since some of the measurements from this site went into the updated HWM model, the comparison should be good. Figures 5.14 and 5.15 show

the zonal and meridional harmonic reconstructions, respectively, for 20, 00, and 04 LT. On the whole, the reconstructed winds do a very good job capturing the zonal and meridional winds, especially at midnight. The HWM14 amplitudes are on the correct order but there are underestimated zonal winds at 20 LT during August (up to 27 m/s) and 04 LT from February to May (up to 28 m/s). From July through December of 20 LT, the meridional winds are overestimated by the model by about 20 m/s. Similarly, at 04 LT, HWM14 overestimates the meridional winds from November to March by up to 35 m/s. Given that the day-to-day variation of these winds is 20 to 40 m/s, the model's estimates are reasonable.

However, when comparing HWM14's least squares residuals to our harmonic fit, we find that our method is always better than HWM14 at fitting the data. The residuals and ratios of these fits are presented in Table 5.5. The pre-sunrise HWM fits, compared to the earlier night, are much worse than our harmonic fit, with $\sim 50\%$ larger residuals for both the meridional and zonal winds. This is important because it supports that our fitting technique, which includes a terannual component, is superior for this location. Therefore, the HWM14 model fit, which is already accurate from ingesting parts of this dataset, could further improve its fitting if the third harmonic was added.

5.3.4 Harmonic Analysis Over PARI

Tables 5.3 and 5.4 also contain the Lomb-Scargle analysis over PARI, NC. The largest harmonic at each local time for the zonal and meridional winds is the annual variation. The phase is centered at DOY 360, with a standard deviation of 17 days. The semiannual component is usually the second largest in amplitude, with exceptions at 21 LT in the zonal winds and at 20, 21, and 00 LT in the meridional winds. The average phase for the semiannual component is DOY 105, with a 64-day standard deviation, and the average phase for the terannual component is DOY 38, with a 40-day standard deviation. Note that a terannual harmonic is small (but detectable) in both the meridional and zonal winds at most local times.

HWM14's annual component matches the data well over PARI, with amplitudes usually within 5 m/s of the data. The mean phase of the annual

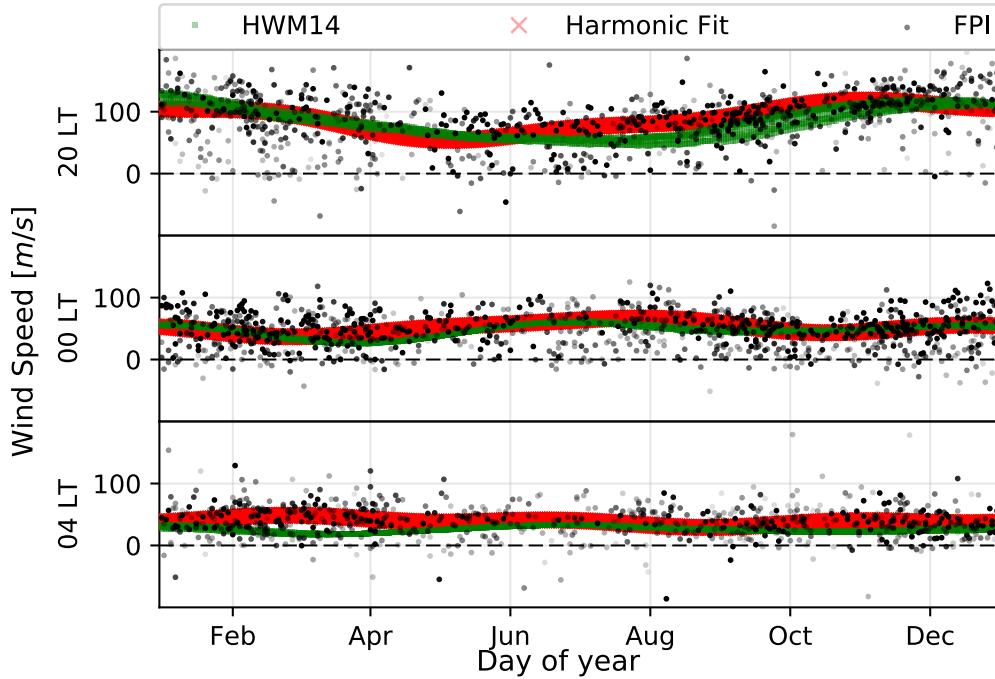


Figure 5.14: Best fit harmonic reconstruction of FPI data and HWM14 for the zonal winds over Cariri, Brazil, at set local times. The data points are shaded by uncertainty.

harmonic matches as well (DOY 1, with a standard deviation of 15 days). The semiannual component of HWM14 does not share this good agreement as there is little correlation between the the data and model. The mean phase of HWM14 is DOY 125 with a standard deviation of 43 days.

HWM14 also ingested some of our ground-based FPI measurements over PARI, so comparisons with HWM14 should also lead to good agreements. We choose to compare with PARI, instead of one of the other four US FPIs, because (1.) it has been running the longest, and (2.) it is at nearly the same geographic latitude as our Moroccan site. The other NATION sites reveal similar findings to that of PARI, due to the fact that they are all located in close proximity to each other in the eastern/central United States and the analysis is concerned with large-scale structure.

We present the reconstructed best fit compared to HWM14’s zonal and meridional winds in Figures 5.16 and 5.17. HWM14 is in good agreement with the data and our harmonic fit for the meridional winds, with only a few differences. These differences are underestimates from August to December at 00 LT (by up to 26 m/s), June to August at 04 LT (by up to 31 m/s),

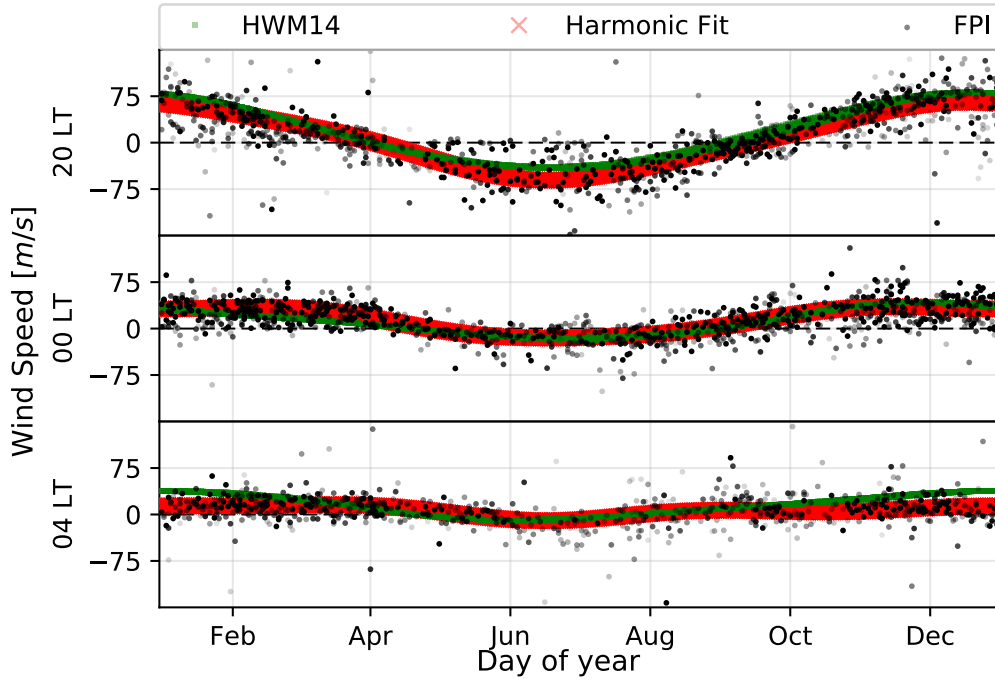


Figure 5.15: Best fit harmonic reconstruction of FPI data and HWM14 for the meridional winds over Cariri, Brazil, at set local times. The data points are shaded by uncertainty.

and December to February at 04 LT (by up to 31 m/s). Visually, it appears that modifying the phasing and amplitudes of the semiannual harmonic and adding a terannual harmonic would correct this. Note that all meridional local times presented here contain a terannual harmonic in the data fit, which has a 8% to 25% lower residual than the terannual-lacking model fit.

On the other hand, the model is in poor agreement with the zonal winds. HWM14 has a bias that overestimates the early evening winds by 54 m/s, and the winds at midnight by 31 m/s. The winds at 04 LT are not biased like the other local times but they are lacking the semiannual and terannual harmonic. This causes up to a 42 m/s underestimation from May through August. This finding compliments and expands upon the early HWM14 analysis done by *Fisher et al.* [2015] who found that HWM overestimated zonal winds in this mid-latitude region. As the model zonal fits presented here do not contain a terannual component, the improvement seen with our waveform shows that the ground-based measurements should be weighted more when HWM refits the annual and semiannual parameters over this region.

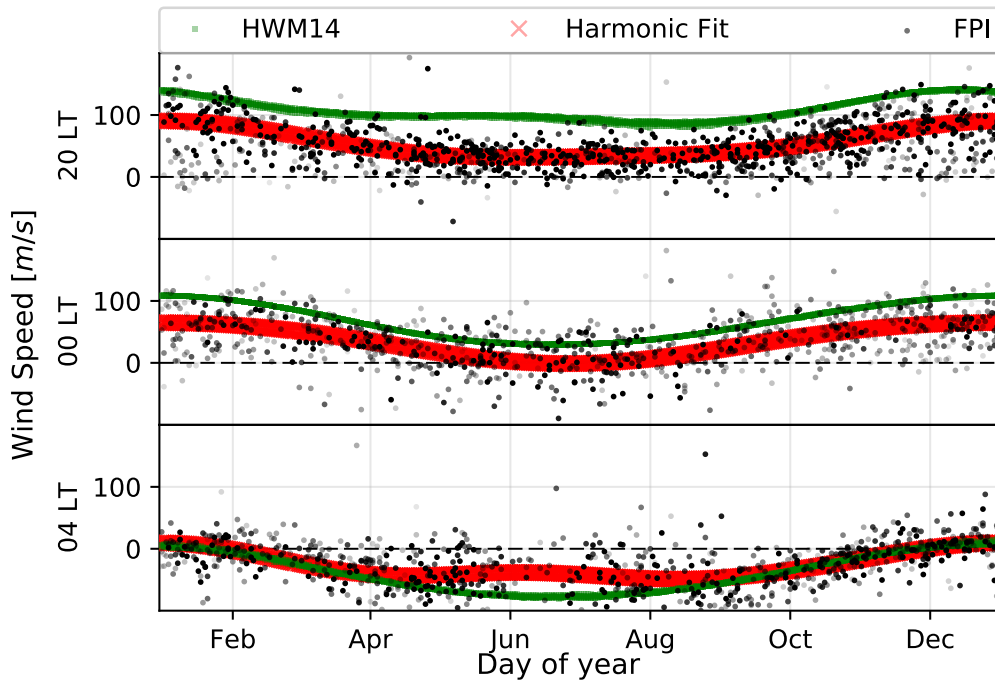


Figure 5.16: Best fit harmonic reconstruction of FPI data and HWM14 for the zonal winds over PARI at set local times.

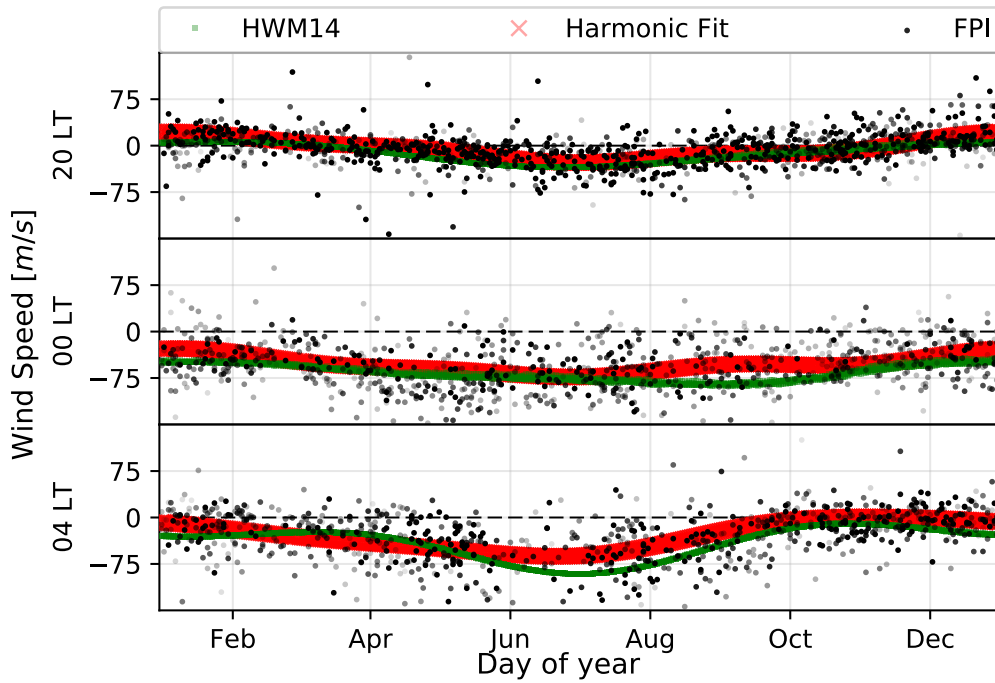


Figure 5.17: Best fit harmonic reconstruction of FPI data and HWM14 for the meridional winds over PARI at set local times.

5.3.5 Harmonic Analysis over Morocco

Finally, we discuss Tables 5.3 and 5.4 pertaining to the Lomb-Scargle analysis over Oukaïmeden, Morocco. The annual harmonic is dominant in amplitude for all local times except for the midnight zonal winds where all three harmonics are nearly equal in amplitude. The mean phase of the annual component is DOY 365, with a standard deviation of 30 days. Moroccan data include a discernible semiannual harmonic at all local times, even though they are all less than 10 m/s. However, the semiannual harmonic is not always the second largest, as a larger or nearly equal amplitude terannual component is seen at 21, 00, and 04 LT in the zonal winds and at 20, 21, and 00 LT in the meridional winds. The average semiannual phase is DOY 65, with a standard deviation of 51 days, and the average terannual phase is DOY 59, with a standard deviation of 32 days. Nearly all local times have a terannual component in the meridional and zonal winds.

The Moroccan HWM winds do not agree with the annual amplitudes seen in the data, often with more than 20 m/s differences. However, the average phase, DOY 2, does match that found in the data, well within the 12-day standard deviation. Additionally, the Moroccan HWM winds do not agree with the semiannual amplitudes seen in the data. The average phase for the semiannual component is DOY 112, with a standard deviation of 45 days.

Since none of the ground-based measurements of the thermospheric wind from the African sector were included in the reformulation of HWM, a comparison between the Oukaïmeden FPI-data harmonic fit and HWM14 becomes an independent validation for regions previously measured only via satellite passes. This section is an extension of work completed by *Kaab et al.* [2017] who used the first two years of FPI data in a comparison to HWM14; we extend this by another year with improved harmonic-analysis code. It is worth noting that due to dimmer airglow emissions occurring after midnight, fewer measurements can be taken as exposure time is increased to improve the signal-to-noise ratio. This reduction in samples negatively impacts the accuracy of our analysis later in the night.

Figures 5.18 and 5.19 show the three years of zonal and meridional wind data above Oukaïmeden along with the best-fit harmonic curves for the measurements and HWM14. We see a trend similar to that of the mid-latitude PARI site; HWM14 has a better fit with the meridional winds than zonal

winds. While no biases exist in the HWM14 meridional wind fits, we do see larger disagreements. For 20 LT, there is an overestimate from the data by ~ 20 m/s between November and April and an underestimate of ~ 20 m/s from April to October. At 00 LT, the winds are underestimated by up to 33 m/s from August to April and overestimated in May by 29 m/s. This suggests the amplitude of the annual component of the meridional winds is improperly fit here, in agreement with results found in Table 5.4. The HWM annual harmonic is seen to match our harmonic fit at 04 LT, which also agrees with results from the table. When comparing residuals between the fits, we again find the harmonic fit to be 10 to 40% better.

As in PARI, biases also exist in HWM14’s estimated zonal winds. The 20 LT winds are overestimated by an average of 38 m/s and the 04 LT winds are underestimated by an average of 29 m/s. However, the midnight winds show no bias, but do appear to be missing the correct amplitude of the annual harmonic as winds are 40 m/s overestimated October through February and 35 m/s underestimated May through August. So, too, does the 04 LT HWM fit not weight the annual component correctly because the March through August measurements are 60 m/s underestimated from the data while the September to February winds nearly match the data. Based on the residuals, the HWM14 fits are one to three times worse than the data-driven fits.

The improvement in fit, seen by using the harmonic fit over HWM14, suggests that this dataset be added to the next HWM iteration to help improve the model’s representation of the northwest African sector. This is especially pressing since the annual amplitudes seem to be the largest cause of differences (in addition to the biases). Since the differences between the average data and model are so large, it is difficult to determine if the differences are enhanced due to an incorrect semiannual phasing or a complete lack of terannual period. The analysis of the HWM14 horizontal wind fit over Morocco supports what was initially seen in *Fisher et al.* [2015] and validates what was discussed in *Kaab et al.* [2017]. The model residuals are 5% to 124% larger than those of the harmonic fit. The harmonic reconstructions nearly all contain a terannual component, signifying that the inclusion of the terannual period could improve future iterations of the model.

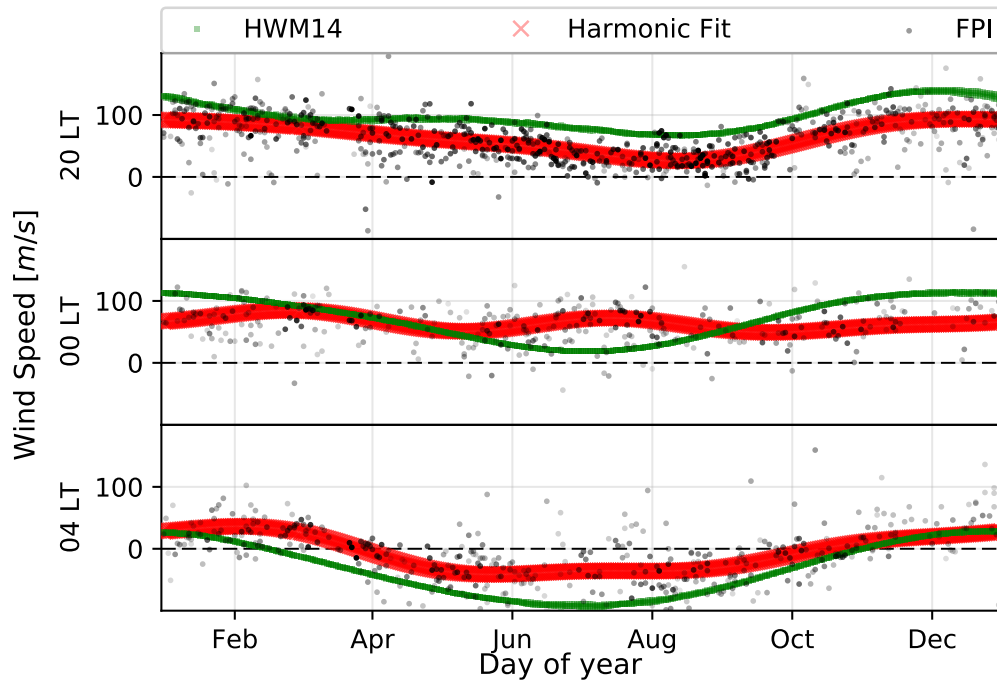


Figure 5.18: Best fit harmonic reconstruction of FPI data and HWM14 for the zonal winds over Morocco at set local times.

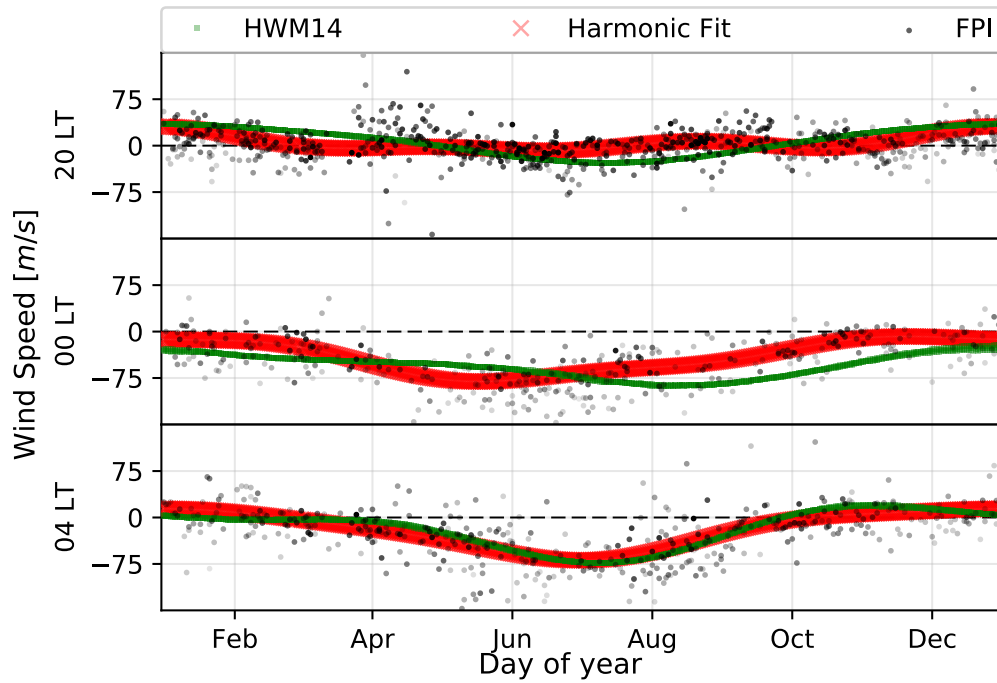


Figure 5.19: Best fit harmonic reconstruction of FPI data and HWM14 for the meridional winds over Morocco at set local times.

5.3.6 Harmonic Analysis Discussion

The most prominent feature seen in both the zonal and meridional measurements is the annual harmonic. This is seen at all the site locations for all local times, except for Brazil and Morocco’s zonal wind at midnight when the three components are nearly equal in value. Ignoring these two exceptions, not only is the annual period always largest in amplitude, but the peak amplitude of the wind is typically centered around DOY 1, ranging from DOY 325 to 60 with a mean of DOY 364, regardless of hemisphere. The similar annual harmonics have the physical explanation that heat flux from the sun is the dominant driver of these thermospheric winds. The 00 LT zonal winds over Brazil, which are not dominated by the annual component, are the only annual component nearly 180 degrees out of phase with all the others. It is curious that the Brazilian and Moroccan midnight zonal winds do not have a dominant annual harmonic when PARI clearly does.

Turning to HWM14, there is fairly good agreement with the annual harmonics found in the FPI data for both zonal and meridional winds. Most amplitudes match closely with the data and the phase matches well, too. However, when the zonal amplitude is smaller than the semiannual amplitude (after midnight in Brazil), HWM14’s non-dominant peak is nearly 180 degrees out of phase. Outside of these cases, HWM14’s annual harmonic has a mean phase of DOY 363, almost exactly matching the data. Regarding the annual amplitudes, not all match well; a worst case example is seen in the overestimate of the 00 LT zonal wind by 38 m/s. We share an example of good agreement in Figure 5.20 with a snapshot of the annual harmonic components taken at 20 LT for the meridional winds. This figure utilizes compass vectors to visually compare the amplitude of the fit (represented by the vector length) and phase of the fit (represented as the angle). DOY has been converted to degrees using the maximum period length in days. Both the amplitude and phase match the data well at this time in all locations except Morocco. Morocco’s amplitude and phase may be off because very little ground-based data over the African sector has gone into HWM. However, given that HWM14 captures the annual harmonics seen in the data across the other two regions, and that the annual harmonic is dominant in most cases, HWM14 can be trusted to capture the large-scale patterns of the winds in regions where FPI data has been included in the model.

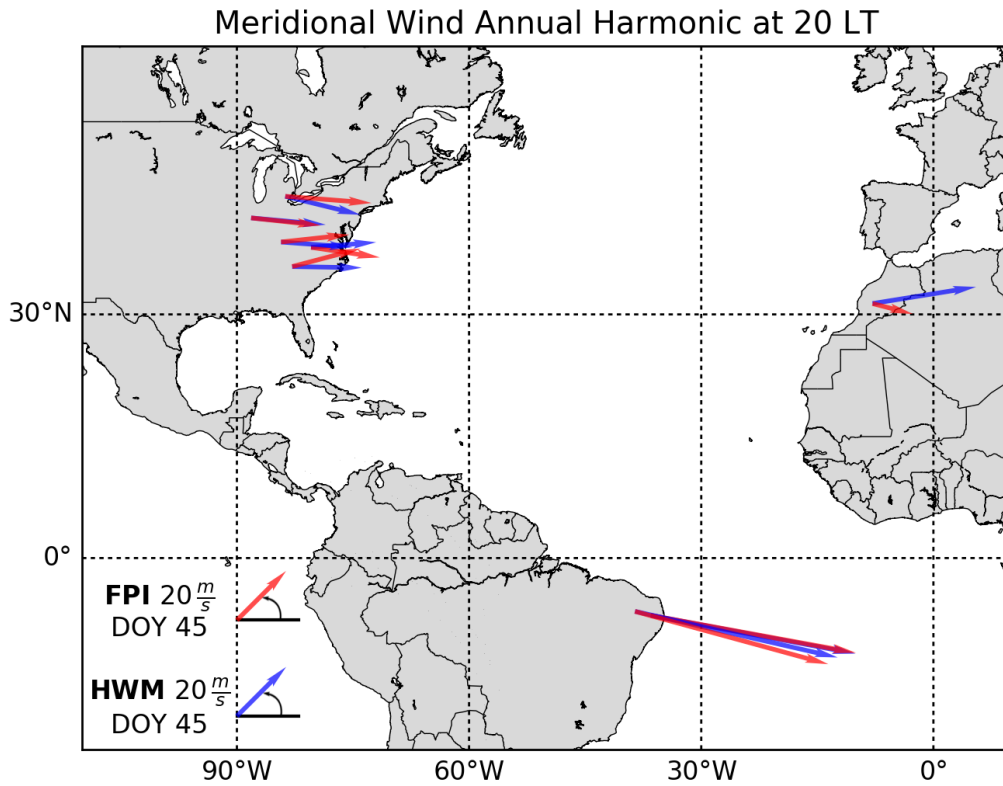


Figure 5.20: Annual harmonic components as vectors for 20 LT meridional winds. Red vectors represent the FPI data while blue vectors represent HWM14. The lengths of the vectors are proportional to the amplitudes and the angles display when the peak amplitude occurs ($365.25 \text{ days} = 360^\circ$).

The semiannual variations of HWM14 show latitudinal variation, where Morocco and PARI have similar amplitude and phase components for both the zonal and meridional winds. However, all three sites have a similar average phase around DOY 78. While this self-agreement is good, the semiannual harmonics found in HWM14 do not share this good agreement with the wind data in general. Figure 5.21 is an example of the semiannual components represented as vectors for the meridional wind at 03 LT. Not only are the amplitudes in disagreement, but there are also significant disagreements between the observations and model in the phase angle. A single HWM fit, while having nearly correct amplitude, is off by nearly 180 degrees phase. Unfortunately, there is no clustering of error by site or local time with either under/overestimating the amplitude or having phase offsets. Since HWM does not capture the semiannual harmonic well, but does capture the annual harmonic, there will be offsets between the modeled wind fits and the measurements. This was observed in the model reconstructed fit at all three sites, in certain local times, where two to three months of overestimation/underestimation exist.

The observations do indicate that the terannual variation can be more significant than the semiannual variation or at least of equal importance. These cases exist without a set pattern, but are present in all three sites at various local times. On average, the phase of the terannual component is DOY 56 with a standard deviation of 36 days. The existence of a significant terannual harmonic in the FPI measurements directly motivates the need for the horizontal wind model to include this in the next iteration.

HWM14 only includes annual and semiannual harmonics by design. We see that this is mostly true, except for the zonal winds of Brazil at 00, 03, and 04 LT, the zonal wind of Morocco at 20 LT, and the meridional wind over PARI at 00 LT. Since the terannual harmonic should not exist in the HWM14 winds, we speculate that this component is due to airglow weighting. In order to prove that the terannual frequencies are in fact an artifact of the airglow-weighted HWM14 winds, we recalculate the HWM14 harmonics assuming a thin emitting layer at 250 km. Without the airglow weighting, no terannual harmonics were found. Semiannual and higher order composition variations are routinely observed in satellite measurements [*Paetzold and Zschörner, 1961; McLandress et al., 1996; Guo et al., 2008; Xu et al., 2009*] and therefore are captured in empirical models of the upper atmosphere. As MSIS and IRI

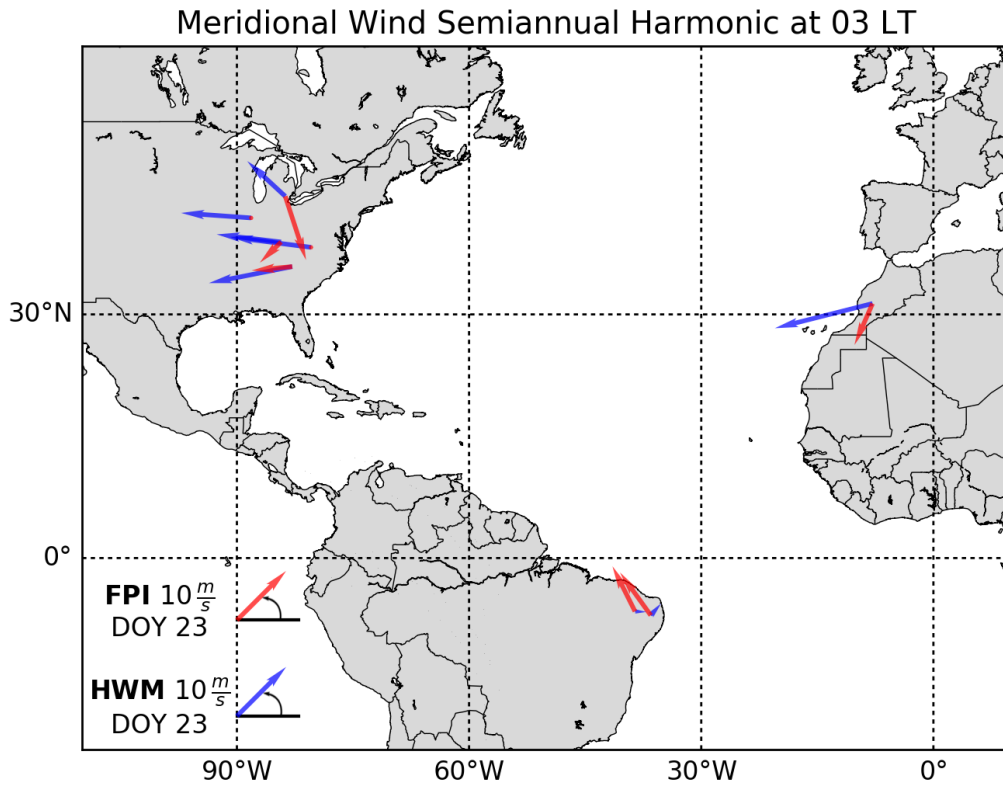


Figure 5.21: Semiannual harmonic components as vectors for 03 LT meridional winds. Red vectors represent the FPI data while blue vectors represent HWM14. The lengths of the vectors are proportional to the amplitudes and the angles display when the peak amplitude occurs (182.625 days = 360°).

are both empirical models, the terannual variation of the constituents would cause a terannual variation in the airglow volume emission rate (Equation 2.6), leading to a terannual weighting of the model winds. However, even with airglow weighting HWM14, the amplitudes of the terannual harmonics are very small (less than 2.5 m/s).

A recent study by *Guo et al.* [2008] used four years of CHAMP measurements to study the annual and intra-annual variations seen in thermospheric densities. While the physical mechanism of this phenomenon is not yet fully understood, several have been proposed to explain the variations. *Mayr and Volland* [1972] speculate that global circulation patterns transport particles and are modified by Joule heating in high latitudes. *Fuller-Rowell et al.* [1996] further stipulate that this interhemispheric flow creates eddies that mix the constituents. *Guo et al.* [2008] confirm that intra-annual variations are seen in all latitude/longitude sectors, but do vary from year-to-year. Additionally, it was noted that the annual harmonic can vary in amplitude by up to 60% year-to-year but the phase is set between DOY 20 and 30. *Guo et al.* [2008] also found that the semiannual component held a constant phase around DOY 100, but the terannual component would vary from DOY 50 to 110.

Comparing the harmonic analysis of our measurements to those made by *Guo et al.* [2008], we see that the phases of the annual and semiannual harmonics are close, but the CHAMP phases lag the average FPI phases by ~ 25 days. As global circulation patterns are theorized to drive the intra-annual density variations, it is possible that the wind flow pattern leads the changes seen in composition by roughly one month. It is also possible that this phase difference is caused by the large standard deviations seen in the phases of the harmonic components. The Monte Carlo simulations do show a 20 day uncertainty caused by random noise simulated in our measurements. This spread is enough to explain the phase difference for both the annual and semiannual components. However the average standard deviations in phase are measured to be quite large: 26 days for the annual component and 54 days for the semiannual component. This large variance disagrees with the nearly constant phase found in the CHAMP-measured annual and semiannual variations each year and could indicate that the day-to-day variability of the measurements does not constrain the Lomb-Scargle technique. In Section 4.2, we found day-to-day variation to be greater than 20 m/s, which means

the harmonic routine has one month of phase uncertainty in the amplitude fit alone. As the 30 days of uncertainty are on the order of the measured phase standard deviations found by the Lomb-Scargle analysis, daily variability could be causing the uncertainty. Interestingly, HWM14's average annual phase, DOY 363, leads the CHAMP results by around 20 days, but HWM's average semiannual phase, DOY 120, lags the CHAMP semiannual component by 20 days.

Unlike the semiannual component, the terannual component measured by *Guo et al.* [2008] shows yearly phase variation. The average terannual phase measured by the FPIs is DOY 56, which is within the range measured from CHAMP. Assuming that the FPI measurements lead the densities by the same amount predicted for the annual and semiannual components, the FPI estimate would be in the center of the range. As the standard deviation of the terannual phase is large too, it is uncertain if this is due to day-to-day measurement variability or actual phase variation. Unfortunately, the data collected is not sampled densely enough to validate the year-to-year variations, such as the yearly amplitude fluctuation or the asymmetry of the semiannual component, seen in *Guo et al.* [2008]. By averaging the data over multiple years, we have blurred any amplitude or phase shifts that exist. More data would be needed to study these intra-annual variations. Collecting a longer time series of data can only improve the accuracy of this Lomb-Scargle analysis, as the winds are quite variable day-to-day. Nevertheless, with the shortest time series of data being over three years in length (coming from Morocco), the terannual harmonic is a repeatable feature that exists at all locations at certain local times.

5.4 Summary

We summarize the key points learned from using our neutral wind data to validate the horizontal wind model:

- Our neutral wind measurements were vital in identifying an issue with HWM07 over Brazil. The FPI measurements also were ingested by the model to improve the next iteration, HWM14.
- In order to properly compare HWM with our LOS FPI observations,

the model requires airglow-weighting. Using IRI and MSIS, one can estimate the vertical airglow profile to help weight the relative contribution of wind from each altitude. It was shown that this method is superior to assuming a thin emitting layer at 250 km; however, it does require accurate empirical models.

- We utilize a Lomb-Scargle harmonic analysis to find the amplitude and phase of the annual, semiannual, and terannual components of the winds at set local times, in order to better compare with how HWM14 is created. These components are then used to reconstruct the best-fit sinusoid for the data and the model.
- The annual harmonic is usually the dominant component of the neutral winds, driven by solar heat flux. HWM14 does a good job capturing this component in both amplitude and phase.
- The semiannual harmonic seen in the data is not well captured by the model. Further ingestion of FPI observations to HWM would improve the model fits, especially with data from the African sector.
- The terannual harmonic is present in a majority of the sites at various local times. The harmonic fits of the data, using this component, always have a better residual than the model fits. As HWM14 does not include a terannual component, our results show promise of further improving HWM with the inclusion of the terannual harmonic.
- Comparisons of harmonic findings with other studies have shown that more data is required to accurately estimate the best-fit waveforms for the neutral wind data. Additional measurements would enable higher order harmonics to be observed and potentially enable the study of year-to-year wind variations.

CHAPTER 6

UTILIZING JOINT FPI AND ASI OBSERVATIONS TO ASSESS THE STORM-TIME DISTURBANCE DYNAMO

This chapter utilizes derived neutral wind data along with airglow imaging data during geomagnetic storms to analyze thermosphere/ionosphere storm-time coupling. We present two methods of bubble drift and neutral wind comparisons. The analysis is used to further understand the disturbance dynamo theory and the dynamics of low-latitude plasma irregularities.

6.1 Equatorial Ionospheric Irregularities

Plasma irregularities are common in the equatorial and low-latitude ionosphere [Burke, 2004]. A primary feature of these irregularities is an electron depletion region caused by the Rayleigh-Taylor instability [Dungey, 1956]. Analogous to the unstable system of a denser fluid atop a lighter one, the nighttime ionosphere consists of a dense conductive layer of electrons on top of a bottomside F-layer with a smaller density due to recombination. When a perturbation, such as an electric field or zonal neutral wind, destabilizes the system, it causes rapid growth of a depletion region [Kudeki *et al.*, 2007]. Once formed, these plasma regions drift eastward with the background plasma following F-region dynamo theory [Rishbeth, 1971; Heelis *et al.*, 1974; Fejer, 1981; Sobral *et al.*, 2011].

The names for this phenomenon vary depending on how it is captured by different instruments. For example, small-scale fluctuations within the depletion region cause radio signals to scatter, creating a spread in the frequency of the returned signal; hence it is referred to as “spread-F” in radar studies. Observed from space, they are called “bite-outs” or “depletions”. If the same irregularity was captured by an optical imager, one would see a dark depleted region which looks like a “bubble” or “plume”. Thus, the depletions in imaging literature are often called equatorial plasma bubbles

(EPB). The depletion in airglow intensity occurs because the redline volume emission rate is dependent on electron density (Section 2.2), and a loss of electrons effectively eliminates the production of excited oxygen.

EPBs tend to form seasonally when the sunset terminator crosses a magnetic flux tube simultaneously in both hemispheres [*Tsunoda*, 1985; *Burke*, 2004]. This time period normally coincides with the equinoxes, but for some locations this is not the case due to the geometry between the solar terminator and the geomagnetic equator. The vertical growth of the EPB is over the geomagnetic equator, but the electric fields map down along magnetic field lines due to the high along- \mathbf{B} directed conductivity. While most equatorial plasma bubbles occur within 20° of the magnetic equator, they have been observed in the mid-latitude regions as high as 40° [*Burke*, 2004]. Over the years, many researchers have studied the seasonality, velocities, and geographic extent of these bubbles, and much work has been done using ground-based imagers [*Mendillo and Baumgardner*, 1982; *Fagundes et al.*, 1997; *Taylor et al.*, 1997; *Kelley and Makela*, 2003; *Martinis*, 2003; *Pimenta et al.*, 2003; *Makela et al.*, 2004; *Yao and Makela*, 2007].

To investigate these phenomena, a redline all-sky imager (ASI) collects a full two-dimensional spatial map of airglow, capturing the motion of bubble events over the night. Under the assumption of the bubbles drifting with the background plasma, a plasma drift can be estimated by tracking the motion of the bubbles over time [*McClure et al.*, 1977]. Additionally, an FPI can be collocated with the ASI. By observing the same region with an FPI, comparison between the FPI-derived winds and the ASI-derived drifts can be made and used to understand coupling between the thermosphere and ionosphere.

Chapagain et al. [2012, 2013] used ASI and FPI data from the Peruvian and Brazilian sectors and found that plasma drifts closely match the horizontal neutral winds perpendicular to \mathbf{B} after fossilization. The Peruvian FPI was used because it is located at the magnetic equator, collocated with Jicamarca's incoherent scatter radar. The finding of agreement between measured plasma drifts and FPI derived winds supported the understandings that the F-region dynamo is fully activated [*Biondi et al.*, 1988; *Basu et al.*, 1996; *Valladares et al.*, 2002], although *Chapagain et al.* [2012, 2013] note variation due to day-to-day variability in the winds. It is worth mentioning that *Chapagain et al.* [2012, 2013] only made comparisons in geomagnetically

quiet periods. No work has been attempted to show similar comparisons during storm-times when disturbance dynamo activation may be different than the quiet-time F-region dynamo. Past studies [Taylor *et al.*, 1997; Abdu *et al.*, 2003; Santos *et al.*, 2016b] have shown that EPB drift velocities can slow down, stall, and even reverse direction during geomagnetic storm periods. However, these previous studies lacked coincident measurements of the neutral drivers of the drifts, and so could not conclude why the EPB drifts changed as they did. Here, we present several results in which we have simultaneous observations of EPBs and neutral winds, and investigate the driver of EPB motion during storms.

6.2 Equatorial Plasma Bubble Analyses

In 2013, a pairing of all-sky imager with a collocated FPI was installed in Oukämeden, Morocco. While Morocco is not a low-latitude site, the ASI is still able to capture EPBs in its southern field-of-view (FOV). Figure 6.1 shows how the Moroccan ASI views a plasma bubble crossing the field-of-view.

In order to analyze the bubble drift velocities and compare them with the measured neutral winds, we have created two automated methods. The first is a quantitative cross-correlation technique designed to track the bubble in a series of images and compare it to the neutral winds. The second is a qualitative method overlaying neutral particle motion vectors on a keogram, useful for visually assessing the relationship between the drift and background thermospheric winds.

6.2.1 Method 1: Cross-Correlation Analysis

The first method to be described is the quantitative cross-correlation technique. As a first step, each airglow image is median filtered to remove both stars and noise. The pixels are then projected onto geomagnetic coordinates at the redline emission peak altitude (assumed to be 250 km). We note that this altitude is likely not correct at all times (see discussion in Section 5.2), but is used as a simplifying assumption for this analysis. This simplification can create drift errors up to $\pm 12\%$, as the emission altitude estimated from

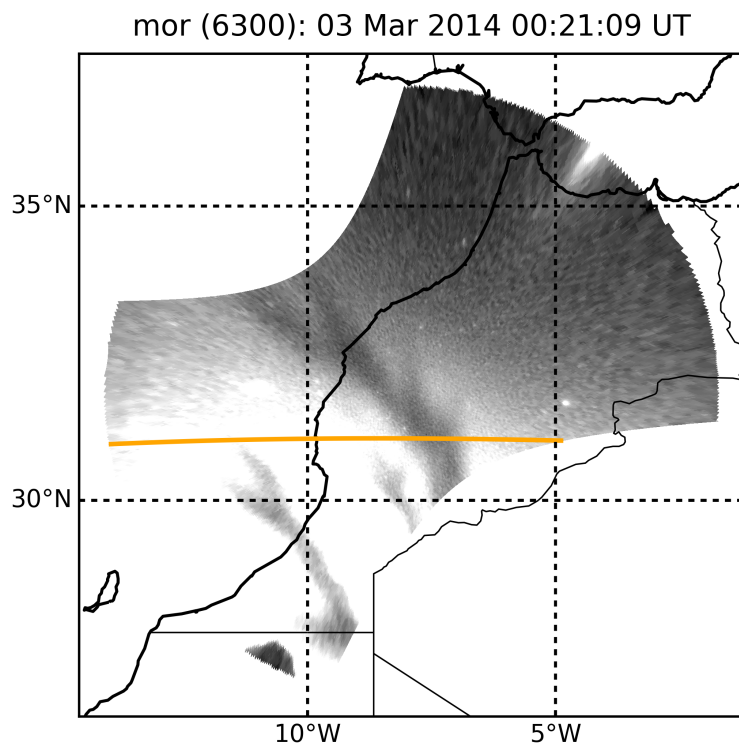


Figure 6.1: Example ASI image capturing an equatorial plasma bubble over Morocco on March 2, 2014. The line shows the constant geomagnetic latitude used to make the keogram in Figure 6.2.

models can fluctuate by ± 30 km in a night.

Next, we take three separate east-west cuts of the airglow intensity at three separate magnetic latitudes. The highest of these latitudes is equal to the mean pierce-point magnetic latitude from the east and west FPI look directions. The other cuts are taken below this latitude in 1° increments, as the EPBs are primarily located in the equatorward half of the image. For the Oukaimeden site, the magnetic latitude slices are taken at 42.8°N , 41.8°N , and 40.8°N . Each slice is interpolated onto a uniformly spaced grid with a sub-pixel resolution of 1 km. After generating these uniformly spaced cuts from each image, cross-correlations are taken. The cross-correlation is defined as:

$$r[l] = \sum_{k=-x/3}^{x/3} X[k+l]Y[k]. \quad (6.1)$$

Here, r is the cross-correlation of vectors X and Y , x is the length of X which is also the length of Y , and the lag is l . We have defined the limits of the summation so that we only use the center $2/3$ of the image for the correlation. We are left with a lag search space in the range of $-x/6$ to $x/6$. The lag corresponding to the highest cross-correlation is used to calculate the velocity. Drifts are calculated as:

$$V \left[\frac{t_{m+5} + t_m}{2} \right] = \frac{ld}{t_{m+5} - t_m}. \quad (6.2)$$

A series of velocities, V , in m/s, are found at the time in between two images, taken at time t_{5+m} and t_m , where m is the exposure number, l is the lag, and d is the grid resolution set by the uniform spacing of the interpolation. We chose a separation of five images in order to limit our velocity uncertainty to ± 1 m/s. This is done because the timing is the only free parameter to adjust the uncertainty; the maximum lag is set by x which is set by the field-of-view of the imager. As we use a lens with an FOV extending to 20° above the horizon and a set exposure time of 90 s, the maximum estimates of drift velocity are limited to ± 264 m/s. This is well within physical wind speeds observed by the FPI and expected drift velocities of EPBs. The velocities estimated from the three latitude slices are averaged together to reduce uncertainties caused by bubble deformation or tilt. Once the EPB drift is calculated, it can be quantitatively compared to the FPI-measured

magnetic zonal winds.

Typically, one must project the zonal and meridional winds onto the horizontal perpendicular- \mathbf{B} direction to ensure a more accurate comparison with the drifts. The magnetic field lines over Morocco have a very small declination (the field lines are nearly perfectly oriented north-south), such that we can assume the zonal wind is the perpendicular- \mathbf{B} horizontal wind. This simplification is important as it reduces the constraints on available wind measurements. Without needing to rotate the horizontal wind vector into the geomagnetic coordinate frame, only a single zonal measurement is needed, instead of both a meridional and zonal measurement for creating a horizontal wind vector. Not having to combine wind measurements from the different FPI look directions reduces uncertainties in the wind speed and also improves the time resolution of the winds.

There are some potential issues with this automated technique. The main problem is that we are tracking an amplitude shift in the signal. If a very bright object (like a cloud, star, or general brightness gradient that was not completely removed by median filtering) passes through to a latitude slice, the cross-correlation may return a lag that tracks this bright object instead of the desired bubble. Secondly, since no pattern recognition is performed, the cross-correlation method will return an “estimated” drift regardless of whether a bubble is present or not. This problem demands that the user know the times when the bubble is in frame to interpret the results properly. Another concern is the effect of the bubble changing shape or rotating while passing through the latitudinal slice. While three slices are averaged together in order to reduce the effects of rotation, this neither guarantees an improvement nor corrects for bubble deformation or fracturing. Finally, the technique only uses the center of the image for correlations, so bubbles on the edge of the CCD will not be found even though they are visible in the raw image.

6.2.2 Method 2: Keogram to Wind Vector Comparison

The second method is a qualitative visual approach using keograms and wind vectors. A keogram is a image created by taking slices of an image and stacking them together in order to determine motion. For example, one can

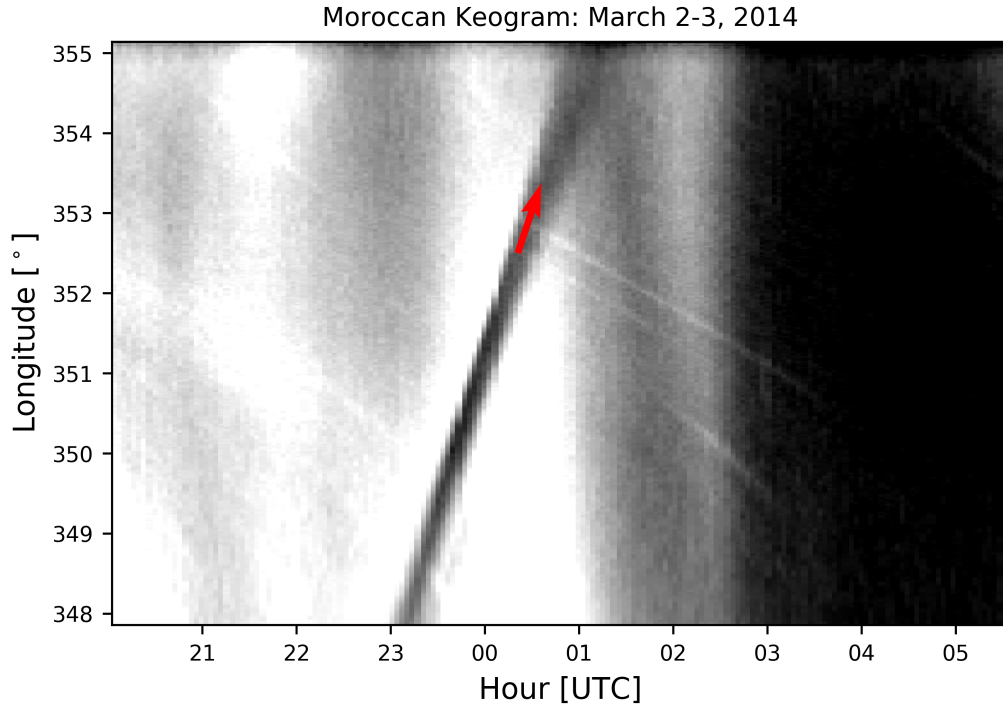


Figure 6.2: Example keogram from the night of March 2, 2014. The vector here matches the slope of the bubble, estimating the zonal motion of the plasma bubble from Figure 6.1.

take a constant latitude cut from each image (marked in orange in Figure 6.1) and place them side-by-side to form a range-time plot. Thus, in EPB analysis, the observed slope of the bubble gives an estimate of the speed. The keogram for the data collected on the night shown in Figure 6.1, created along the cut defined by the orange line, is shown in Figure 6.2. The arrow in Figure 6.2 highlights the slope defined by the bubble motion and can be used to estimate the speed.

The first steps of the technique are identical to the cross-correlation method: median filter the airglow image and project the pixels to geomagnetic coordinates on a 250 km altitude surface. Then, take a single east-west slice of airglow intensity at a fixed magnetic latitude, ideally one that intersects the east and/or west look direction pierce point. Taking these same cuts from each image over the night, we create a keogram or a longitude-vs.-time plot to show the east-west (in the perpendicular- \mathbf{B} direction) bubble motion.

The next step requires the geomagnetic zonal wind from the FPI observations. In order to intuitively plot the wind velocities on top of the keogram,

motion vectors are used. A motion vector shows the path an object takes over a set amount of time, t . In our case, if a test particle were initially placed at the tail end of the vector, the winds would carry it to the tip of the vector over time t . As an example, consider the wind vector in Figure 6.2. The time length (x-axis) of the vector is 10 minutes and the distance (y-axis) it covers is 0.58° . This means that the wind particle will travel 0.58° eastward in 10 min or equivalently has a speed of 95 m/s. The vector has a positive slope indicating that the wind is directed eastward. If the vector had a negative slope, the wind would be westward. If it had no slope, there would be no zonal wind component. This assumes a constant neutral wind over the set time period and that collisions do not change the particle's trajectory. We also assume that the winds across the sky are uniform. It is known that gradients do exist, but are generally small over the 10° longitude seen by the ASI [Emmert *et al.*, 2003]. Thus, the average zonal wind is representative of the instantaneous wind field in our FOV.

If the dynamo is in full effect, the bubbles will drift in the same direction and with the same speed as the background winds. In the keogram technique, this observation can be made by qualitatively comparing the slope/shape of the EPB with the wind motion vector.

6.3 Comparison of Bubble Drifts and Neutral Winds

We utilize these two methods to analyze bubble drifts and neutral winds during storm times. Given the infrequent occurrence of bubbles, the randomness of cloud cover, and an overall lack of storm-time data, there are very few cases of coincident FPI and ASI observations in geomagnetically active conditions. Here, we present a few examples from the Oukaïmeden Observatory instruments. However, in order to show that the storm-time response analysis is valid, it is important to first demonstrate that the methods succeed in analyzing the F-region dynamo during nominal quiet-time cases.

6.3.1 Method Validation During Quiet-Time Events

The two quiet-time EPBs considered here are from early March of 2014. Both occurred during clear skies for the ASI to view bubbles, and the FPI

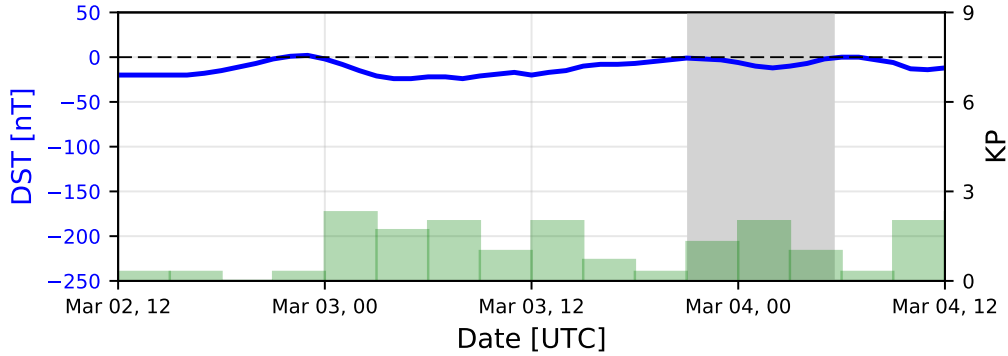


Figure 6.3: DST and K_P values for the nights preceding and nights of March 1, 2014 and March 3, 2014. The gray area indicates when the ASI was operational during these nights.

to measure the zonal neutral winds, with a very high cadence. The first event, March 1, 2014, is characterized by the DST and K_P indices shown in Figure 6.3, indicating relatively quiet conditions. The winds agree with this assertion, as they are representative of the monthly mean quiet-time winds (e.g. Figure 4.4). Figure 6.4 depicts the measured zonal winds from the east (red) and west (magenta) look directions with the measurement uncertainties represented by the error bars. It also includes the 2-sigma variation of the quiet-time zonal winds for the month of March 2014 (green shaded region). It is worth noting that gradients are seen in the zonal winds at more than one point in the night, which could lead to small discrepancies when using the keogram method.

Using the first method (cross-correlation), the zonal drifts are calculated and displayed as blue dots on top of these neutral winds. The ASI first detects plasma bubbles around 21 UTC (manually observed in the images with no filtering), but they do not fully develop until 22 UTC. The bubbles are present until 01 UTC the next day. Figure 6.5 gives a time lapse of airglow images projected to 250 km, capturing the series of bubbles. During this time, Figure 6.4 shows that the drift speed and wind speed are in agreement, typically within the west look direction measurement uncertainties of ± 5 m/s. Since the neutral winds correlate with the estimated drifts, we can state that the dynamo is activated.

Figure 6.6 shows this same data using the keogram method. The keogram captures five depletions crossing eastward with a fairly uniform velocity. The

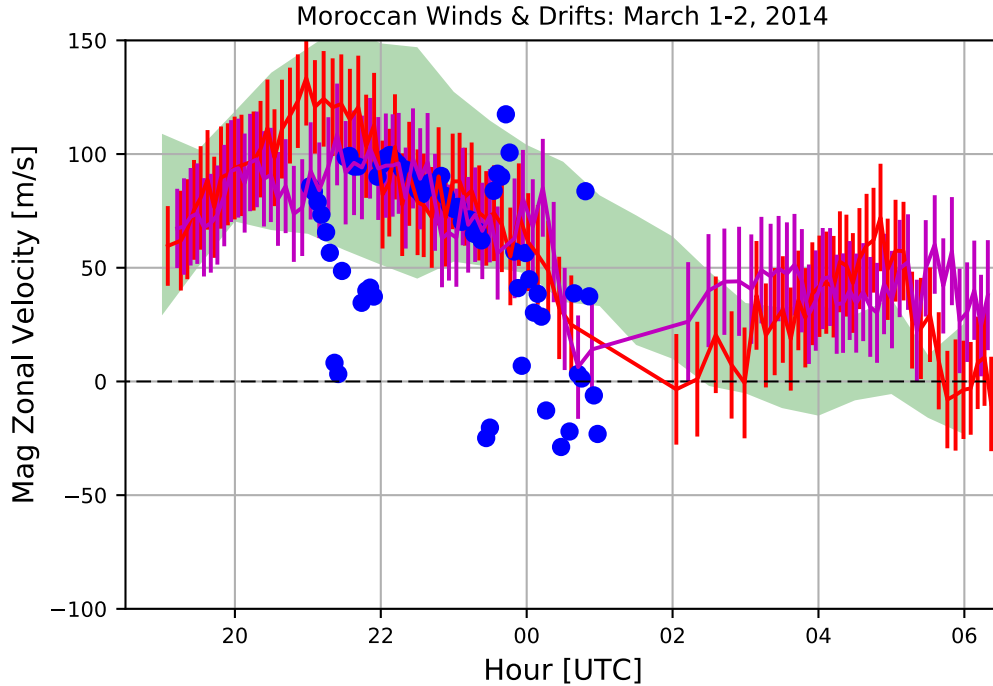


Figure 6.4: Estimated plasma drifts and neutral winds for the night of March 1, 2014. The plasma drift estimates from the cross-correlation method are marked as blue dots. The zonal neutral winds are plotted from the east (red) and west (magenta) look directions with error bars for the measurement uncertainties. The green shaded region displays typical range of quiet-time zonal neutral winds for March 2014.

winds align with the general motion of the EPBs; however, the drifts are slightly faster than the wind vectors. This could be partially due to averaging the zonal winds, especially around 21 UTC when there is a gradient present. Regardless, the agreement shows that the dynamo is in effect during the night.

The second event occurs two days later on March 3, 2014. This night is also geomagnetically quiet. Figure 6.3 corroborates this by showing the DST and K_P values for the night. Bubbles were already present when data were first measured at 21 UTC and continued until 01 UTC. The FPI obtained zonal winds until 02 UTC, when the instrument unexpectedly stopped taking data. This overlapped with the time period when the ASI observed four bubbles passing through the field of view. Figure 6.7 presents the neutral winds and estimated drifts. Between 21 UTC and 01 UTC, the neutral winds were in fairly good agreement with the drift velocity estimations; however, the

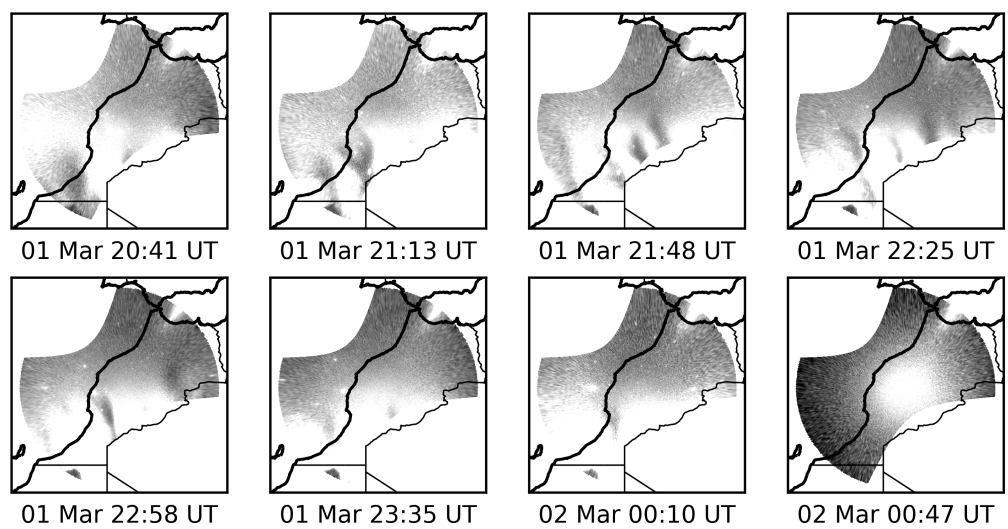


Figure 6.5: Time lapse of bubbles on the night of March 1, 2014. The airglow images are projected to an emission altitude of 250 km.

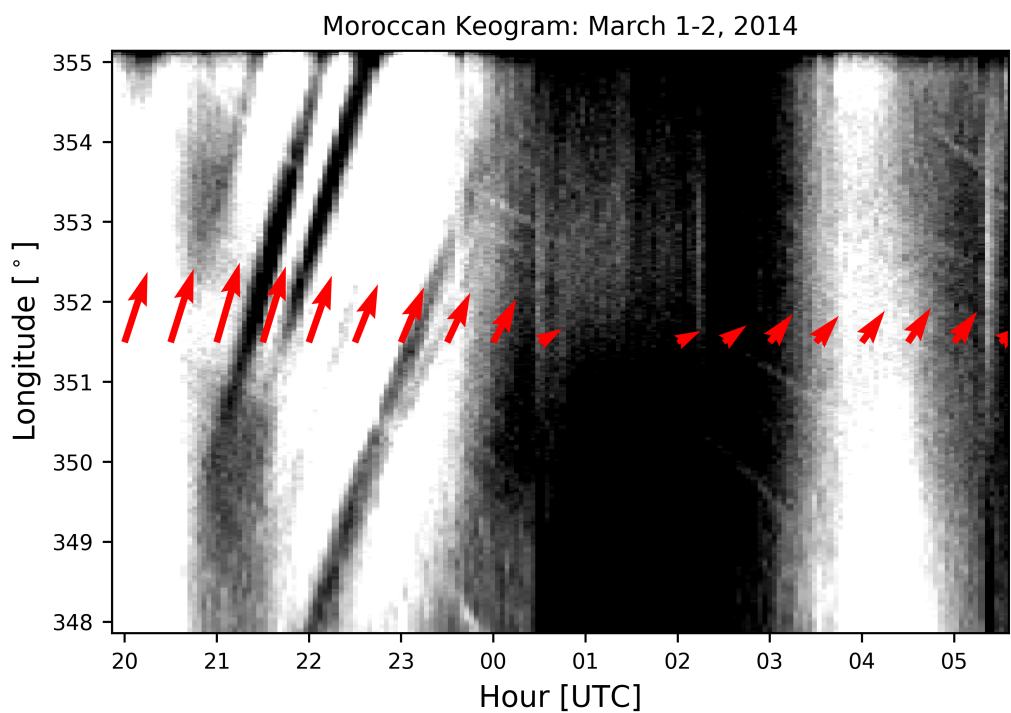


Figure 6.6: Keogram with an overlay of zonal neutral wind vectors from the night of March 1, 2014. The red arrows are motion vectors that describe how a neutral particle would move if the winds were constant across the field of view for that time step.

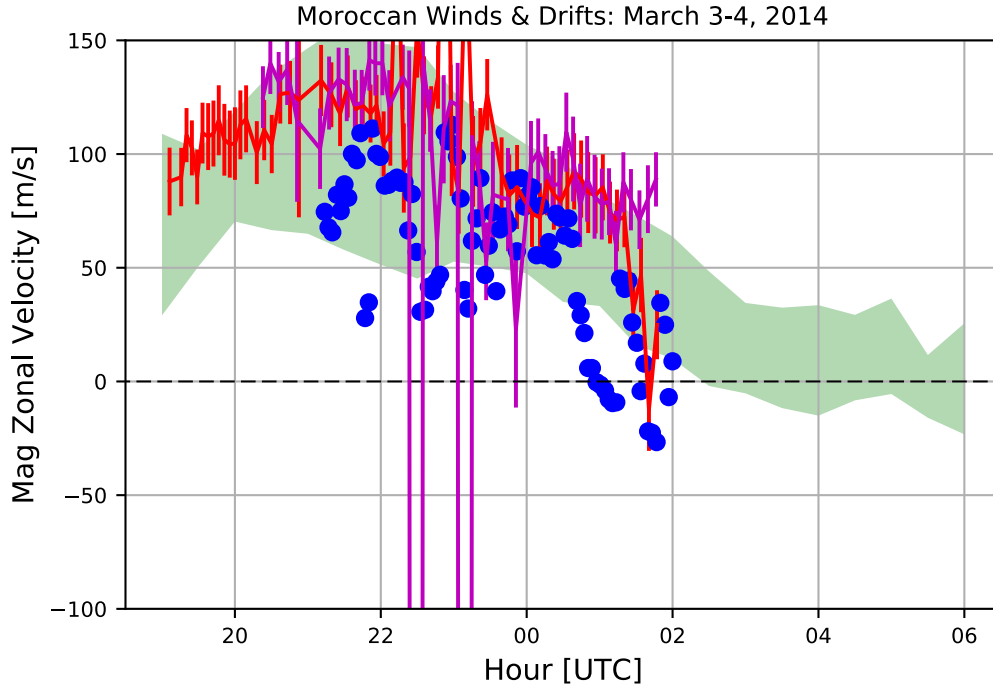


Figure 6.7: Estimated plasma drifts and neutral winds for the night of March 3, 2014. The plasma drift estimates from the cross-correlation method are marked as blue dots. The zonal neutral winds are plotted from the east (red) and west (magenta) look directions with error bars for the measurement uncertainties. The green shaded region displays typical range of quiet-time zonal neutral winds for March 2014.

drifts are on average 30 m/s slower than the winds. This larger discrepancy appears to be due to camera rotation: Figure 6.8 shows that near 23 UTC, the bubbles are on the camera edges. The second technique, which is able to use the entire magnetic slice from edge to edge, shows better agreement between drifts and winds. Figure 6.9 shows that here, too, the dynamo is fully activated.

Both examples show that the two techniques presented in Section 6.2 produce comparable results, and can both successfully be used to compare the wind and drift speeds. The keogram technique, while lacking quantitative results, does show better agreement than the correlation method as it is not affected by noise or edge effects. While many other examples of quiet-time bubbles exist, this sample is sufficient to demonstrate that the techniques produce reasonable results. We now turn to the applicability of both methods during storm-time events.

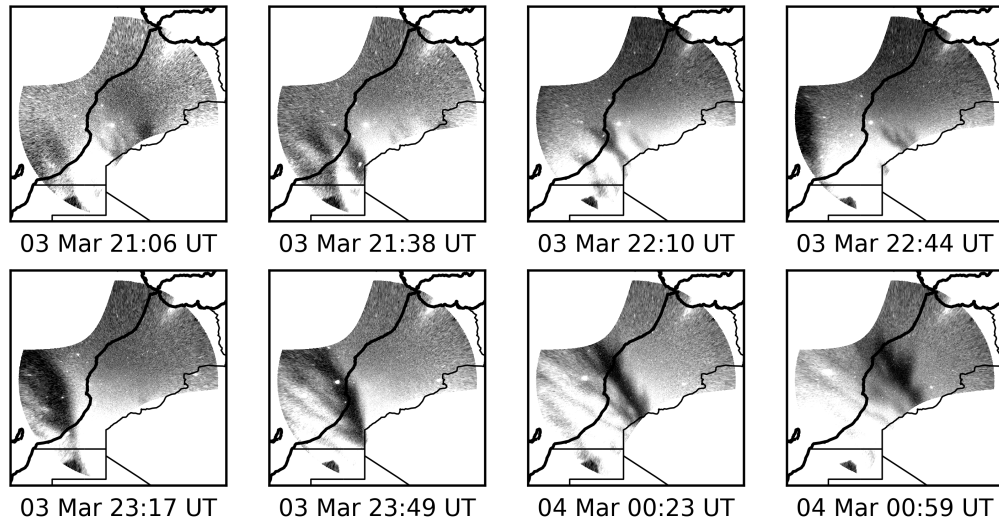


Figure 6.8: Time lapse of bubbles on the night of March 3, 2014. The airglow images are projected to an emission altitude of 250 km.

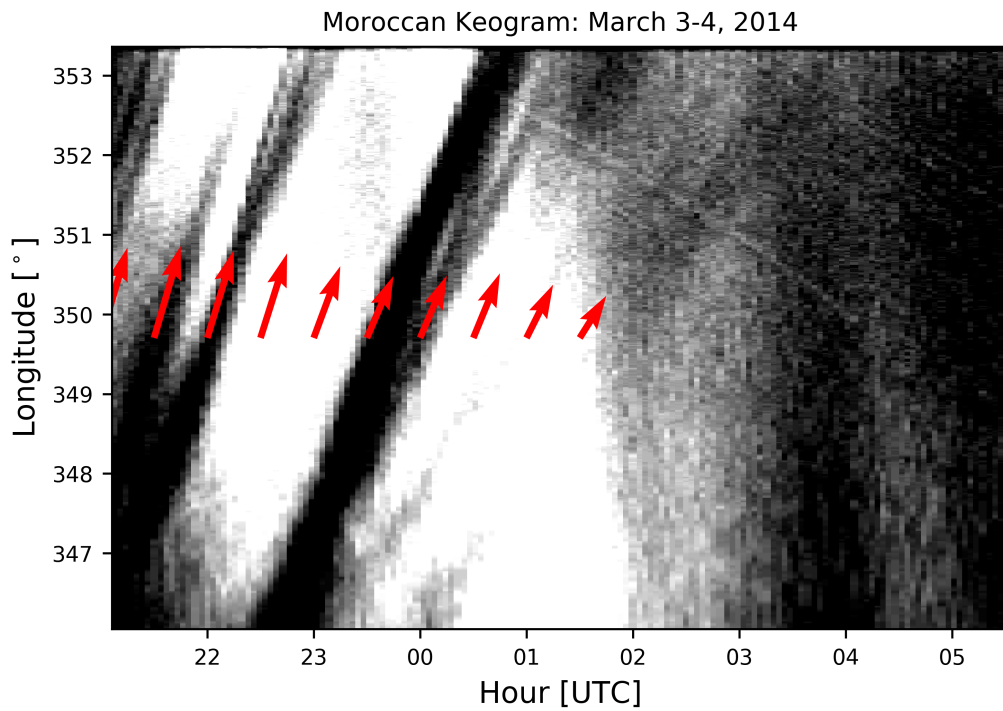


Figure 6.9: Keogram with an overlay of zonal neutral wind vectors from the night of March 3, 2014. The red arrows are motion vectors that describe how a neutral particle would move if the winds were constant across the field of view for that time step.

6.3.2 Method Implementation During Storm-Time Events

The minor storm on August 23, 2016, was characterized by a drop in DST, reaching a low of -74 nT, with sustained K_P values above 4 over the local nighttime, as shown in Figure 6.10. Three bubbles developed immediately after this storm onset, beginning at 20 UTC and lasting until they disappeared in the images around 23 UTC. The bubbles grow, travel slightly westward, and then remain stationary. It is worth noting the bubble tilt changes during this process. Proof of the tilted and stalled bubbles can be seen in the time lapse shown in Figure 6.12. Figure 6.11 shows that, before 21 UTC, the measured neutral winds are westward and outside the 2-sigma nominal quiet-time monthly average for August 2016. The winds again shift westward after 00 UTC. During storms, a westward turning of the zonal winds is typically seen in mid-latitude locations [*Hernandez and Roble, 1976b; Emmert et al., 2002; Makela et al., 2014*] and is evident on this night.

The cross-correlation technique (Figure 6.11) also estimates westward drifts. Unlike the neutral winds, the estimated drift speeds are always westward, and, at times, significantly faster than the neutral winds; on average, the drifts are 20 m/s more westward than the neutrals. This westward bias could be due to contamination from the Milky Way band that crosses the field of view this night. The Milky Way is too bright and unlocalized to remove with simple filtering techniques. Due to the Earth's rotation, the Milky Way becomes a westward propagating feature that is spatially large enough to effect the cross-correlation's returned lag. Another complicating factor is the tilt of the EPB due to vertical sheer in the drifts [*Makela and Kelley, 2003*]. Since the technique only correlates over one-dimensional slices, two-dimensional features, such as curl or tilt, are not distinct from bulk motion. Thus, if any tilt occurs, it could bias the bubble drift speed estimated through cross-correlation. Unfortunately, without any instrumentation near the equator where the bubble forms, it is impossible to test whether any vertical sheer exists.

The keogram technique agrees with these findings and shows good correlation between the winds and drifts in Figure 6.13. The center bubble (in Figure 6.12) is actually the solid band seen around 351° W longitude, indicating that the depletion did not move. The neutral winds agree well with this, showing no motion during 20 UTC and only slightly eastward flow during 21

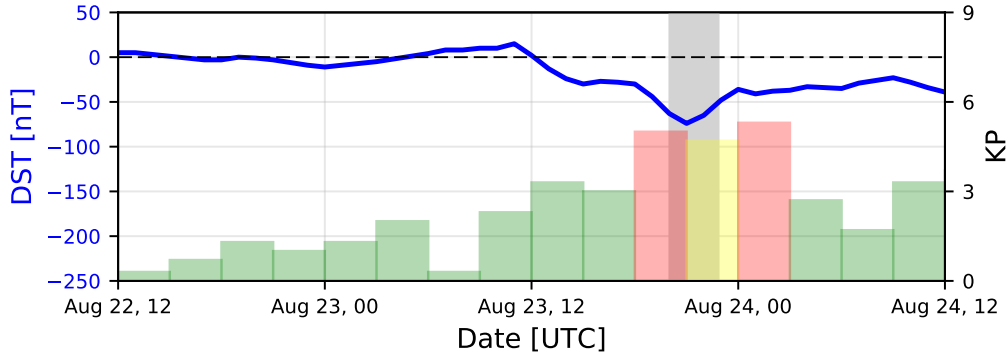


Figure 6.10: DST and K_P values for the night preceding and night of August 23, 2016. The gray area indicates when the ASI was operational during this night.

UTC. This agreement indicates that, much like in geomagnetically quiet periods, the neutral wind plays the largest role in controlling the bubble motion and that the dynamo quickly initiates.

A second event was captured on February 27, 2014, when DST dropped to -94 nT. The geomagnetic storm onset occurred right at local dusk for Morocco, with K_P reaching 5 for six consecutive hours (seen in Figure 6.14). This storm caused a strong westward turning of the neutral winds from 21 to 04 UTC. Figure 6.15 shows that, around local midnight, the neutral winds were over 50 m/s more westward than the 2-sigma quiet-time average. The zonal winds return eastward after 03 UTC, but their pattern is far from typical. Also peculiar is the difference measured between the east and west look directions; from 22 to 01 UTC the east measurement is roughly 25 m/s more westward than the western look direction. This large gradient may indicate storm-time shears in the horizontal winds.

What is most interesting, however, is how well the estimated drifts match the zonal winds measured from the west look direction; there is less than a 5 m/s difference between them, on average, between 01 and 04 UTC. The drifts are more westward than the neutrals from 20 to 22 UTC when the bubble is near the edge of the CCD. From 22 to 04 UTC, the plasma drifts are nearly always within the uncertainties measured from the west look direction. This unique wind and drift pattern is also apparent in the keogram in Figure 6.16. While the airglow becomes extremely dim for a large portion of the night, the transition from westward to eastward winds is well captured in

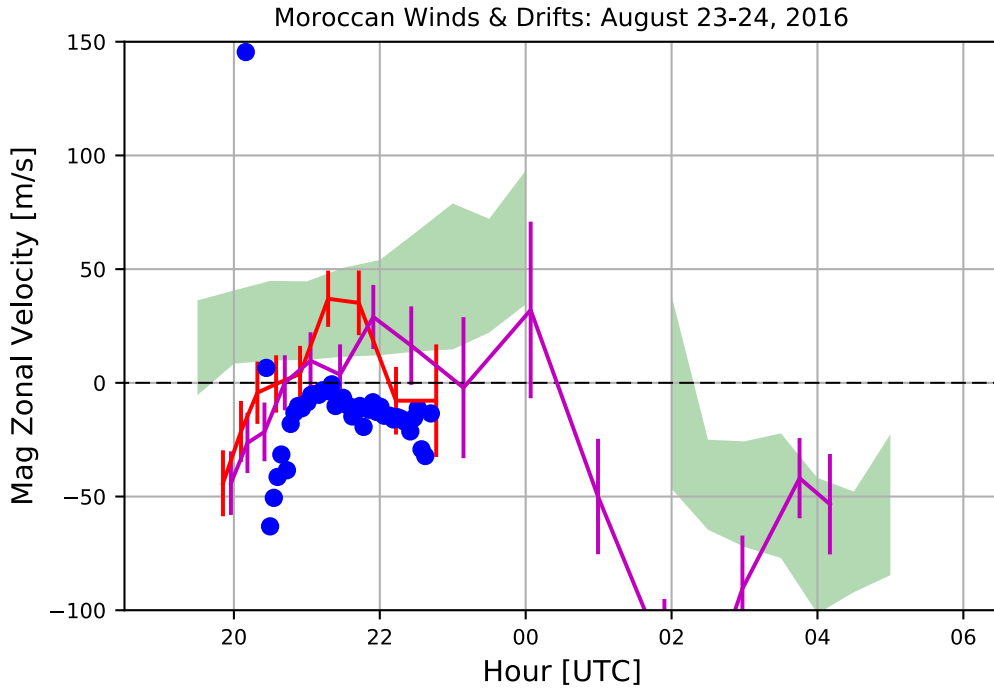


Figure 6.11: Estimated plasma drifts and neutral winds for the night of August 23, 2016. The plasma drift estimates from the cross-correlation method are marked as blue dots. The zonal neutral winds are plotted from the east (red) and west (magenta) look directions with error bars for the measurement uncertainties. The green shaded region displays typical range of quiet-time zonal neutral winds for August 2016.

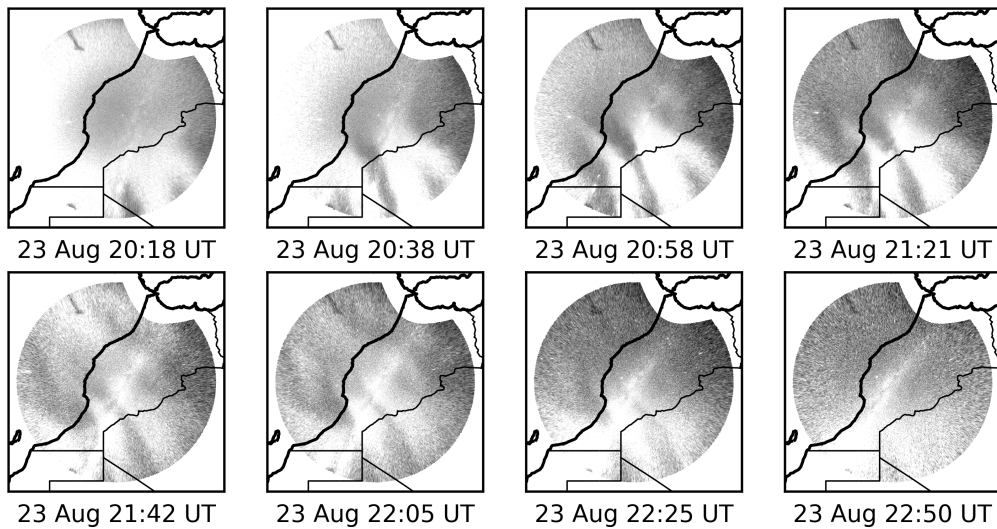


Figure 6.12: Time lapse of bubbles on the night of August 23, 2016. The airglow images are projected to an emission altitude of 250 km.

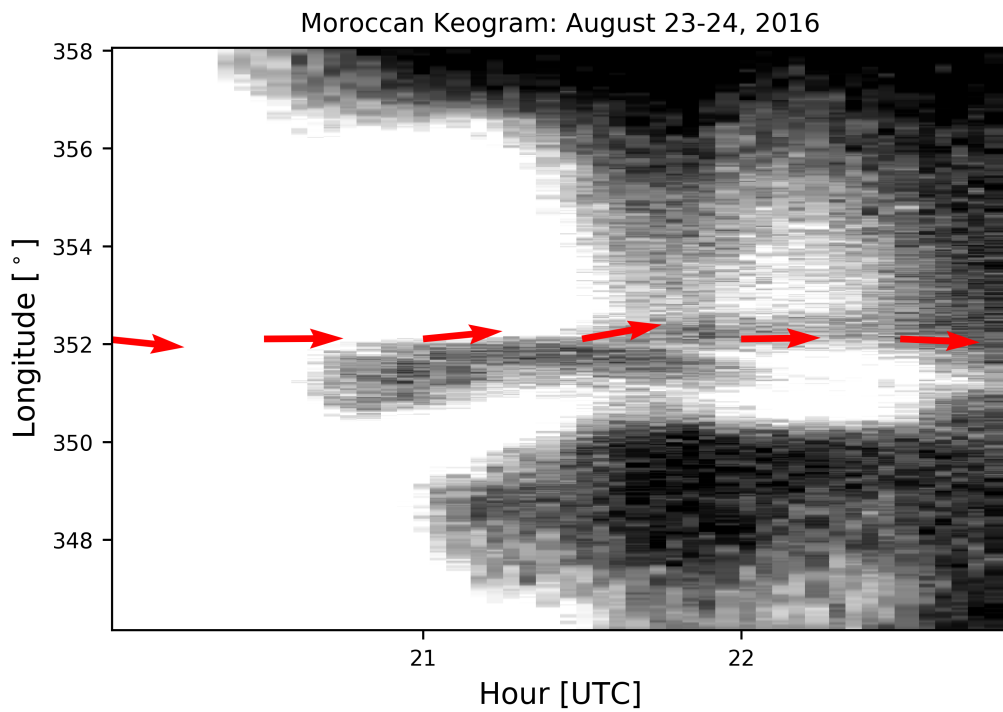


Figure 6.13: Keogram with an overlay of zonal neutral wind vectors from the night of August 23, 2016. The red arrows are motion vectors that describe how a neutral particle would move if the winds were constant across the field of view for that time step.

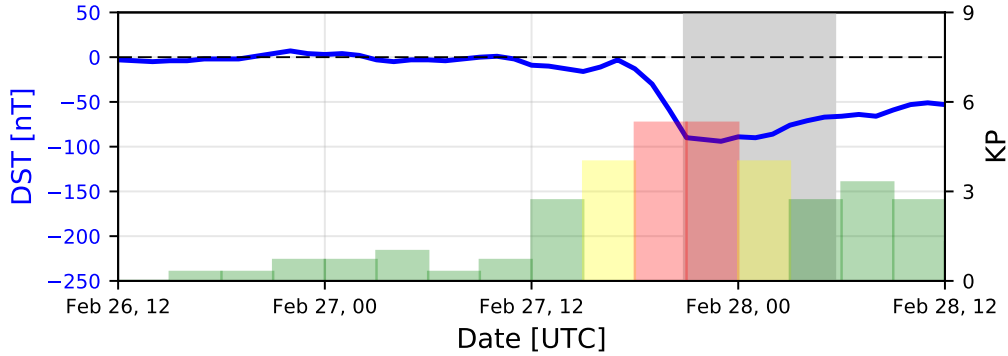


Figure 6.14: DST and K_P values for the night preceding and night of February 27, 2014. The gray area indicates when the ASI was operational during this night.

the “U” shaped plasma bubble pattern centered at 03 UTC. This transition is also captured in a time lapse of the images in Figure 6.17. Note that the measured wind vectors also mimic this feature. This estimate provides further evidence that even during storm periods, the neutral winds control bubble motion through the dynamo.

6.3.3 Comments on Secondary Instabilities

Optical observations of equatorial plasma bubbles have shown that secondary instabilities can form on a bubble’s western wall. These secondary plumes were theorized to be driven by an eastward neutral wind blowing across a steep electron density gradient [Tsunoda, 1983]. This would leave the eastern wall unchanged. The bubbles over Morocco do develop secondary instabilities on their western walls during quiet times, which can be seen in Figure 6.8.

While a majority of secondary instabilities are seen on the western walls of bubbles, the irregularities are occasionally seen forming on the eastern walls. Makela *et al.* [2006] showed such an example from airglow observations on the Haleakala Volcano in Hawaii during a geomagnetic storm in February 2003. They postulated that the east-wall irregularities must be due to a westward neutral wind, instead of an eastward wind. Disturbance dynamo theory supports that a westward wind should exist at mid-latitudes during storm times (see Section 2.4). Makela *et al.* [2006] did observe a southwest-propagating brightness enhancement, but did not have coincident measurements of the

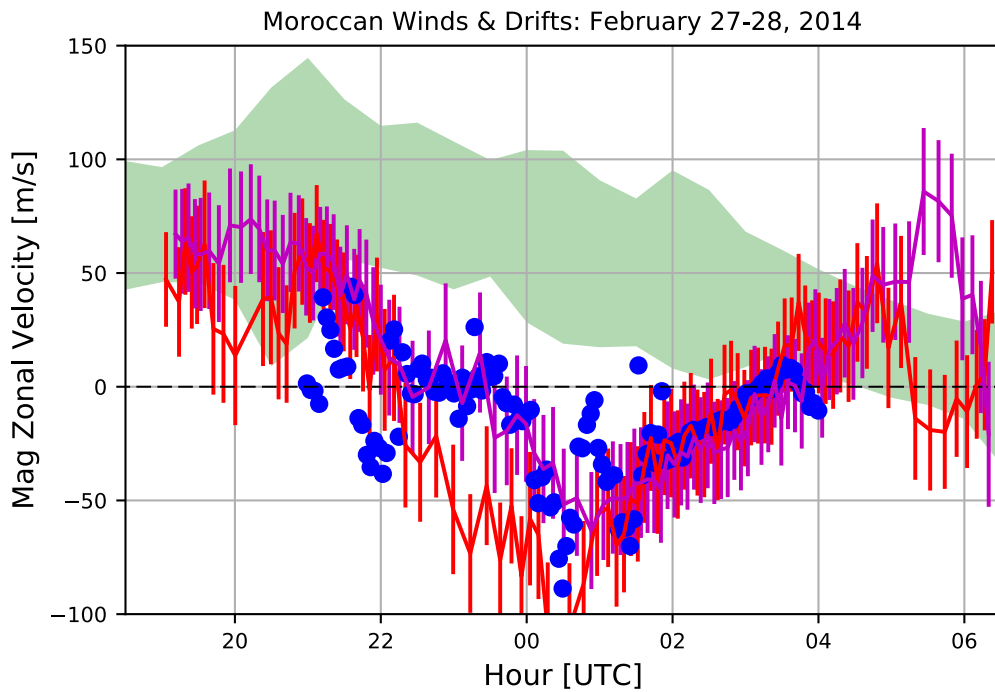


Figure 6.15: Estimated plasma drifts and neutral winds for the night of February 27, 2014. The plasma drift estimates from the cross-correlation method are marked as blue dots. The zonal neutral winds are plotted from the east (red) and west (magenta) look directions with error bars for the measurement uncertainties. The green shaded region displays typical range of quiet-time zonal neutral winds for February 2014.

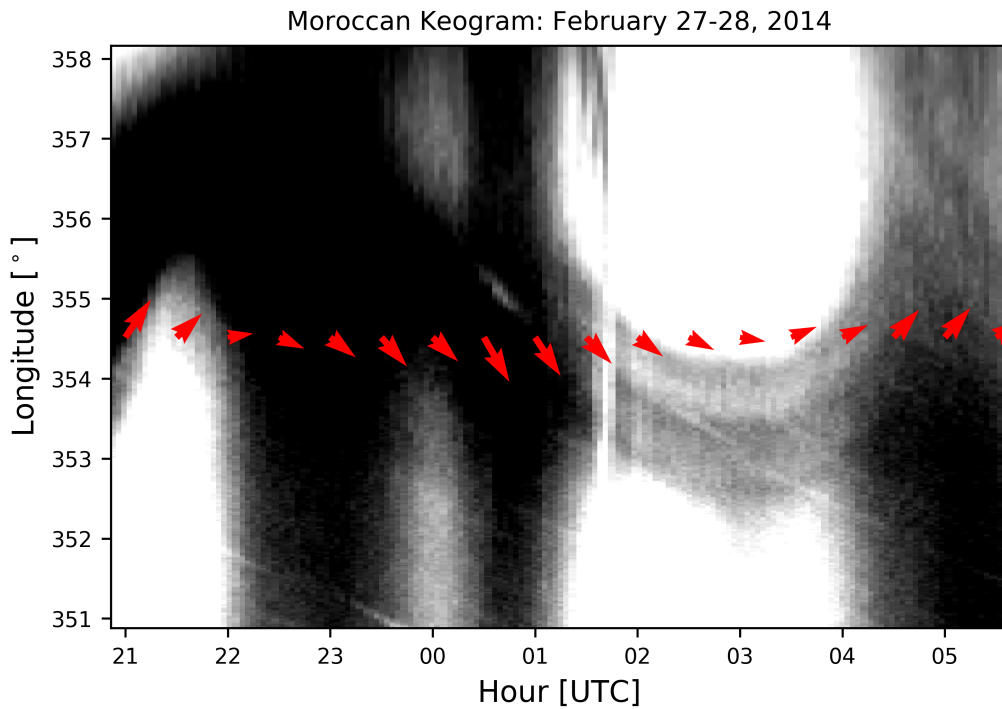


Figure 6.16: Keogram with an overlay of zonal neutral wind vectors from the night of February 27, 2014. The red arrows are motion vectors that describe how a neutral particle would move if the winds were constant across the field of view for that time step.

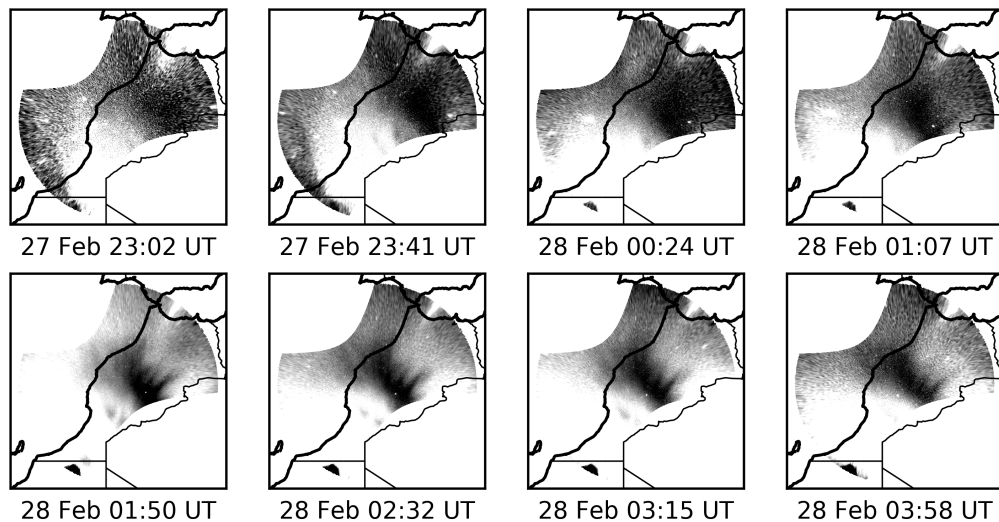


Figure 6.17: Time lapse of bubbles on the night of February 27, 2014. The airglow images are projected to an emission altitude of 250 km.

thermospheric winds to validate this. With joint measurements from the ASI and FPI in Morocco during storm times, we add direct neutral measurements that can validate if the neutral wind is needed to drive the secondary instabilities.

We first discuss the storm-time EPB on February 27, 2014, as it closely compares with what was observed by *Makela et al.* [2006]. This event saw a westward turning of the neutral winds (with speeds up to 100 m/s) which correlated with a westward drift of the plasma bubble. During the westward motion, instabilities formed off the eastern wall of the EPB. Figure 6.17 shows three distinct eastern-wall instabilities during this storm period. These measurements validate that a westward zonal wind was required to drive the secondary plume formation, in agreement with the prediction by *Makela et al.* [2006].

To strengthen this argument, we discuss the observed EPBs during the August 23, 2016, geomagnetic storm. This event showed weak (nearly 0 m/s) zonal winds which matched the motionless EPBs. The stalled bubbles show no secondary irregularities on either their eastern or western walls (see Figure 6.12). Without a zonal wind, both walls remained unchanged.

As a neutral wind is needed relative to the bubble motion to destabilize the bubble wall and cause secondary instabilities, and we have shown in the prior sections that the dynamo causes the plasma drifts to match the neutral winds, we must conclude that the dynamo is not 100% effective during the entire night. In fact, some slippage must occur to seed secondary bubble development. These two cases demonstrate that a zonal neutral wind is required to seed secondary instabilities on the walls of the EPBs, with eastward winds leading to west-wall instabilities and westward winds leading to east-wall instabilities.

6.4 Summary

We summarize the key points learned from the two methodologies we have established to analyze coincident measurements of neutral winds and EPB drift speeds:

- The cross-correlation technique allows for a quantitative assessment of the drifts and winds. However, being an automated process, it requires

the user to know when bubbles are visible, to know when the results are applicable. Results can also be biased due to bubble deformation and tilting, or other structures such as the Milky Way entering the FOV of the ASI.

- The keogram/wind vector technique is only qualitative, but allows for comparison of the winds and drifts without being biased by potential sources like the cross-correlation technique.
- During quiet-times, the cross-correlation technique showed that the plasma drifts matched neutral winds, typically within the FPI measurement uncertainties. The keogram technique confirms this, showing that EPB motion follows the zonal neutral winds. This is in agreement with prior findings that the F-region dynamo is in full effect after bubble formation.
- The ASI observed bubbles stalling and drifting westward while the FPI observed the zonal wind speed stalling and blowing westward during two storm-time events. This is the first comparison between collocated neutral wind measurements and EPB drifts during a geomagnetic storm. The cross-correlation method and the keogram method both reveal good agreement between the neutral wind and EPB drift speeds. This signifies that the disturbance dynamo is fully activated over the mid-latitudes during geomagnetic storms.
- Secondary plumes were found to require a zonal wind to form. The secondary instabilities were seen on the western wall of the EPB during a night when eastward winds were measured, and on a different night when westward winds were measured, they were seen on the eastern wall of the EPB. Finally, when a nearly 0 m/s zonal wind was observed, neither wall produced secondary plumes.

CHAPTER 7

CONCLUSIONS AND FUTURE DIRECTIONS

This work demonstrates the scientific value of collecting long-term thermospheric wind and temperature measurements. Through the observations from ground-based Fabry-Perot interferometers, we are able to study the daily, monthly, yearly, and solar cycle variations in the neutral parameters at various geographic latitudes and longitudes. This information will improve our understanding of the physics, enabling advancements in models of the upper atmosphere. This chapter summarizes the contributions discussed in this dissertation. It also offers a direction for future researchers to take utilizing airglow observations.

7.1 Contributions

In the past decade, many FPIs were deployed with the intention of collecting long-term measurements of the neutral parameters of the thermosphere. Taking advantage of the naturally occurring redline emission from the dissociative recombination of O_2^+ , the ground-based FPIs get nightly recordings of the neutral winds and temperatures. Much effort has been spent improving the quality of the FPI data product in order to make the data useful to the community. Quality control of FPI data was initially a manual (and arbitrary) task requiring a binary classification of each individual airglow measurement. An automated data-quality control system was created to systematically flag the data in a three-tiered system: good, use with caution, or bad. With a more reliable FPI data product, the measurements can be combined to create statistically significant long-term analyses.

Climatological averaging functions have been designed to bin the FPI data over time and space, both from different observation geometries and from different sites. The monthly means of the neutral winds and temperatures

are calculated along with relevant, physically meaningful parameters such as the day-to-day variability. The results can be separated not only by local time and month, but also by $F_{10.7}$ solar flux. Using the designed climatologies for the Brazilian, United States, and Moroccan regions for the past solar cycle, we were able to determine that there is a negligible effect of solar cycle on the neutral winds. However, small post-sunset and midnight enhancements were seen in the winds in certain months. The opposite was found for the neutral temperatures which have a direct dependence on solar flux, in agreement with prior findings. Geographic variations can also be analyzed. There are distinct differences in the meridional winds from different latitude regions, caused by differences in forcing. The low-latitude was dominated by solar forcing while the mid-latitude sites showed evidence of forcing from the polar region. Additionally, longitudinal comparisons were made between the zonal winds over PARI and Oukaïmeden. The geomagnetic latitudes of the sites were found to affect the timing of the east-to-west reversals, with PARI leading Oukaïmeden by two hours. On the other hand, the timing of the eastward peak flow, which differed greatly by month, is attributed to longitudinal variations.

The long-term datasets are used for more than just observing thermospheric physics. The FPI data were used to improve the horizontal wind model, correcting poor agreements seen over Brazil where data were scarce and the harmonic functions were not scaled properly. The FPI measurements were also used to validate the updated HWM. In order to accurately compare FPI measurements with model data, the model must be weighted by the vertical airglow profile. This was done cautiously for HWM14, as it relies on the accuracy of gradients in HWM, IRI, and MSIS. It was shown that the model has greatly improved the fitting with the Brazilian measurements, but still has issues over North America, where data were also ingested. Data from Morocco also differed from the model, which implies that ground-based data are needed over the African sector to improve HWM. Furthermore, it was shown that a harmonic fit of the data, consisting of annual, semiannual, and terannual components, better captures the seasonal variation of the neutral wind data. The findings indicate that adding the terannual (and potentially higher) frequency component to the model would increase its accuracy.

Additionally, the FPI data has been used to investigate the coupling between the neutral winds and equatorial plasma bubbles. The ASI can track

EPB motion, indicative of the plasma drift speed in the thermosphere. The ASI and FPI have already proven that the F-region dynamo is fully activated each night, with daily variation driving differences. We have implemented two methods of analysis to automatically make EPB/wind comparisons: one quantitative method using cross-correlations and one qualitative method using keograms. Both methods aided in validating that the dynamo is fully active in the nighttime thermosphere. We then presented the first storm-time drift to wind comparison from collocated ASI and FPI data. During geomagnetic storms over Morocco, the bubbles were seen to stall and reverse in the images. However, the neutral wind estimates correlated highly with these drifts. The analysis validates that the disturbance dynamo is in full effect during geomagnetic storms at night.

7.2 Future Directions

Although our FPI measurements have contributed to an understanding of the thermosphere around 250 km, there are still many outstanding questions.

Of particular note in our large dataset is the amount of day-to-day variability seen in the neutral winds and temperatures. It would be greatly beneficial to understand the underlying physics that govern these small changes. The daily variability is important to account for in models and simulations as small variations can aid or hinder upper atmospheric phenomena such as EPB formation, TAD propagation, and MTMs. Work is currently underway to characterize the seasonality of the MTM feature in the three regions studied here. Properly quantifying the geographic extent, as well as the daily variability of MTMs, is a current topic of study in the community. Grasping the daily fluctuations would greatly help to enable short-term predictions of upper atmospheric conditions, enabling users of global navigation satellite systems and satellite-based communication to better prepare for ionosphere-induced issues.

While the horizontal neutral winds have been well analyzed with our FPI measurements, we still cannot trust the vertical wind climatologies with absolute certainty. A new experiment must be run to completely validate the existence, or lack, of vertical winds in the thermosphere. Both scattering and OH emissions can factor into the periodically observed apparent vertical

winds [*Harding et al.*, 2017], and, in order to test this, a collocated all-sky imager and Fabry-Perot interferometer are required. First of all, a calibrated ASI for the 630.0-nm redline emission is needed to account for the atmospheric scatter in our measurements. The calibration is needed to estimate the amount of light scattered into our FPI. Secondly, the ASI needs to take observations of the OH lines, again requiring calibration. The relative 630.0-nm brightness and OH brightness is required to estimate the potential OH contamination. Our deployed ASIs do have filterwheels that would allow alternating exposures with the two filters, enabling both factors to be accounted for using the same instrument. However, the current systems do not have a method to do the calibrations. This experiment must run for a full year to explain the seasonal differences in the dawn and dusk vertical winds.

We are only able to validate HWM14 in the localized regions of the thermosphere surrounding our instruments. A new deployment, or redeployment, of ground-based FPIs would be required to cover latitude and longitude sectors that have previously been neglected (such as the African sector). Still, ground-based instruments cannot completely cover the globe. Also, the FPI measurements do not produce a vertical profile of the neutral parameters. We have shown how altitudinal gradients in the winds and temperatures can change the measurements from the ground; however, we lack the neutral measurements outside the redline emission altitude to confirm or deny the existence of meaningful gradients. Models like HWM assume smooth transitions between the mesosphere and thermosphere in the E-F valley region where measurements are difficult to obtain. HWM also assumes an arbitrary altitude cutoff between the thermosphere and exosphere, above which the neutral winds remain constant with altitude. Solving these problems will require new experimentation, such as a space-based interferometer or improved lidar techniques.

REFERENCES

- Abalde, J. R. (2004), Height-resolved ionospheric drifts at low latitudes from simultaneous OI 777.4 nm and OI 630.0 nm imaging observations, *Journal of Geophysical Research*, *109*(A11), A11,308, doi:10.1029/2004JA010560.
- Abdu, M. A., P. T. Jayachandran, J. MacDougall, J. F. Cecile, and J. H. Sobral (1998), Equatorial F region zonal plasma irregularities drifts under magnetospheric disturbances, *Geophysical Research Letters*, *25*(22), 4137–4140, doi:10.1007/s13398-014-0173-7.2.
- Abdu, M. A., I. S. Batista, H. Takahashi, J. MacDougall, J. H. Sobral, A. F. Medeiros, and N. B. Trivedi (2003), Magnetospheric disturbance induced equatorial plasma bubble development and dynamics: A case study in Brazilian sector, *Journal of Geophysical Research: Space Physics*, *108*(A12), 1–13, doi:10.1029/2002JA009721.
- Akmaev, R. A. (2011), Whole atmosphere modeling: Connecting terrestrial and space weather, *Reviews of Geophysics*, *49*, doi:10.1029/2011RG000364.
- Babcock, H. (1923), A Study of the Green Auroral Line by the Interference Method, *The Astrophysical Journal*, *57*, 209, doi:10.1086/142747.
- Basu, S., E. Kudeki, C. E. Valladares, E. J. Weber, H. P. Zengingonul, S. Bhattacharyya, R. Sheehan, J. W. Meriwether, M. Biondi, H. Kuenzler, and J. Espinoza (1996), Scintillations, plasma drifts, and neutral winds in the equatorial ionosphere after sunset, *Journal of Geophysical Research: Space Physics*, *101*(A12), 26,795–26,809, doi:10.1029/96JA00760.
- Bilitza, D., and B. Reinisch (2008), International Reference Ionosphere 2007: Improvements and new parameters, *Advances in Space Research*, *42*(4), 599–609, doi:10.1016/j.asr.2007.07.048.
- Biondi, M., and D. P. Sipler (1985), Horizontal and vertical winds and temperatures in the equatorial thermosphere: Measurements from Natal, Brazil during August–September 1982, *Planetary and Space Science*, *33*(7), 817–823, doi:10.1016/0032-0633(85)90035-2.
- Biondi, M., J. W. Meriwether, B. G. Fejer, and R. Woodman (1988), Measurements of the dynamics and coupling of the equatorial thermosphere

- and the F-region ionosphere in Peru, *Journal of Atmospheric and Terrestrial Physics*, 50(10-11), 937–942, doi:10.1016/0021-9169(88)90081-5.
- Blanc, M., and A. D. Richmond (1980), The ionospheric disturbance dynamo, *Journal of Geophysical Research*, 85(9), 1669–1686, doi:10.1029/JA085iA04p01669.
- Brum, C. G. M., C. A. Tepley, J. T. Fentzke, E. Robles, P. L. Dragotti, and S. A. González (2012), Long-term changes in the thermospheric neutral winds over Arecibo: Climatology based on over three decades of Fabry-Perot observations, *Journal of Geophysical Research: Space Physics*, 117, 1–16, doi:10.1029/2011JA016458.
- Buonsanto, M. (1999), Ionospheric storms - a review, *Space Science Reviews*, 88(3/4), 563–601, doi:10.1023/A:1005107532631.
- Burke, W. J. (2004), Longitudinal variability of equatorial plasma bubbles observed by DMSP and ROCSAT-1, *Journal of Geophysical Research*, 109(A12), A12,301, doi:10.1029/2004JA010583.
- Chapagain, N. P., J. J. Makela, J. W. Meriwether, D. J. Fisher, R. A. Buriti, and A. F. Medeiros (2012), Comparison of nighttime zonal neutral winds and equatorial plasma bubble drift velocities over Brazil, *Journal of Geophysical Research*, 117(A6), A06,309, doi:10.1029/2012JA017620.
- Chapagain, N. P., D. J. Fisher, J. W. Meriwether, J. L. Chau, and J. J. Makela (2013), Comparison of zonal neutral winds with equatorial plasma bubble and plasma drift velocities, *Journal of Geophysical Research: Space Physics*, 118(4), 1802–1812, doi:10.1002/jgra.50238.
- Chartier, A. T., J. J. Makela, H.-L. Liu, G. S. Bust, and J. Noto (2015), Modeled and observed equatorial thermospheric winds and temperatures, *Journal of Geophysical Research: Space Physics*, 120(7), 5832–5844, doi:10.1002/2014JA020921.
- Dickinson, R., and J. Geisler (1968), Vertical motion field in the middle thermosphere from satellite drag densities, *Monthly Weather Review*, 96(9), 606–616, doi:10.1175/1520-0493(1968)096.
- Drob, D. P., J. T. Emmert, G. Crowley, J. M. Picone, G. G. Shepherd, W. Skinner, P. B. Hays, R. J. Niciejewski, M. F. Larsen, C.-Y. She, J. W. Meriwether, G. Hernandez, M. J. Jarvis, D. P. Sipler, C. A. Tepley, M. S. O'Brien, J. R. Bowman, Q. Wu, Y. Murayama, S. Kawamura, I. M. Reid, and R. A. Vincent (2008), An empirical model of the Earth's horizontal wind fields: HWM07, *Journal of Geophysical Research: Space Physics*, 113(A12), 1–18, doi:10.1029/2008JA013668.

- Drob, D. P., J. T. Emmert, J. W. Meriwether, J. J. Makela, E. Doornbos, M. G. Conde, G. Hernandez, J. Noto, K. A. Zawdie, S. E. McDonald, J. D. Huba, and J. H. Klenzing (2015), An update to the Horizontal Wind Model (HWM): The quiet time thermosphere, *Earth and Space Science*, *2*(7), 301–319, doi:10.1002/2014EA000089.
- Dungey, J. (1956), Convective diffusion in the equatorial F region, *Journal of Atmospheric and Terrestrial Physics*, *9*(5-6), 304–310, doi:10.1016/0021-9169(56)90148-9.
- Emmert, J. T., B. G. Fejer, G. G. Shepherd, and B. H. Solheim (2002), Altitude dependence of middle and low-latitude daytime thermospheric disturbance winds measured by WINDII, *Journal of Geophysical Research: Space Physics*, *107*(A12), 1–15, doi:10.1029/2002JA009646.
- Emmert, J. T., B. G. Fejer, and D. P. Sipler (2003), Climatology and latitudinal gradients of quiet time thermospheric neutral winds over Millstone Hill from Fabry-Perot interferometer measurements, *Journal of Geophysical Research: Space Physics*, *108*, 1–12, doi:10.1029/2002JA009765.
- Emmert, J. T., M. L. Faivre, G. Hernandez, M. J. Jarvis, J. W. Meriwether, R. J. Niciejewski, D. P. Sipler, and C. A. Tepley (2006), Climatologies of nighttime upper thermospheric winds measured by ground-based Fabry-Perot interferometers during geomagnetically quiet conditions: 1. Local time, latitudinal, seasonal, and solar cycle dependence, *Journal of Geophysical Research: Space Physics*, *111*(A12), A12,302, doi:10.1029/2006JA011948.
- Emmert, J. T., D. P. Drob, G. G. Shepherd, G. Hernandez, M. J. Jarvis, J. W. Meriwether, R. J. Niciejewski, D. P. Sipler, and C. A. Tepley (2008), DWM07 global empirical model of upper thermospheric storm-induced disturbance winds, *Journal of Geophysical Research*, *113*(A11), A11,319, doi:10.1029/2008JA013541.
- Fagundes, P. R., Y. Sahai, I. S. Batista, J. A. Bittencourt, M. A. Abdu, and H. Takashi (1997), Vertical and zonal equatorial F-region plasma bubble velocities determined from OI 630 nm nightglow imaging, *Advances in Space Research*, *20*(6), 1297–1300, doi:10.1016/S0273-1177(97)00790-4.
- Faivre, M. L., J. W. Meriwether, C. G. Fesen, and M. Biondi (2006), Climatology of the midnight temperature maximum phenomenon at Arequipa, Peru, *Journal of Geophysical Research: Space Physics*, *111*(January), 1–10, doi:10.1029/2005JA011321.
- Fejer, B. G. (1981), The equatorial ionospheric electric fields. A review, *Journal of Atmospheric and Terrestrial Physics*, *43*(516), 377–386, doi:10.1016/0021-9169(81)90101-X.

- Fejer, B. G., D. T. Farley, R. Woodman, and C. Calderon (1979), Dependence of equatorial F region vertical drifts on season and solar cycle, *Journal of Geophysical Research*, *84*(A10), 5792, doi:10.1029/JA084iA10p05792.
- Fejer, B. G., E. Paula, S. A. González, and R. Woodman (1991), Average vertical and zonal F region plasma drifts over Jicamarca, *Journal of Geophysical ...*, *96*(June 1988).
- Fejer, B. G., J. T. Emmert, and D. P. Sipler (2002), Climatology and storm time dependence of nighttime thermospheric neutral winds over Millstone Hill, *Journal of Geophysical Research: Space Physics*, *107*, 1–9, doi:10.1029/2001JA000300.
- Fisher, D. J. (2013), Three-dimensional wind measurements and modeling using a bi-static Fabry-Perot interferometer system in Brazil, M.S. thesis, University of Illinois at Urbana-Champaign.
- Fisher, D. J., J. J. Makela, J. W. Meriwether, R. A. Buriti, Z. Benkhaldoun, M. Kaab, and A. Lagheryeb (2015), Climatologies of nighttime thermospheric winds and temperatures from Fabry-Perot interferometer measurements: From solar minimum to solar maximum, *Journal of Geophysical Research: Space Physics*, *120*(8), 6679–6693, doi:10.1002/2015JA021170.
- Ford, E. A. K., A. L. Aruliah, E. M. Griffin, and I. McWhirter (2006), Thermospheric gravity waves in Fabry-Perot Interferometer measurements of the 630.0nm OI line, *Annales Geophysicae*, *24*(2), 555–566, doi:10.5194/angeo-24-555-2006.
- Fuller-Rowell, T. J., M. V. Codrescu, H. Rishbeth, R. J. Moffett, and S. Quegan (1996), On the seasonal response of the thermosphere and ionosphere to geomagnetic storms, *Journal of Geophysical Research: Space Physics*, *101*(A2), 2343–2353, doi:10.1029/95JA01614.
- Guo, J., W. Wan, J. M. Forbes, E. K. Sutton, R. S. Nerem, and S. Bruinsma (2008), Interannual and latitudinal variability of the thermosphere density annual harmonics, *Journal of Geophysical Research: Space Physics*, *113*(A8), doi:10.1029/2008JA013056.
- Harding, B. J., T. W. Gehrels, and J. J. Makela (2014), Nonlinear regression method for estimating neutral wind and temperature from Fabry-Perot interferometer data., *Applied Optics*, *53*(4), 666–73, doi:10.1364/AO.53.000666.
- Harding, B. J., J. J. Makela, J. Qin, D. J. Fisher, C. R. Martinis, J. Noto, and C. M. Wrasse (2017), Atmospheric scattering effects on ground-based measurements of thermospheric vertical wind, horizontal wind, and temperature, *Journal of Geophysical Research, Space Physics*, doi:10.1002/2017JA023942.

- Hays, P. B., D. Rusch, R. G. Roble, and J. C. G. Walker (1978), The O I (6300 Å) airglow, *Reviews of Geophysics and Space Physics*, *16*(2), 225, doi:10.1029/RG016i002p00225.
- Hedin, A. E., J. Salah, J. Evans, C. Reber, G. Newton, N. W. Spencer, D. Kayser, D. Alcaydé, P. Bauer, L. L. Cogger, and J. P. McClure (1977), A global thermospheric model based on mass spectrometer and incoherent scatter data MSIS, 1. N₂ density and temperature, *Journal of Geophysical Research*, *82*(16), 2139–2147, doi:10.1029/JA082i016p02139.
- Hedin, A. E., N. W. Spencer, and T. L. Killeen (1988), Empirical global model of upper thermosphere winds based on Atmosphere and Dynamics Explorer satellite data, *Journal of Geophysical Research*, *93*(A9), 9959, doi:10.1029/JA093iA09p09959.
- Hedin, A. E., M. Biondi, R. G. Burnside, G. Hernandez, R. Johnson, T. L. Killeen, C. Mazaudier, J. W. Meriwether, J. Salah, R. Sica, R. Smith, N. W. Spencer, V. Wickwar, and T. Viridi (1991), Revised global model of thermosphere winds using satellite and ground-based observations, *Journal of Geophysical Research*, *96*(A5), 7657, doi:10.1029/91JA00251.
- Hedin, A. E., E. L. Fleming, A. Manson, F. J. Schmidlin, S. K. Avery, R. R. Clark, S. J. Franke, G. Fraser, T. Tsuda, F. Vial, and R. A. Vincent (1996), Empirical wind model for the upper, middle and lower atmosphere, *Journal of Atmospheric and Terrestrial Physics*, *58*(13), 1421–1447, doi:10.1016/0021-9169(95)00122-0.
- Heelis, R. A., P. C. Kendall, R. J. Moffett, D. W. Windle, and H. Rishbeth (1974), Electrical coupling of the E- and F-regions and its effect on F-region drifts and winds, *Planetary and Space Science*, *22*(5), 743–756, doi:10.1016/0032-0633(74)90144-5.
- Hernandez, G. (1982), Mid-latitude thermospheric neutral kinetic temperatures, 1, Solar, geomagnetic, and long-term effects, *Journal of Geophysical Research*, *87*(1), 1623–1632, doi:10.1029/JA087iA03p01623.
- Hernandez, G., and R. G. Roble (1976a), Direct measurements of nighttime thermospheric winds and temperatures, 1. Seasonal variations during geomagnetic quiet periods, *Journal of Geophysical Research*, *81*(13), 2065, doi:10.1029/JA081i013p02065.
- Hernandez, G., and R. G. Roble (1976b), Direct measurements of nighttime thermospheric winds and temperatures, 2. Geomagnetic storms, *Journal of Geophysical Research*, *81*(28), 5173–5181, doi:10.1029/JA081i028p05173.
- Herrero, F. A., H. G. Mayr, and N. W. Spencer (1983), Latitudinal (seasonal) variations in the thermospheric midnight temperature maximum:

- A tidal analysis, *Journal of Geophysical Research*, 88(A9), 7225, doi:10.1029/JA088iA09p07225.
- Herzberg, G. (1944), *Atomic Spectra and Atomic Structure*, Dover Publications, New York, NY.
- Immel, T. J., E. Sagawa, S. L. England, S. B. Henderson, M. E. Hagan, S. B. Mende, H. U. Frey, C. M. Swenson, and L. J. Paxton (2006), Control of equatorial ionospheric morphology by atmospheric tides, *Geophysical Research Letters*, 33(15), L15,108, doi:10.1029/2006GL026161.
- Kaab, M., Z. Benkhaldoun, D. J. Fisher, B. J. Harding, A. Bounhir, J. J. Makela, A. Lagheryeb, K. Malki, A. Daassou, and M. Lazrek (2017), Climatology of thermospheric neutral winds over Oukaimeden Observatory in Morocco, *Annales Geophysicae*, 35(1), 161–170, doi:10.5194/angeo-35-161-2017.
- Kelley, M. C. (1989), *The Earth's Ionosphere*, Academic Press, Burlington, MA.
- Kelley, M. C., and J. J. Makela (2003), The first coordinated ground- and space-based optical observations of equatorial plasma bubbles, *Geophysical Research Letters*, 30(14), 5–8, doi:10.1029/2003GL017301.
- Killeen, T. L., and P. B. Hays (1984), Doppler line profile analysis for a multichannel Fabry-Perot interferometer, *Applied Optics*, 23(4), 612, doi:10.1364/AO.23.000612.
- Knipp, D. J., B. Emery, M. Engebretson, X. Li, A. McAllister, T. Mukai, S. Kokubun, E. G. D. Reeves, D. S. Evans, T. Obara, X. Pi, T. Rosenberg, A. Weatherwax, M. McHarg, F. Chun, K. Mosely, M. V. Codrescu, L. Lanzerotti, F. J. Rich, J. Sharber, and P. Wilkinson (1998), An overview of the early November 1993 geomagnetic storm, *Journal of Geophysical Research*, 103(A11), 26,197, doi:10.1029/98JA00762.
- Krassovsky, V., N. Shefov, and V. Yarin (1962), Atlas of the airglow spectrum 300012400 Å, *Planetary and Space Science*, 9(12), 883–915, doi:10.1016/0032-0633(62)90008-9.
- Kudeki, E., A. Akgiray, M. A. Milla, J. L. Chau, and D. L. Hysell (2007), Equatorial spread-F initiation: Post-sunset vortex, thermospheric winds, gravity waves, *Journal of Atmospheric and Solar-Terrestrial Physics*, 69(17-18), 2416–2427, doi:10.1016/j.jastp.2007.04.012.
- Link, R., and L. L. Cogger (1988), A reexamination of the O I 6300-Å nightglow, *Journal of Geophysical Research*, 93(A9), 9883–9892, doi:10.1029/JA093iA09p09883.

- Link, R., and L. L. Cogger (1989), Correction to A reexamination of the O I 6300-Å nightglow by R. Link and L. L. Cogger, *Journal of Geophysical Research*, *94*(A2), 1556, doi:10.1029/JA094iA02p01556.
- Liu, X., J. Xu, S. Zhang, G. Jiang, Q. Zhou, W. Yuan, J. Noto, and R. Kerr (2014), Thermospheric planetary wave-type oscillations observed by FPIs over Xinglong and Millstone Hill, *Journal of Geophysical Research: Space Physics*, *119*(8), 6891–6901, doi:10.1002/2014JA020043.
- Makela, J. J., and M. C. Kelley (2003), Field-aligned 777.4-nm composite airglow images of equatorial plasma depletions, *Geophysical Research Letters*, *30*(8), 1–4, doi:10.1029/2003GL017106.
- Makela, J. J., B. M. Ledvina, M. C. Kelley, and P. M. Kintner (2004), Analysis of the seasonal variations of equatorial plasma bubble occurrence observed from Haleakala, Hawaii, *Annales Geophysicae*, *22*(9), 3109–3121, doi:10.5194/angeo-22-3109-2004.
- Makela, J. J., M. C. Kelley, and M. J. Nicolls (2006), Optical observations of the development of secondary instabilities on the eastern wall of an equatorial plasma bubble, *Journal of Geophysical Research*, *111*(A9), A09311, doi:10.1029/2006JA011646.
- Makela, J. J., J. W. Meriwether, Y. Huang, and P. J. Sherwood (2011), Simulation and analysis of a multi-order imaging Fabry-Perot interferometer for the study of thermospheric winds and temperatures, *Applied Optics*, *50*(22), 4403–4416, doi:10.1364/AO.50.004403.
- Makela, J. J., J. W. Meriwether, A. J. Ridley, M. Ciocca, and M. W. Castellez (2012), Large-scale measurements of thermospheric dynamics with a multisite Fabry-Perot interferometer network: Overview of plans and results from midlatitude measurements, *International Journal of Geophysics*, *2012*(3), 1–10, doi:10.1155/2012/872140.
- Makela, J. J., D. J. Fisher, J. W. Meriwether, R. A. Buriti, and A. F. Medeiros (2013), Near-continual ground-based nighttime observations of thermospheric neutral winds and temperatures over equatorial Brazil from 2009 to 2012, *Journal of Atmospheric and Solar-Terrestrial Physics*, *103*, 94–102, doi:10.1016/j.jastp.2012.11.019.
- Makela, J. J., B. J. Harding, J. W. Meriwether, R. Mesquita, S. Sanders, A. J. Ridley, M. W. Castellez, M. Ciocca, G. D. Earle, N. A. Frissell, D. L. Hampton, A. J. Gerrard, J. Noto, and C. R. Martinis (2014), Storm time response of the midlatitude thermosphere: Observations from a network of Fabry-Perot interferometers, *Journal of Geophysical Research: Space Physics*, *119*(8), 6758–6773, doi:10.1002/2014JA019832.

- Martinis, C. R. (2003), Latitude dependence of zonal plasma drifts obtained from dual-site airglow observations, *Journal of Geophysical Research*, *108*(A3), 1–10, doi:10.1029/2002JA009462.
- Mayr, H. G., and H. Volland (1972), Theoretical model for the latitude dependence of the thermospheric annual and semiannual variations, *Journal of Geophysical Research*, *77*(34), 6774–6790, doi:10.1029/JA077i034p06774.
- Mayr, H. G., I. Harris, and N. W. Spencer (1978), Some properties of upper atmosphere dynamics, *Reviews of Geophysics*, *16*(4), 539–565, doi:10.1029/RG016i004p00539.
- Mayr, H. G., I. Harris, N. W. Spencer, A. E. Hedin, L. E. Wharton, H. S. Porter, J. C. G. Walker, and H. C. Carlson (1979), Tides and the midnight temperature anomaly in the thermosphere, *Geophysical Research Letters*, *6*(6), 1–4, doi:10.1029/GL006i006p00447.
- McClure, J. P., W. B. Hanson, and J. H. Hoffman (1977), Plasma bubbles and irregularities in the equatorial ionosphere, *Journal of Geophysical Research*, *82*(19), 2650–2656, doi:10.1029/JA082i019p02650.
- McLandress, C., G. G. Shepherd, and B. H. Solheim (1996), Satellite observations of thermospheric tides: Results from the Wind Imaging Interferometer on UARS, *Journal of Geophysical Research*, *101*(D2), 4093, doi:10.1029/95JD03359.
- Mendillo, M., and J. Baumgardner (1982), Airglow characteristics of equatorial plasma depletions, *Journal of Geophysical Research*, *87*(A9), 7641, doi:10.1029/JA087iA09p07641.
- Menvielle, M., and A. Berthelier (1991), The K_p-derived planetary indices: Description and availability, *Reviews of Geophysics*, *29*(3), 415, doi:10.1029/91RG00994.
- Mesquita, R., J. W. Meriwether, J. J. Makela, D. J. Fisher, B. J. Harding, S. Sanders, F. Tesema, and A. J. Ridley (Submitted), New results on the mid-latitude midnight temperature maximum, *Annales Geophysicae*.
- Meriwether, J. W., and M. Biondi (1995), Optical interferometric observations of 630-nm intensities, thermospheric winds and temperatures near the geomagnetic equator, *Advances in Space Research*, *16*(5), 17–26, doi:10.1016/0273-1177(95)00168-E.
- Meriwether, J. W., J. J. Makela, Y. Huang, D. J. Fisher, R. A. Buriti, A. F. Medeiros, and H. Takahashi (2011), Climatology of the nighttime equatorial thermospheric winds and temperatures over Brazil near solar minimum, *Journal of Geophysical Research*, *116*(A4), A04,322, doi:10.1029/2011JA016477.

- Paetzold, H. K., and H. Zschörner (1961), The structure of the upper atmosphere and its variations after satellite observations, *Space Research*, *2*, 958–973.
- Palmer, D. M. (2009), A fast chi-squared technique for period search of irregularly sampled data, *The Astrophysical Journal*, *695*(1), 496–502, doi:10.1088/0004-637X/695/1/496.
- Picone, J. M., A. E. Hedin, D. P. Drob, and A. C. Aikin (2002), NRLMSISE-00 empirical model of the atmosphere: Statistical comparisons and scientific issues, *Journal of Geophysical Research*, *107*(A12), 1–16, doi:10.1029/2002JA009430.
- Pimenta, A. A., J. A. Bittencourt, P. R. Fagundes, Y. Sahai, R. A. Buriti, H. Takahashi, and M. J. Taylor (2003), Ionospheric plasma bubble zonal drifts over the tropical region: A study using OI 630 nm emission all-sky images, *Journal of Atmospheric and Solar-Terrestrial Physics*, *65*(10), 1117–1126, doi:10.1016/S1364-6826(03)00149-4.
- Raghavarao, R., W. Hoegy, N. W. Spencer, and L. E. Wharton (1993), Neutral temperature anomaly in the equatorial thermosphere—A source of vertical winds, *Geophysical Research Letters*, *20*(11), 1023–1026, doi:10.1029/93GL01253.
- Rees, D. (1995), Observations and modelling of ionospheric and thermospheric disturbances during major geomagnetic storms: A review, *Journal of Atmospheric and Terrestrial Physics*, *57*(12), 1433–1457, doi:10.1016/0021-9169(94)00142-B.
- Ridley, A. J., Y. Deng, and G. Tóth (2006), The global ionosphere-thermosphere model, *Journal of Atmospheric and Solar-Terrestrial Physics*, *68*(December), 839–864, doi:10.1016/j.jastp.2006.01.008.
- Rishbeth, H. (1971), Polarization fields produced by winds in the equatorial F-region, *Planetary and Space Science*, *19*(3), 357–369, doi:10.1016/0032-0633(71)90098-5.
- Rishbeth, H. (2000), The equatorial F-layer: progress and puzzles, *Annales Geophysicae*, *18*(7), 730–739, doi:10.1007/s00585-000-0730-6.
- Rishbeth, H., and O. K. Garriott (1969), *Introduction to Ionospheric Physics*, Academic Press, New York, NY.
- Roble, R. G. (1983), Dynamics of the Earth’s thermosphere, *Reviews of Geophysics*, *21*(2), 217, doi:10.1029/RG021i002p00217.
- Salah, J., W. Deng, and R. R. Clark (1996), Observed response of the Earth’s lower thermosphere to a major geomagnetic storm, *Geophysical Research Letters*, *23*(5), 575–578, doi:10.1029/96GL00307.

- Santos, A. M., M. A. Abdu, J. R. Souza, J. H. Sobral, and I. S. Batista (2016a), Disturbance zonal and vertical plasma drifts in the Peruvian sector during solar minimum phases, *Journal of Geophysical Research A: Space Physics*, *121*(3), 2503–2521, doi:10.1002/2015JA022146.
- Santos, A. M., M. A. Abdu, J. R. Souza, J. H. Sobral, I. S. Batista, and C. M. Denardini (2016b), Storm time equatorial plasma bubble zonal drift reversal due to disturbance Hall electric field over the Brazilian region, *Journal of Geophysical Research: Space Physics*, *121*(6), 5594–5612, doi:10.1002/2015JA022179.
- Scherliess, L., and B. G. Fejer (1997), Storm time dependence of equatorial disturbance dynamo zonal electric fields, *Journal of Geophysical Research: Space Physics*, *102*(A11), 24,037–24,046, doi:10.1029/97JA02165.
- Sobral, J. H., V. M. de Castilho, M. A. Abdu, H. Takahashi, I. Paulino, U. A. Gasparelo, D. C. Arruda, M. Mascarenhas, C. Zamlutti, C. M. Denardini, D. Koga, A. de Medeiros, and R. A. Buriti (2011), Midnight reversal of ionospheric plasma bubble eastward velocity to westward velocity during geomagnetically quiettime: Climatology and its model validation, *Journal of Atmospheric and Solar-Terrestrial Physics*, *73*(11-12), 1520–1528, doi:10.1016/j.jastp.2010.11.031.
- Spencer, N. W., G. R. Carignan, H. G. Mayr, H. B. Niemann, R. F. Theis, and L. E. Wharton (1979), The midnight temperature maximum in the Earth's equatorial thermosphere, *Geophysical Research Letters*, *6*(6), 444–446, doi:10.1029/GL006i006p00444.
- Spencer, N. W., L. E. Wharton, G. R. Carignan, and J. C. Maurer (1982), Thermosphere zonal winds - Vertical motions and temperature as measured from Dynamics Explorer, *Geophysical Research Letters*, *9*(9), 953–956, doi:10.1029/GL009i009p00953.
- Takahashi, H., M. J. Taylor, J. H. Sobral, A. F. Medeiros, D. Gobbi, and D. Santana (2001), Fine structure of the ionospheric plasma bubbles observed by the OI 6300 and 5577 airglow images, *Advances in Space Research*, *27*(6-7), 1189–1194, doi:10.1016/S0273-1177(01)00159-4.
- Taylor, M. J., J. V. Eccles, J. LaBelle, and J. H. Sobral (1997), High resolution OI (630 nm) image measurements of F-region depletion drifts during the Guara Campaign, *Geophysical Research Letters*, *24*(13), 1699–1702, doi:10.1029/97GL01207.
- Tsunoda, R. T. (1983), On the generation and growth of equatorial backscatter plumes: 2. Structuring of the west walls of upwellings, *Journal of Geophysical Research*, *88*(A6), 4869, doi:10.1029/JA088iA06p04869.

- Tsunoda, R. T. (1985), Control of the seasonal and longitudinal occurrence of equatorial scintillations by the longitudinal gradient in integrated Eregion Pedersen conductivity, *Journal of Geophysical Research*, *90*(A1), 447–456, doi:10.1029/JA090iA01p00447.
- Valladares, C. E., J. W. Meriwether, R. Sheehan, and M. Biondi (2002), Correlative study of neutral winds and scintillation drifts measured near the magnetic equator, *Journal of Geophysical Research*, *107*(A7), 1112, doi:10.1029/2001JA000042.
- Vaughan, J. M. (1989), *The Fabry-Perot Interferometer*, IOP Publishing, Philadelphia, PA.
- Wu, Q., W. Yuan, J. Xu, C. Huang, X. Zhang, J. Wang, and T. Li (2014), First U.S.-China joint ground-based Fabry-Perot interferometer observations of longitudinal variations in the thermospheric winds, *Journal of Geophysical Research: Space Physics*, *119*, 5755–5763, doi:10.1002/2014JA020089.
- Xu, J., A. K. Smith, H.-L. Liu, W. Yuan, Q. Wu, G. Jiang, M. G. Mlynczak, J. M. Russell, and S. J. Franke (2009), Seasonal and quasi-biennial variations in the migrating diurnal tide observed by Thermosphere, Ionosphere, Mesosphere, Energetics and Dynamics (TIMED), *Journal of Geophysical Research*, *114*(D13), D13,107, doi:10.1029/2008JD011298.
- Yao, D., and J. J. Makela (2007), Analysis of equatorial plasma bubble zonal drift velocities in the Pacific sector by imaging techniques, *Annales Geophysicae*, *25*(3), 701–709, doi:10.5194/angeo-25-701-2007.
- Yu, T., C. Huang, G. Zhao, T. Mao, Y. Wang, Z. Zeng, J. Wang, and C. Xia (2014), A preliminary study of thermosphere and mesosphere wind observed by Fabry-Perot over Kelan, China, *Journal of Geophysical Research: Space Physics*, *119*, 4981–4997, doi:10.1002/2013JA019492.
- Yuan, W., X. Liu, J. Xu, Q. Zhou, G. Jiang, and R. Ma (2013), FPI observations of nighttime mesospheric and thermospheric winds in China and their comparisons with HWM07, *Annales Geophysicae*, *31*(8), 1365–1378, doi:10.5194/angeo-31-1365-2013.